IMPACTS OF STREAM BED ADJUSTMENTS ON LOCAL BRIDGE MORPHOLOGY AT HIGHWAY 281

FINAL REPORT

David Admiraal, Molly Likins, Richard Wood, Tirthankar Roy, Sudan Pokheral, Mitra Nasimi, and Gul Laiwal

Department of Civil and Environmental Engineering

University of Nebraska – Lincoln
Lincoln, NE 68588-0531

Sponsored By

Nebraska Department of Transportation and U.S. Department of Transportation Federal Highway Administration

2/17/2026

NEBRASKA
Good Life. Great Journey.
DEPARTMENT OF TRANSPORTATION

University of Nebraska Lincoln

TECHNICAL REPORT DOCUMENTATION PAGE

1. Report No. FY23(021)	**2. Government Accession No.**	**3. Recipient's Catalog No.**
4. Title and Subtitle Impacts of Stream Bed Adjustments on Local Bridge Morphology at Highway 281		**5. Report Date** 2/17/2026 **6. Performing Organization Code**
7. Author(s) David Admiraal Tirthankar Roy Gul Laiwal Molly Likins Sudan Pokheral Richard Wood Mitra Nasimi		**8. Performing Organization Report No.**
9. Performing Organization Name and Address Department of Civil and Environmental Engineering University of Nebraska—Lincoln Lincoln, NE 68588-0531		**10. Work Unit No.** **11. Contract** FY23(021)
12. Sponsoring Agency Name and Address Nebraska Department of Transportation Research Section 1400 Hwy 2 Lincoln, NE 68502		**13. Type of Report and Period Covered** Final Report July 2021 – August 2025 **14. Sponsoring Agency Code**
15. Supplementary Notes		
16. Abstract Abstract		
17. Key Words Sediment Transport, Dam Failure, Morphological Adjustments	**18. Distribution Statement** No restrictions. This document is available through the National Technical Information Service. 5285 Port Royal Road Springfield, VA 22161	

19. Security Classification (of this report) Unclassified	**20. Security Classification (of this page)** Unclassified	**21. No. of Pages** 111	**22. Price**

Form DOT F 1700.7 (8-72) Reproduction of completed page authorized

DISCLAIMER

The contents of this report reflect the views of the authors, who are responsible for the facts and the accuracy of the information presented herein. The contents do not necessarily reflect the official views or policies neither of the Nebraska Department of Transportations nor the University of Nebraska-Lincoln. This report does not constitute a standard, specification, or regulation. Trade or manufacturers' names, which may appear in this report, are cited only because they are considered essential to the objectives of the report.

The United States (U.S.) government and the State of Nebraska do not endorse products or manufacturers. This material is based upon work supported by the Federal Highway Administration under SPR-FY23(021). Any opinions, findings and conclusions or recommendations expressed in this publication are those of the author(s) and do not necessarily reflect the views of the Federal Highway Administration.

ABSTRACT

Nebraska sand-bed rivers have long been used in the development of well-known empirical bedload equations. Some of these studies have shown how adjustments in available sediment led to changes in local stream morphology. The sand-bed rivers of Nebraska are highly susceptible to such changes due to their wide, shallow cross-sections and erodibility. The objective of our study was to develop a methodology to predict both short and long-term channel adjustments for an aggraded sand-bed river – in particular, the Niobrara River.

The field component of our study targeted the reaches of the Niobrara River in northern Nebraska near two bridges, the Highway 11 bridge and the Highway 281 bridge. These reaches are of particular interest because they are situated upstream and downstream of Spencer Dam, which failed in 2019, releasing large quantities of sand into the downstream reach. We began with collecting Uncrewed Aerial System (UAS) data that provides us with point clouds and aerial photos of the sites and hand-collected PPK GPS data for streambed topography and for observing temporal changes at the sites. The point clouds were aligned with USGS data and then used to create Digital Elevation Models (DEMs). The point clouds were also used to calculate local sediment erosion. QGIS was used to create polygons to represent areas of available sediment and areas of erosion in the reservoir. Scripts were written to calculate available volumes and volume losses at the local areas of erosion. There are two areas of eroding deposits upstream of the old dam structure and one area downstream. One of the areas upstream of the dam is losing approximately 250,000 m^3 of sediment each year. The second area upstream of the dam is losing about 90,000 m^3 per year. Erosion losses between 2020 and 2024 for these two areas totaled about 1,400,000 m^3 of sediment. The area downstream of the dam lost a total of 133,000 m^3 between 2020 and 2024. Although this is less than the other two sites, erosion of the downstream area also impacts where the river will ultimately migrate in the long-term.

All three eroding areas contribute to sediment loads that are causing the river to aggrade in the vicinity of the dam. Scripts were written to assess changes in the bed profile over the duration of the project. The results showed that from spring of 2024 to September of 2022, the bed and local water surface elevation at the bridge increased by approximately 0.45 meters. Data collected in August of 2023 showed that the bed still had the same slope as the 2020 DEM bed, but that the bed and water surface elevation continued to increase another 0.06 meters at the bridge.

HEC-RAS was used to create a one-dimensional model of the Niobrara River at the Highway 281 bridge. Data collected in 2023 were incorporated in the model to assess model performance and to adjust the model to recreate the observed data. Standing waves were observed in aerial imagery and confirmed the results of the model that showed that the flow of the river is critical through the entire reach. The bathymetry changes in the river are complicated due to the self-formed river bed with multi-channel flow and critical flow conditions. Overcoming these complexities was not possible in the current project and will be necessary to develop a two-dimensional model that is able to accurately predict short- and long-term morphological changes at the study site. These obstacles are discussed more thoroughly in the conclusions.

Table of Contents

1. Introduction 1
1.1. Background 1
1.2. Report Layout 1
2. Literature Review 3
2.1. Introduction 3
2.2. Stable Channel Geometry 3
2.2.1. Width relations 3
2.2.2. Erosion and sediment transport 10
2.3. Ice Erosion 18
3. Study Site 23
3.1. Introduction 23
3.2. Site Description 23
3.2.1. Highway 11 to Highway 281 23
3.2.2. Niobrara River at Highway 281 24
3.3. Hydrology 24
4. Data Sources and Processing 28
4.1. Introduction 28
4.2. Source Data and Data Preparation 28
4.2.1. Data summary 28
4.2.2. Aerial imagery 28
4.2.3. External DEMs and point clouds 29
4.2.4. Orthomosaics 29
4.2.5. Project-based point clouds 29
4.2.5.1. Project-based point cloud processing 30
4.2.5.2. Project-based point cloud alignment 30
4.2.5.3. Realignment of project-based point clouds 31
4.2.5.4. Creation of DEMs from project-based point clouds 31
4.2.5.5. Identification of local river channel plane 32
4.2.6. Hand collected GPS data 33
4.2.6.1. Data collection 33
4.2.6.2. Alignment of PPK GPS data 34
4.3. Site Visit Overview 34
4.3.1. September 2022 site visit 34
4.3.2. March 2023 site visit 35
4.3.3. August 2023 site visit 37
4.3.4. February 2024 site visit 39
5. Sediment Budget Calculations and Measurements 41
5.1. Introduction 41
5.2. Longitudinal Elevation Profile of Niobrara River 41
5.3. Sediment Volume Calculation Methods 46

5.4. Sediment Erosion and Availability Volume Results 51
5.4.1. Sediment erosion downstream of the dam 51
5.4.2. Sediment availability and erosion upstream of the dam 55
5.4.3. Summary of sediment availability and erosion at the study site 57
5.4.4. Sediment volumes released immediately after the dam failure 57
6. Hydraulic Modeling 60
6.1. Modeling Approach 60
6.1.1. Preliminary one-dimensional model 60
6.1.2. One-dimensional model 61
6.1.3. Quasi-unsteady sediment transport model 62
6.2. Estimating Points for Incomplete Cross-sections 63
6.3. Model Runs 68
6.3.1. Simple Model Run 68
7. Conclusions 78
7.1. Conclusions 78
7.2. Recommendations for Further Work 79
References 81
Appendix A. Field Site Information 84
A.1. September 2022 Site Visit Information 85
A.2. March 2023 Site Visit Information 88
A.3. August 2023 Site Visit Information 91
A.4. Sediment Graphs – Data from Schaepe et al. (2018) 94
Appendix B. Two-Dimensional Computer Models 98
Appendix C. National Agricultural Inventory Program Results 100

List of Figures

Figure 3.1 Overview of Highway 11 to Highway 281(NAIP, 2022)..... 24
Figure 3.2 NAIP (2024) aerial of the 7 km reach upstream of Highway 281..... 24
Figure 3.3 Watershed map for the Spencer/Highway 281 site. 25
Figure 3.4 Log-Pearson Type 3 plot of Niobrara River annual peak flows at Verdel, NE..... 26
Figure 3.5 Log-Pearson Type 3 plot of Niobrara River annual peak flows at Highway 11, NE.. 27
Figure 4.1 Example of the elevation profile tool in QGIS showing 2013 (green) and 2020 (lavender) cross sections of the Niobrara immediately downstream of Highway 281. 31
Figure 4.2 September 2022 orthomosaic at Highway 11..... 35
Figure 4.3 September 2022 orthomosaic at Highway 281..... 35
Figure 4.4 March 2023 orthomosaic at Highway 11 36
Figure 4.5 March 2023 orthomosaic at Highway 281 37
Figure 4.6 August 2023 orthomosaic at Highway 11 38
Figure 4.7 August 2023 orthomosaic at Highway 281 39
Figure 4.8 February 2024 orthomosaic at Highway 11 40
Figure 4.9 February 2024 orthomosaic at Highway 281 40
Figure 5.1 closeup of cross sections 42
Figure 5.2 Cross sections spaced at 50-m intervals for the entire reach from Highway 11 to 503rd Avenue..... 42
Figure 5.3 Comparison of minimum elevations as a function of distance downstream of the Highway 281 Bridge..... 43
Figure 5.4 Longitudinal profiles of water surface at Highway 281..... 45
Figure 5.5 Longitudinal profile of water surface at Highway 281 (enlarged)..... 45
Figure 5.6 Plan view of the study site showing Areas A through C..... 46
Figure 5.7 Flowchart of methods for finding available and eroded area volumes: Method 1 is for point cloud data and Method 2 is for uniformly spaced DEM rasters. Green cells were done in CloudCompare and Blue cells were done in QGIS..... 47
Figure 5.8 Sediment deposits upstream and downstream of the dam based on the 2020 DEM... 50
Figure 5.9 Cross section polygons covering the study reach..... 50
Figure 5.10 Sediment availability in the vicinity of Spencer Dam as determined from the 2020 DEM using a moving datum based on minimum channel centerline elevations..... 51
Figure 5.11 Progression of receding bankline at Area C from (a) 2020, (b) 2020 to Sept. 2022, (c) 2020 to March 2023, (d) 2020 to Aug. 2023, and (e) 2020 to Feb. 2024..... 52
Figure 5.12 Area lost between September 2022 and February 2024..... 53
Figure 5.13 Point cloud elevation grid (irregularly spaced) (Sept 2022 – February 2024)..... 53
Figure 5.14 Resulting raster with lost elevation in each cell (Sept 2022 – February 2024)..... 54
Figure 5.15 Biannual sediment loss polygons based on NAIP observations. Green – 2020 DEM to 2020 NAIP. Yellow – 2020 NAIP to 2022 NAIP. Red – 2022 NAIP to 2024 NAIP 56
Figure 5.16 Sediment losses upstream of Spencer Dam between 2013 and 2020 DEMs for a 6 km reach upstream of Spencer Dam 58
Figure 5.17 Sediment losses upstream of Spencer Dam between 2013 and 2020 DEMs for a 10 km reach upstream of Spencer Dam 58

Figure 6.1 Overview of August 2023 measured cross-sections 64
Figure 6.2 Cross-section 1 65
Figure 6.3 Cross-section 2 65
Figure 6.4 Cross-section 3 66
Figure 6.5 Cross-section 4 67
Figure 6.6 Cross-section 5 67
Figure 6.7 Cross-section 6 68
Figure 6.8 HEC-RAS longitudinal profile result 69
Figure 6.9 Cross-section 1 model result 72
Figure 6.10 Cross-section 2 model result 73
Figure 6.11 Cross-section 3 model result 74
Figure 6.12 Cross-section 5 model result 75
Figure 6.13 Cross-section 6 model result 76
Figure A.1 Sediment Graph for Niobrara River near Spencer, Nebraska 94
Figure A.2 Sediment Graph for Niobrara River near Redbird Creek 95
Figure A.3 Sediment Graph for Niobrara River near Verdel, Nebraska 96
Figure A.4 Sediment Graph for Niobrara River upstream of Spencer Dam 97
Figure C.1 NAIP aerial imagery of the Niobrara for Boyd and Holt Counties from (a) 2018 and (b) 2020 102
Figure C.1(cont.) NAIP aerial imagery of the Niobrara for Boyd and Holt Counties from (c) 2022 and (d) 2024 103
Figure C.2 7km long NAIP aerial images upstream of HW281 in (a) 2018 and (b) 2020 104
Figure C.2 (cont.) 7km long NAIP aerial images upstream of HW281 in (c) 2022 and (d) 2024 105
Figure C.3 Available sediment deposits upstream and downstream of the dam based on the 2020 DEM. Yellow is Area A and represents the largest deposit. Orange is Area B. Red is Area C. Area C is an underestimate and represents areas eroded thus far, but it is a small amount of sediment compared to what remains upstream of the dam in Areas A and B 106
Figure C.4 Sediment availability in the vicinity of Spencer Dam as determined from the 2020 DEM using a datum based on minimum channel centerline elevations 107
Figure C.5 Biannual sediment loss polygons based on NAIP observations. Green – 2020 DEM to 2020 NAIP. Yellow – 2020 NAIP to 2022 NAIP. Red – 2022 NAIP to 2024 NAIP. Note that green represents a much shorter time period than yellow and red. 108
Figure C.6 Sediment losses upstream of Spencer Dam between 2013 and 2020 DEMs utilizing information as far as 6 km upstream of Spencer Dam 110
Figure C.7 Sediment losses upstream of Spencer Dam between 2013 and 2020 DEMs utilizing information as far as 10 km upstream of Spencer Dam 111

List of Tables

Table 4.1 Data retrieved from external sources and field measurements (green rows)..... 28
Table 4.2 Summary of September 2022 data collection..... 34
Table 4.3 Summary of March 2023 data collection..... 36
Table 4.4 Summary of August 2023 data collection..... 37
Table 4.5 Summary of February 2024 data collection..... 39
Table 5.1 Eroded volumes for Area C..... 54
Table 5.2 Estimates of sediment eroded from Area C since 2020 – calculated using 2020 DEM..... 54
Table 5.3 Comparison of Area C calculations..... 55
Table 5.4 Available sediment deposits estimated from the 2020 DEM in Areas A and B..... 55
Table 5.5 Estimates of sediment deposits eroded since 2020 – calculated using the 2020 DEM..... 56
Table 5.6 Estimates of cumulative eroded sediment since 2020 – calculated using the 2020 DEM..... 57
Table A.1 Visit 1 Discharges (cfs) at Butte gauge and temperatures (°F) at Verdel..... 85
Table A.2 Weather at Lynch, Nebraska, September 10, 2022..... 87
Table A.3 Weather at O'Neill, Nebraska, September 10, 2022..... 87
Table A.4 Visit 2 Discharges (cfs) at Butte gauge and temperatures (°F) at Verdel..... 88
Table A.5 Weather at Lynch, Nebraska, March 20, 2023..... 90
Table A.6 Weather at O'Neill, Nebraska, March 20, 2023..... 90
Table A.7 Visit 3 Discharges (cfs) at Butte gauge and temperatures (°F) at Verdel..... 91
Table A.8 Weather at Lynch, Nebraska, August 30, 2023..... 93
Table A.9 Weather at O'Neill, Nebraska, August 30, 2023..... 93
Table C.1 NAIP Aerial imagery information for Boyd County..... 101
Table C.2 NAIP Sediment deposits and erosion from the time of the DEM until the specified NAIP Raster..... 109
Table C.3 Analyzed areas and volumes eroded between 2013 and 2020 DEM for six and ten kilometers upstream of dam..... 111

1. Introduction

1.1.Background

The bomb cyclone that took place in March of 2019 caused great devastation in the Midwest. The storm itself produced a large quantity of precipitation, but this was aggravated by the frozen ground which was mostly impervious and a large amount of existing snow that melted during the event. Moreover, due to a prior cold snap, streams and rivers had thick layers of ice. Following the event, Nebraska rivers had major ice jams and flooding. Bridges, and hydraulic structures were severely damaged as a result. In northern Nebraska, Niobrara River ice jam flooding caused the destruction of Spencer Dam and the approach to the Highway 281 bridge over the Niobrara River. Since then, the Niobrara River has taken a new course and is constantly changing.

The Niobrara River has fine sediments (sand and silt) and is very wide and shallow. High velocities near the Highway 281 bridge cause standing waves. These standing waves indicate critical flow. Sediment transport capacity is high due to the high flow velocities. Since the failure of Spencer Dam, stream bed elevations have adjusted and have led to significant changes in local stream morphology.

Understanding these streambed morphological changes is crucial to better predict short-term and long-term channel migration for aggraded sand-bed rivers. A hydrodynamic model can be created by collecting detailed flow and topographic data and implementing them into the model. A model that can predict short-term and long-term morphological changes can be beneficial for structures to be designed to last for decades.

The first objective of this project was to establish a measurement method for rapidly collecting detailed topographic, bathymetric, and flow data at bridge crossings. The second objective was to utilize the new method to collect multiple complete data sets at a bridge crossing with dynamic streambed conditions (The Highway 281 bridges downstream of the Spencer Dam site). The third objective was to develop a baseline hydraulic modeling approach to recreate observed data at the bridge crossing. The fourth and final objective was to refine the modeling and data collection methods for the application of a more complex hydrodynamic model at the local bridge crossing at Niobrara River.

1.2. Report Layout

The fulfillment of these four research objectives focused on the morphological changes at Highway 281 near Spencer Dam and the reach between the bridges at Highway 11 and Redbird Creek, upstream and downstream of Spencer Dam, respectively. Achieving these research objectives required multiple components that are presented and discussed in subsequent chapters and appendices, including collected background information, doing a thorough assessment of sediment and morphological changes occurring at the study site, and generating and analyzing a hydrodynamic model for the Niobrara River at Highway 281.

The literature review chapter provides information about stable channel geometry and ice erosion. Stable channel geometry focuses on width and velocity relations, and erosion and

sediment transport in shallow, wide, and sand-bedded rivers. This section explores possible ideas for the generation and analysis of an accurate hydrodynamic model for sand-bedded rivers.

The third chapter provides a description of the study site, including a first look at the geomorphology that defines river characteristics. The watershed of the site is then presented. Finally, the chapter provides a look at the hydrology of the Niobrara River at Highway 281, and particularly the ice flow dynamics that define a major part of the channel forming characteristics of the river.

Chapter four presents the data that were collected over the course of the study, including imagery, elevation data, and GPS measurements. A large quantity of data were collected in four visits to the study site, during which an Uncrewed Aerial System (UAS) was used to collect extensive orthomosaics and point clouds of the study site. During visits when the river bed was accessible, GPS data were also collected to establish flow cross-sections and baseline elevation information. Additional data were collected from external sources, such as USGS, NDNR (The Nebraska Department of Natural Resources), and USDA (National Agricultural Inventory Program). In addition to describing the data that were collected, some of the data processing techniques are also described in detail.

In chapter five, sediment budget calculations and measurements are described. This chapter provides significant insight into expected future grade changes of the river and information about the likely rate at which the sediment reservoir behind the failed dam will continue to erode. It also provides a quantitative assessment of the amount of sediment that is still in storage and is likely to be released by future high flows.

Chapter six explains the development of a one-dimensional model of the study site. This includes a description of the establishment of flow cross-sections for the one-dimensional model followed by a description of the model and its results.

Finally, the conclusions chapter summarizes the findings of the study and provides recommendations for improvements necessary to produce a higher quality two-dimensional model of the study site which can better predict sediment transport changes.

2. Literature Review

2.1.Introduction

Understanding how channel geometry is formed and influenced by factors such as velocity, width relations, erosion, and sediment transport is crucial for producing high-quality models. Velocity plays a key role in determining both the stability and width of the channel, while instability often leads to increased erosion. Sediment transport, in turn, influences the channel's shape, the position of the thalweg, and the river's longitudinal profile. Braided rivers introduce added complexity due to their multiple shifting channels and high sediment load. Additionally, recognizing the differences in behavior between straight and meandering channels is essential, as meandering channels typically experience more complex patterns of erosion and deposition than straight channels. By fully grasping the impact of these hydraulic elements on channel geometry, a more accurate and reliable model for predicting channel behavior can be developed.

2.2.Stable Channel Geometry

2.2.1.Width relations

In *Stable Channel Cross Sections of Straight Sand Rivers* by Ikeda and Izumi (1991), a mathematical model is presented for specifying the size and cross-section of straight sand-bedded rivers in which there is sediment fine enough to be transported as bedload and suspended load. The assumptions the authors make in creating this mathematical model are that the channel is straight and wide, has a constant downstream slope, center depth, width, uniform noncohesive fine sediment size, and is split into a central section and bank sections. Since the channel is wide, depth-averaged shallow water flow can be assumed in treating the flow field (Ikeda and Izumi, 1991). As a river meanders, the velocity varies across the width of the river. This variation in flow speed leads to erosion on concave banks and deposition on convex banks, resulting in more meandering of the river. Bank vegetation stimulates deposition in the bank regions (Ikeda and Izumi, 1991). Ikeda and Izumi solve differential equations derived from the continuity and momentum equations for sediment transport and fluid flow. Results are that the stable channel depth shows that the relative depth is proportional to $S^{-0.8}$ for natural sand-bedded channels, and the stable channel width can be found using a function of flow discharge, longitudinal slope, and sediment size (Ikeda and Izumi, 1991). The key to keeping channel cross-section stability is maintaining a balance in erosion and deposition.

Ikeda and Izumi (1991) present a model for stable, straight, sand-bedded rivers, showing how erosion-deposition balance, sediment size, and flow dynamics maintain channel cross-section stability. Popovic et al. (2021) expand on this by demonstrating that lateral momentum diffusion and sediment discharge shape laminar rivers, with excessive sediment flux leading to instability and braided channels. The goal of Popovic et al. (2021) was to show that equilibrium between fluid stresses and gravity acting on the sediment grains, along with cross-stream diffusion of sediment, dictates the shape and the sediment flux profile of laminar laboratory rivers that carry sediment as bedload. Popovic et al. created a theory that the shape of the river is represented as a function of water and sediment discharges. They find that when the sediment load is large, the diffusion of momentum laterally creates an excess of stress on the riverbed, and this drives sediment transport. Momentum diffusion, thus, plays a key role in determining the shape of the

channel. Popovic et al. demonstrated that as sediment discharge increases, the flux of sediment approaches its maximum and this causes the river to get wider and shallower. But as the sediment discharge increases past the experiment threshold it destabilizes the river and forms a braided river.

Popovic et al. (2021) illustrate how sediment discharge and momentum diffusion shape laminar river channels, with excessive sediment flux leading to destabilization and braided rivers. Similarly, Wilson (1973) emphasizes the challenges of maintaining equilibrium in natural rivers, linking channel shape and flow dynamics to sediment size, with larger grains favoring braided formations and smaller grains supporting meandering channels. Wilson (1973) discusses how maintaining a constant equilibrium cross-section profile is nearly impossible due to rapid flow fluctuations. In natural rivers, when sediment is transported as bed load it must continue to move downslope towards the thalweg because of gravity. But if the channel maintains shape, there must be an equal force upslope acting on the sediment to keep the shape of the channel. Wilson found that with increasing grain size the channel becomes shallower and wider until it reaches a stage in which the secondary flow divides to form two vortex pairs with many sub-channels. Wilson also concludes that braided rivers will form with riverbeds that have larger sediment sizes and meandering rivers with riverbeds that have smaller-sized sediments.

Wilson (1973) highlights how sediment size and flow dynamics shape river channels, with larger grains promoting braided rivers and smaller grains favoring meandering patterns, while emphasizing the difficulty of maintaining equilibrium due to flow fluctuations. Building on this, Dunne and Jerolmack (2020) use threshold-limited channel models and hydraulic data to predict how sediment load and entrainment thresholds influence channel width and morphology, supporting the idea that higher discharge and sediment transport drive channel widening and pattern changes. Dunne and Jerolmack (2020) test a threshold-limited channel model with a combination of analysis of a global dataset of hydraulic geometry measurements. Dunne and Jerolmack use this model to predict how changes in the entrainment threshold could cause the river channel pattern to change from braided to single-threaded. This is done by applying a first-order influence on the channel aspect ratio. Parker's theory suggests that increased sediment load can lead to channel widening. Parker's theory is a mathematical and physical model that pursues an explanation of the behavior and formation of channel patterns, specifically how the channel morphology is influenced by the balance of discharge and sediment transport. Dunne and Jerolmack's study show a strong correlation between sediment load and channel width. Parker's theory also suggests that bedforms and sediment distribution affect channel width and stability. This study proves that higher discharge tends to increase the width of the river, supporting the idea that more flow can cause the channel to widen which increases sediment transport. The results indicate that sediment transport and flow conditions can influence the channel width and stability.

Dunne and Jerolmack (2020) explore how sediment transport and flow conditions influence channel width and stability, demonstrating that variations in entrainment thresholds can shift river patterns from braided to single-threaded. Complementing this, Dey (2001) provides a computational framework for predicting the bank profiles of threshold channels with

noncohesive sediments, using fluid dynamics and sediment characteristics to model channel morphology with results consistent with prior experimental studies. Dey (2001) provides a simplified approach for the computation of a bank profile of a self-formed threshold channel with noncohesive sediment that is uniform. Dey computed the bank profile by first computing $\widehat{D} = k_s \left(\frac{\Delta g}{\nu^2}\right)^{1/3}$; where k_s is the equivalent roughness height (=$2d_{50}$), $\Delta = s - 1$ and s is the relative density of sediment, g is the gravitational constant, and ν is the kinematic viscosity of water. Second, Dey found $\hat{\tau}$ using $\widehat{D}$ and the following equations:

$$\hat{\tau} = 0.142\widehat{D}^{-0.35} \text{ for } \widehat{D} \leq 1, \tag{2.1}$$

$$\hat{\tau} = 0.148\widehat{D}^{-0.60} \text{ for } 1 < \widehat{D} \leq 15 \tag{2.2}$$

$$\hat{\tau} = 0.013\widehat{D}^{0.32} \text{ for } 15 < \widehat{D} \leq 50 \tag{2.3}$$

$$\hat{\tau} = 0.045 \text{ for } \widehat{D} > 50 \tag{2.4}$$

Then Dey used $\hat{\tau}$ to find $[\tau]_{\theta=0} = \hat{\tau}(\rho g \Delta d_{50})$. $[\tau]_{\theta=0}$ was then used to calculate $h = [\tau]_{\theta=0}/\rho g S$, where S is the longitudinal slope of the free surface. Then the variation of $\hat{y}$ with $\hat{x}$ was found using a fourth order Runge-Kutta method to solve:

$$\sqrt{\eta^2\mu^2 - 1}\frac{d\hat{y}}{d\hat{x}} = \mu\sqrt{[(1 - \hat{y} + Cm\hat{x}^{m-1})(1 - \eta\mu) + \eta\mu]^2 - 1}, \tag{2.5}$$

Where $C = 0.0027$ and $m = 4.5$, and these values were obtained from experimental data from a different experiment. The flow cross section Area A and the top width T were the found using $y = \hat{y}h$ and $x = \hat{x}h$. And finally, the discharge Q was computed using:

$$Q = AV = 2.5A\sqrt{g\left(\frac{A}{P}\right)S}\ \ln\left(11\ \frac{A/P}{d_{50}}\right). \tag{2.6}$$

These steps were implemented in a computer program. The computer program required d_{50}, S, and μ as input data. And μ was found using:

$$\mu = \tan[0.302(logd_{50})^5 + 0.126(logd_{50})^4 - 1.811(logd_{50})^3 - 0.57(logd_{50})^2 + 5.95(logd_{50}) + 37.52] \tag{2.7}$$

The predictions from this model agree with other models from Diplas and Viligar (1992) and Yu and Knight (1998). But the model slightly underestimates the experimental data (Dey, 2001).

Dey (2001) presents a computational approach for predicting the bank profiles of threshold channels with noncohesive sediments, using hydrodynamic equations and sediment properties to calculate parameters like discharge and cross-section geometry. Building on predictive modeling, Francalanci et al. (2020) employ the Cross-Section Evolution Model (CSEM) to determine equilibrium channel widths in gravel and sand-bedded rivers, incorporating factors such as bank

roughness, shear stress, and sediment transport, with robust validation across diverse datasets. In Francalanci et al. (2020), the goal was to determine the equilibrium bankfull channel width in gravel and sand bedded rivers using channel slope, median grain size, discharge flowing into the channel, and critical shear stress of the banks. Francalanci et al. first formulate the model to be applied to larger datasets, and then validate the model with gravel and sand-bedded rivers for predicting the equilibrium width and depth of river cross section. The assumptions Francalanci et al. make to formulate the model are that the cross-sectional shape of the channel is rectangular, the bankfull flow is uniform, and the banks are cohesive. The model is formulated by finding the bankfull cross-sectional average velocity (U_{bf}) first by using the following equations:

$$\frac{U_{bf}}{u_{*bf}} = \frac{C_{bf}}{g^{1/2}}, \quad u_{*bf} = \left(gSR_{bf}\right)^{1/2}. \tag{2.8}$$

Where g is the acceleration of gravity, u_{*bf} is the bankfull friction velocity, R_{bf} is the bankfull hydraulic radius, and C_{bf} is the overall Chezy coefficient. The rectangular channel is split into 3 sections (2 bank regions and a central region), where the central region has a width $B_{bf} - 2z_{out}$. The two bank regions are then split into two triangles (upper triangle and lower triangle) that have the areas of $H_{bf}\ z_{out}\ /\ 2$. The flow resistance for the lower triangle is affected by the channel bed roughness. The flow resistance for the upper triangle is affected by the bank roughness. The thickness of z_{out} can be computed with:

$$z_{out} = 2\frac{u_{*T}^2}{gS}. \tag{2.9}$$

And $u_{*T} = (\tau_T/\rho)^{1/2}$, where τ_T is the total shear stress exerted on the banks. Then the bankfull discharge can be found by the following equation:

$$Q = A_{bf}U_{bf} = A_0U_0 + 2(A_{LT}U_{LT} + A_{UT}U_{UT}). \tag{2.10}$$

The subscript 0 denotes the central region of the flow while the subscripts *LT* and *UT* denote the lower and upper triangles, respectively. Using the equations above can be simplified to:

$$A_{bf}C_{bf}\sqrt{SR_{bf}} = A_0C_0\sqrt{SR_0} + 2(A_{LT}C_{LT}\sqrt{SR_{LT}} + A_{UT}C_{UT}\sqrt{SR_{UT}}). \tag{2.11}$$

For the central region of flow, the velocity profile normal to the bed can be calculated using

$$u(y) = \frac{u_{*0}}{\kappa}\ln\left(\frac{y}{y_{0T}}\right), \tag{2.12}$$

Where κ is the von Karman constant, the friction velocity ($u_{*0} = (\tau_0/\rho)^{1/2}$) related to the total shear stress τ_0, and the reference level where velocity vanishes ($y_{0T} = 0.033e_s$), which is related

to the roughness height based on experimental data from van Rijn (Francalanci et al., 2020). And from van Rijn, the effective roughness is set to $3D_{90}$.

The Cross-Section Evolution Model (CSEM) is a modeling framework that is used to predict the equilibrium width of rivers with cohesive banks. The CSEM model consists of three units (Flow unit, Kean and Smith unit, and Erosion unit). Each unit is a submodule that takes inputs and puts them through a series of equations that compute an output that is needed for the next unit. For instance, the bankfull discharge (Q_{bf}),the channel slope (S), median grain size (D_{50}), and a trial value of the bankfull width (B_0) are inputs for the first main unit, the flow unit. Then the flow unit takes these inputs and calculates the flow velocity at a specified outer boundary layer, u_{out}. Then the bank roughness Gaussian shape variables ($z_{0sf}, \sigma_{reg}, \lambda_{reg}$) and the u_{out} are inputs for the next main unit, the Kean and Smith unit or the (Near-bank shear stress). Then the outputs from the Kean and Smith unit are τ_{SF} and H_{bf}, these are inputs for the last main unit called the Erosion unit. If $\tau_{SF} > \tau_c$, the river widens and the iterative procedure starts again with an increased value of width $B > B_0$, But if otherwise the cross-section is assumed to be at equilibrium and the algorithm stops. H_{reg} (Gaussian-shaped bank geometry) and τ_c (critical shear stress for bank sediment erosion) are calibration parameters that are adjusted to obtain the best agreement between computed and observed bankfull width, B_{bf}. Francalanci et al. assume that the bank erodibility is in the range of 0.5-4 Pa if there is little vegetation. But if the banks are highly vegetated the bank erodibility factor can be increased up to 2.5. Wider rivers have bigger roughness elements in general. Bump geometry can vary with flow discharge. The "bumps" that Francalanci et al. refers to are the observation of bumps along the bank from a top view of the channel. Bump geometry refers to the mean height and wavelength of these bumps. Periods when there was intense erosion led to an increase in the riverbank macroroughness. The outcome of this increase enhances the thickness of the bank boundary layer and decreases skin friction. This leads to a smoothing of the bump induced roughness and consistent geometry of the bumps.

The application of the CSEM model to a large data set concerning the features of rivers at bankfull conditions led Francalanci et al. to express the critical shear stress at the bank and the average height of the bumps as a function of the bankfull discharge. The model was robust for large datasets and valid for both gravel and sand bed rivers in predicting flow depth and river width.

Francalanci et al. (2020) and Parker (1978) both explore the dynamics of equilibrium channel morphology, yet their approaches and assumptions differ significantly. While Francalanci et al. provide a robust model applicable to cohesive banks and various sediment types, Parker focuses on sediment transport in sandy, non-cohesive systems, highlighting the interplay between bank sediment and central channel depth. Parker (1978) states "Sand predominates in the bed, banks, and flood plain of considerable reaches of many of the streams arising in the Nebraska Sandhills…". This includes the Niobrara River. Parker hypothesized that equilibrium is achieved by bed load transport and the slope from the bank to the central region of the river moving bank sediments to the central region. Such that when the banks are already shallow and overloaded, the depth of the central region decreases. And when the banks are deep and underloaded, the depth of the central region increases.

The bed boundary condition is that the vertical flux of suspended sediment should be continuous at the bed and for non-cohesive material the bed boundary condition can be expressed as

$$-\epsilon(z)\left[\frac{\partial c}{\partial z}\right]_{z=a} = v_s E. \tag{2.13}$$

Where ϵ is a kinematic eddy diffusivity, z is the height above the bed, c is the volumetric sediment concentration, a=0 if a vertically constant eddy diffusivity is used, v_s is the fall velocity, and E is a dimensionless erosion rate. This is known as the gradient boundary condition and is critical in describing overloading and underloading in banks correctly. And this boundary condition is used to formulate a model. The model results of the relative roughness of the center of the channel are compared with data collected from the Middle Loup River and the Niobrara River. Both rivers have unusually uniform discharges maintained by groundwater accretion (Parker, 1978). Secondary currents in meandering channels, or meandering flows in straight channels, are known to play an important role in determining the cross-sectional shape (Parker 1978). Parker's model does not consider the secondary current, thus causing the calculated profile and the observed profiles of cross-sections of the Middle Loup and Niobrara to be slightly different. Parker suggests that meandering alone does not seem to provide a mechanism for choosing a preferred width for a channel migrating in a non-cohesive flood plain.

Parker's focus on equilibrium through sediment transport and bank interaction highlights how central channel depth adjusts to bank conditions. In contrast, Leopold (1953) extends the discussion by examining how changes in discharge, sediment load, and channel geometry interact to influence river morphology and downstream adjustments. Leopold (1953) discusses observed natural channel characteristics, such as width, depth, velocity changes, downstream slope, and downstream roughness, in relation to observed data on suspended-sediment load. Leopold also discusses the adjustment process between the channel cross-section shape and the sediment load through the consideration of river hydraulics.

The different discharges at a given cross-section vary in frequency (Leopold, 1953). In a low discharge channel, assuming the frequency of the rate of discharge is constant across the cross-section, the channel cross-section shape remains the same, but the channel cross-sectional area gets bigger. With the same assumption, for a high discharge channel, the river cross-section stretches wider, and the depth remains shallow. The changes in discharge are from changes in velocity, width, and depth. The relative rates of increase of width, depth, and velocity are determined by the shape of the channel, the slope of the water surface, and by the roughness of the wetted perimeter. As the river continues downstream, the discharge will increase due to the increasing drainage area. Leopold studied multiple rivers and found that all but one have similar slopes when comparing the width, depth, and velocity in relation to the mean annual discharge. The anomaly river is the Loup River. Leopold believes that the ground-water contributions from the sandhills are partly responsible for the anomalous behavior. The fact that velocity increases downstream with mean annual discharge in the rivers studied indicates that the increase in depth overcompensates for the decreasing river slope (Leopold, 1953). When it comes to the geometry of the channel in relation to sediment load, the concentration of suspended sediment increases

with discharge. It might be presumed that because the bed of an alluvial river tends to be scoured during high discharges, the observed increase of suspended-sediment concentration with increased discharge results from the suspension of the additional material scoured out of the bed by concomitant high velocity (Leopold, 1953). The relationship between suspended sediment and discharge in the downstream direction is that the concentration of suspended sediment decreases as the drainage area increases. As stated earlier, the discharge increases as the drainage area increases. The relationship between channel width, depth, velocity, and suspended sediment at a constant discharge was observed with multiple cross-sections at multiple rivers. It concludes that at a constant width and decreasing depth, the velocity and suspended sediment concentration increase. At a constant velocity and decreasing depth, the width increases and the concentration of suspended sediment decreases. At near-peak discharges, the concentration of suspended sediment increased at a slower rate than at a slightly lower discharge. This slower rate of increase is associated with bed scour. The foregoing analyses of scour and fill of a riverbed during flood demonstrate that the changes in the bed occurred simultaneously with changes in the rate of change of suspended-sediment concentration (Leopold, 1953). An increase in the channel roughness is an effect of the decrease in the concentration of suspended sediment, and the slope remains constant. The particle size, bed configuration, and sediment load are the factors that affect the bed roughness. In sand-bedded rivers, there are ripples and dunes that are constantly changing depending on the location of the cross-section and the particle size does not contribute as much to the bed roughness as the bedforms. Thus, the roughness is constantly changing with the bed configurations along the river length. The slope can be adjusted over time by the changes in the stream. Leopold summarized that load and discharge are independent factors, slope is a dependent factor, and width, depth, velocity, bed roughness, and particle sizes are semi-dependent.

Leopold's observations on channel characteristics and their adjustments to sediment load provide a foundation for understanding how rivers respond to varying discharges. Building on this, Alexander et al. (2009) focus specifically on the Niobrara River, examining its unique hydrological attributes and the challenges of accurately measuring its hydraulic geometry. Alexander et al. (2009) provide hydrological and physical attributes of the Niobrara River, such as the drainage area of 13,480 square miles, average annual precipitation of 24 inches, and the bedrock being gently sloping and flat. The Niobrara River holds unique qualities in terms of channel types. The Niobrara River has a custom classification scheme developed to study segments of the river longitudinally. When it comes to hydraulic geometry, there are limitations. One limitation is the discharge measurements are not always measured at the same location. A second limitation is when the measurement is collected from a gage house, the discharge measurements are not representative of the channel upstream and downstream. A third limitation of hydraulic geometry is the measurements themselves, which may be limited in the range of flows, have varying degrees of uncertainty, and may be greatly affected by environmental conditions such as ice or debris (Alexander et al., 2009). Based on the initial results, Alexander et al. show the relations between discharge and channel width, average cross-sectional depth, and average flow velocity. According to Alexander et al.’s analysis, the discharge range is between 540-12,500 cfs. Based on the discharge range the average flow velocity range in feet per second is approximately between 2.1 and 8.0. The range for average cross-sectional depth in feet is

approximately between 1.4 and 3.9. The channel top width range in feet is approximately between 195 and 340.

2.2.2.Erosion and sediment transport

In de Almeida and Rodríguez (2011), pool-riffle dynamics are analyzed using an unsteady one-dimensional flow morphology and bed-sorting model. The 1-D model approach is used to provide insight into the effects of different sediment sizes in shaping and maintaining the pool-riffle longitudinal profile while limiting computational complexity. Sediment transport and flow dynamics play key roles in shaping pool-riffle sequences. Although progress has been made in comprehending the intricate properties of flows in the pool-riffle sequences, there has not been as much progress in sediment transport in pool-riffle sequences. Sediment transport seems to be the missing intermediate step between flow and morphology. de Almeida and Rodríguez mention more specifically that fractional transport, longitudinal grain sorting, bed level fluctuations and their feedback on flow, and the history of past flows are all expected to play a significant role in pool-riffle morphodynamics. The 1-D model does not consider flow concentration, secondary currents, bank failure, vegetation interaction with flow and sediment, or soil porosity changes in the bed sorting process. However, the 1-D model provides simplicity, is effective in capturing longitudinal dynamics, is easier to validate with real observations, and is appropriate for de Almeida and Rodríguez's objectives for this research. The hydraulic model solves the Saint-Venant 1-D unsteady flow equations by a generalized form of the Priessman four-point implicit finite difference scheme. The Priessman scheme is commonly used for time-dependent problems, as it is accurate and stable for problems with time steps. The hydraulic model also includes procedures to enhance the model under near-critical and small-depth conditions. The sediment transport model that is being used is the Wilcock and Crowe transport model. This model is primarily used to estimate bedload transport rates and fractional transport rates for mixed sand-gravel sediment. The use of cross-sectional average shear stress might cause significant underestimations of sediment transport rate to rise because of the nonlinearity of the bed load relations in 1-D models (de Almeida and Rodríguez, 2011). To improve the estimation, the cross-section is divided into vertical strips, and the transport formula is applied to each strip. The morphological model is quite simple. The bed level changes are solved in two steps. The first step is solving the Exner equation or the 1-D sediment continuity equation. This yields the cross-section-averaged values of erosion. The second step is distributing the cross-section-averaged values of erosion over the cross-section. The grain sorting model requires prior knowledge of the bed and bedload grain size distributions. The grain size distribution changes are calculated using mass conservation. de Almeida and Rodríguez's results conclude that longitudinal grain sorting is important in pool-riffle morphodynamics. There are two key mechanisms responsible for the upkeep of pool-riffle sequences. The first is that deposition of downstream riffles enhances flow reversal probability in the upstream pool-riffle unit via backwater, which induces upstream riffle deposition and ultimately prevents the formation of a flattened bed. The second is that as the deposition occurs in a riffle, the probability of flow reversal in the same pool-riffle unit is reduced, which prevents unbounded riffle deposition. These two mechanisms control the height differences of two contiguous riffle crests.

While de Almeida and Rodríguez (2011) focus on sediment transport and the role of fractional transport in shaping pool-riffle dynamics, Church (2006) provides a broader framework for understanding how sediment transport processes influence alluvial channel forms. Church's approach, emphasizing both forward and inverse methods, extends these concepts by offering a detailed analysis of sediment transport using a variety of equations and models that further deepen the understanding of river morphology and sediment movement. In Church (2006), the goal is to understand and explain how different properties of channels and different sediments are associated with certain alluvial channel forms. This problem can be approached in two ways. The forward approach is using the known physics of sediment transport to deduce some conditions of fluvial sedimentation. The second approach is the inverse approach, which uses the observed properties of stream channels and fluvial sediments to make inferences about the sediment transport process. River morphology and river sediments are much more easily observed than sediment transport and can yield quite detailed results on along-channel variations in transport, hence morphology, but is not yet so physically rigorous.

Church uses the continuity equation along a streamline that can be described as

$$\frac{\partial q_{bx}}{\partial x} + \frac{\partial}{\partial x}\left[k_y\left(\frac{\partial C_b}{\partial x}\right)\right] + (1-p)\frac{\partial z}{\partial t} + \frac{\partial C_b}{\partial t} = 0, \tag{2.14}$$

the first term gives the change in transport with distance along the streamline, the second term gives the effect of sediment lateral diffusion, the third term gives the deposition or erosion, and the last term gives the change in sediment concentration over time (Church 2006). Church further simplifies this equation to a one-dimensional equation by averaging the cross-sectional changes:

$$\frac{\partial Q_b}{\partial x} + (1-p)\frac{\partial A_b}{\partial t} = 0, \tag{2.15}$$

where $A_b = wdz$ and is the net erosion or deposition in a cross-section with a width of w. This is very similar to the Exner equation, which is the one-dimensional form of the equation above. The Exner equation is

$$\frac{\partial q_b}{\partial x} + (1-p)\frac{\partial z}{\partial t} = 0. \tag{2.16}$$

Upon integration, the equation for a traveling wave is obtained:

$$q_b = (1-p)v_b\langle h\rangle dw + C, \tag{2.18}$$

where v_b is the bedform migration rate, $\langle h\rangle$ is the average bedform height, dw is the unit width, and C is a constant of integration. Church then asks two critical questions: What is the magnitude of C?, and how can C be determined? Church concluded that there is a need for a more critical and thorough study of these questions.

The equations that represent the sediment balance for a river with no large tributaries can be expressed as

$$(1-p)\Delta V + (Q_{bo} - Q_{bi})\Delta t = 0, \tag{2.19}$$

where $\Delta V = V_i - V_o$, and V_i is the volumetric sediment input and $V_o$is the volumetric sediment output. This equation is helpful for the deformation of channels. To calculate sediment transport in a channel, the sediment influx or efflux must be known. Another variable that could make computing sediment transport possible is the sediment path length. If particle path length is known and, in addition, the depth of the active layer is known, then sediment transport can be estimated as

$$Q_b = v_b d_s w_s (1-p)\rho_s, \tag{2.20}$$

in which $v_b = L/T$ is the virtual velocity of the particles, L is the clast path length, T is the elapsed time between observations, and w_s is the active width of the channel bed. Particles tend to accumulate at bars and the particle average distance traveled for transporting sediment is from bar to bar. Church also noted that more observations are needed, but this conclusion represents an important regularity in the relation between sediment transport and river morphology.

When applying the Inverse Methods, the sand load is twice the magnitude of the gravel load and estimating the total sediment transport is challenging because of the wash load (this makes the magnitude of the bed load smaller). In rivers with fine-grained sediment, i.e. sand, the sediment load moves primarily in suspension. Church then concluded that for a successful application, the method must be adapted to the deformation style of each major transport regime type, lending added significance to the appropriate classification.

Building on Church's (2006) exploration of sediment transport and channel properties, Dunne and Jerolmack (2018) further investigate how gravel-bedded and sand-bedded rivers may represent distinct equilibrium states or a continuum of transport regimes. Their work highlights the transition from gravel-bedded to sand-bedded conditions and introduces new classifications of threshold and near-threshold channels, which challenge existing models of river behavior and sediment dynamics. Dunne and Jerolmack (2018) attempt to answer the following questions: Do gravel-bedded rivers and sand-bedded rivers have separate equilibrium states? Or do alluvial rivers show a continuum of transport regimes? Dunne and Jerolmack show the transition from rivers that can be explained entirely by Parker's theory, where channel beds and banks are composed of uniform material transported by only bed-load, to channels that cannot. In natural rivers, this transition commonly occurs from gravel-bedded to sand-bedded conditions. Parker (1978) recognized that riverbanks that are stable are not compatible with transport. The transverse slope causes a net flux away from the banks, which then leads to erosion and widening of the channel. Dunne and Jerolmack further express that suspension channel theories have not provided a satisfactory description of sandy river channel geometry and that there is no acceptable model for the equilibrium geometry of river channels far above the threshold. Dunne and Jerolmack classify channels as either threshold channels or near-threshold channels.

Threshold channels are channels where the flow reaches a critical velocity or shear stress and just initiates the movement of sediment. Near-threshold channels are channels where the flow is just above the threshold but is not enough to maintain sediment movement and causes intermittent sediment transport. Sand-bedded rivers commonly form near-threshold channels and show a large offset from the gravel-bedded river trend and the threshold channel predictions. Yet, sand-bedded rivers do not behave differently from gravel-bedded rivers. Sand-bedded rivers also have a higher bank-full Shields stress than gravel-bedded rivers. Dunne and Jerolmack find that the bimodality in Shields stress and transport stage is mirrored by a comparable bimodality in riverbed grain size. Along a longitudinal river profile, Dunne and Jerolmack found that the Shields stress increases as the bed goes from gravel to sand, the fluid shear stress declines downstream, and the width slightly decreases downstream. It was discussed that to maintain a "suspension river" like most natural sand-bed channels, the banks must be composed of cohesive sediment with a significantly higher entrainment threshold than the bed material. So larger sediment grains are harder to move because of their mass, but smaller sediment grains are harder to move because of their cohesivity. Consideration of the slope or grain size dependence of the critical Shields stress shows that alluvial rivers are bimodal in terms of transport stage and bed-material grain size and that these modes correspond generally to bed-load gravel rivers and suspension sand rivers.

Following Dunne and Jerolmack's (2018) exploration of the dynamics between gravel-bedded and sand-bedded rivers, Bridge (1993) shifts focus to the development of braided rivers, examining the processes that shape their origin, flow, and sediment transport. By emphasizing the importance of temporal and spatial data, Bridge highlights the role of discharge variations, sediment supply, and bank erosion in determining channel patterns and the morphology of braided rivers. Bridge (1993) reviews the current knowledge of the origin, geometry, flow, sediment transport, erosion, and deposition of modern braided rivers and uses that knowledge to construct qualitative and quantitative models for braided rivers. But to construct valid, adequate predictive models, it is crucial to have information on the variation of flow, sediment transport, and bed geometry over time. This is to predict erosion and deposition associated with channel bars and fills. It is crucial to have historical data on modes and rates of bank erosion, channel bar migration, channel cutting, and channel filling. Lastly, it is crucial to have 3D variation of bed geometry, grain sizes, sedimentary structures, and paleo currents throughout the channel belt deposits. Channel patterns can form from a straight erodible alluvial channel. How this formation can start is that the channel bed can build towards a constant geometry that has single or multiple rows of bed waves. These bed waves are in equilibrium with steady hydraulic and sediment transport conditions. After these bed waves form, the banks start to erode, and the channel widens. This causes the water level to drop, and the highest sections of alternate bars begin to emerge. This will cause sediment deposition and form braid bars or point bars. Braid bars are a result of the accumulation of sediment in the middle of the channel. Point bars are a result of the accumulation of sediment that forms banks on the inside of river bends. The basic geometry of point and braid bars is controlled by channel-forming discharge. The main braiding mechanisms that were observed by the Bridge in the laboratory and natural rivers are the development and emergence of individual rows of alternate bars and the formation of crossbar channels.

The main differences between a bar and an island are vegetation and whether it is submerged at bankfull or emergent at bankfull. Near-bankfull flow patterns control the formation of bars but the falling stage controls the geometrical features. The difference between braiding and anastomosing is that braiding is splitting around bars or small islands of sediment deposits; whereas anastomosing is splitting around islands that are more resistant to erosion, such as those with cohesive banks. The two channels created when a channel is anastomosing have independent flows. And anastomosing channel segments can be straight or braided.

Generally, what controls channel patterns are the supply of water and sediment and the valley slope. Channel pattern is also influenced by bed-material size, where braiding happens at lower slopes and/or discharges as the grain size decreases. For experimental purposes, Bridge (1993) suggests the most appropriate discharge to use is a flood discharge that does not depend on a reference to channel geometry, such as a frequency-based measure like the one- or two-year flood. Valley slope should be used instead of channel slope to avoid biasing the plotting positions of sinuous streams, which have a lower channel slope than valley slope (Bridge, 1993). Different researchers have classified rivers that are near transition from meandering to braided rivers in different ways. An increase in discharge, width or depth, and sediment transport that are associated with great floods may influence a major change in the pattern of the channel. The variability in discharge impacts sediment transport, erosion, and deposition in all alluvial river types, especially braided rivers. The hydraulic measures that are also known to affect sediment transport are bed shear stress, stream power per unit bed area, and stream power per unit channel length. But this also depends on what type of sediment is available and what proportion of the total bed shear stress or power is available to transport sediment in the presence of rough banks and bedforms (Bridge, 1993). The stream power per unit channel length is where the fluid density and gravity control the width-integrated sediment transport rate. This also depends on the grain sizes available for transport and the bedform drag. The total sediment transport rate must be equal to the sediment supply in a river that is at equilibrium. However, a drastic change in sediment supply to a reach may cause a change in the channel pattern. Streams that have large bedload transport in proportion to suspended load transport are called bedload streams. These bedload streams are associated with easily eroded banks, large channel slope and stream power, and are laterally unstable. Streams that have large, suspended load transport in proportion to bedload transport are called suspended load streams. These streams are associated with cohesive, muddy banks, low channel slope and power, and are laterally stable. Although, it has been claimed that the correlation between sediment size, type of sediment load, and channel pattern is not generally supported. In general, vegetation supports stabilizing cut banks and bar surfaces. However, there is no important influence on the equilibrium channel pattern. It is challenging to measure and calculate the total and local sediment transport in braided rivers. This is due to temporal and spatial variability. Around a curved section of the channel, the bedload transport tends to move coarser sediment to the outer bank of the curve and finer grains tend to move towards the inner bank. Higher bedload transport rates can occur where lower bed shear stresses act on sandy beds. In sand-bed streams an increase in bed shear stress may result in an increase or decrease in bedform height/length (hence form drag) such that the bed shear stress effective in bedload transport may decrease or increase. Normally, the bed sediment is finer downstream on the tops of braid bars and point bars and is relatively coarse in the deepest parts of the channel. It

has been observed that when flow stages are lower than bankfull, dunes form shorter and lower, and the proportion of curved crested dunes decreases in relation to straight-crested dunes. The mean geometry of the dune and the rate of migration changes in response to the changing flow conditions with a small time lag had also been observed.

The erosion and deposition at the bar scale are related to three main processes. The first process is the result of seasonal changes in discharge; in which case the bed topography of braid and point bars adjusts. The second process is bank erosion and deposition on adjacent bar margins (channel migration) and is generally associated with the adjustment of bed topography in braided and point bars caused by seasonal discharge changes. The third process is the cutting of new channels, enlarging of existing channels, and abandonment and filling of channels, and is related to the second process. These processes are all related to each other. Erosion and deposition are due to gradients of sediment transport rate (Bridge, 1993). This is given through the sediment continuity equation:

$$-C_0 \frac{\delta h}{\delta t} = \frac{\delta i_s}{\delta s} + \frac{\delta i_n}{\delta n} + \frac{1}{u_s}\frac{\delta i_s}{\delta t} + \frac{1}{u_n}\frac{\delta i_n}{\delta t}, \tag{2.21}$$

where C_0 is the volume concentration of sediment in the bed, h is bed elevation, t is time, s and n are streamwise and cross-stream space coordinates, i_s and i_n are streamwise and cross-stream sediment transport rate by volume, and u_s and u_n are corresponding mean velocities of sediment grains (Bridge, 1993). As the discharge varies, the topography of the bed is always out of equilibrium with flow. The two factors that control bank erosion are the resistance of banks to slumping and the ability of the flow to remove the slumped material. The shear strength of the bank material, τ_s, can be calculated by

$$\tau_s = C + P\mu_c, \tag{2.22}$$

where C is the cohesive strength, P is effective normal stress and μ_c is the static friction coefficient. The factors that affect the cohesive strength are the presence of clay materials, vegetation, and cemented layers. The factors that control effective normal stress are the weight of the potential slump and excess pore pressure. When the banks have large shear strength, τ_s is expected to be large as well, thus preventing erosion. However, theoretical approaches are overly simplistic in that they do not consider flow unsteadiness and the unpredictable entrainment stresses of slump blocks. Bridge concludes that extensive field and lab studies over time on variation and relation of geometry, flow, sediment transport, erosion, deposition, and channel migration will help progress the understanding of braided river processes. The development of theoretical models that can be tested with extensive data can also progress the understanding of the processes of braided rivers.

While Bridge emphasizes the importance of understanding sediment transport and channel dynamics for predicting braided river behavior, Yu and Lim (2003) focus on the modeling of flow velocities over bedforms, highlighting a more technical approach to understanding flow resistance in alluvial channels. Building upon the foundation of sediment transport and hydraulic principles established by Bridge, Yu and Lim (2003) introduce a more specific methodology for

predicting depth-averaged flow velocity and the factors influencing bed resistance in such dynamic systems. Yu and Lim (2003) investigate the bed resistance of two- dimensional flows over bed forms for all flow regimes, and an accurate formula to predict depth-averaged flow velocity that is applicable for the entire flow regime in alluvial channels with bedforms is developed. Yu and Lim's procedure utilizes Manning's equation to calculate the flow (velocity or discharge) in an alluvial channel:

$$U = \frac{1}{n} R_b^{2/3} S^{1/2}, \tag{2.23}$$

where U is the depth-averaged velocity, n is the Manning's bed roughness coefficient, R_b is the hydraulic radius of the channel bed, and S is the energy slope. The energy slope could be equal to the channel slope to keep calculations simple. The Manning's n changes as the bed changes. For sand-bedded rivers Manning's n can be calculated by using $n = d_{50}^{1/6}/19$, this is about 9% larger than the Strickler equation. The Strickler equation is used for a flat bed composed of non-erodible granular material. The Strickler equation is

$$n = \frac{d_{50}^{1/6}}{6.7\sqrt{g}}, \tag{2.24}$$

where d_{50} is the median sediment size and g is the gravitational acceleration. Substituting the Strickler equation into the Manning's formula results in:

$$U_r = 6.7\sqrt{g d_{50}} \left(\frac{R_b}{d_{50}}\right)^{2/3} S^{1/2}, \tag{2.25}$$

where U_r is the depth-averaged velocity for rigid channel bed. This equation can be used for a flat-bed channel with non-erodible material or loose bed material where the flow strength is too weak to dislodge the granular particles. But once the flow rate is high enough to move the sediment and develop bed forms, the bed resistance changes. In this situation, Manning's n, which was estimated before, is no longer relevant and changes with flow depth, flow strength, and sediment size. The calculation procedure for accurate depth-averaged velocity starts with the known discharge, water surface slope, channel width, median sediment size, and sediment gradation. First, a water surface elevation can be assumed, and flow depth, flow area, and velocity can be calculated. If the aspect ratio is less than 10, the equation

$$R_b = \frac{QB^2}{UB^3 + 0.055Q}, \tag{2.26}$$

is used to calculate R_b. Otherwise R_b=h. The next step is to calculate the critical shields parameter with

$$\theta_{cr} = 0.056 - 0.033e^{-0.0115 d_{gr}} + 0.1e^{-0.25 d_{gr}} + e^{-2 d_{gr}}, \tag{2.27}$$

With the critical shields parameter, the ratio of the Shields shear stress parameter with the critical shields parameter θ/θ_{cr} can be found. Then the flow regime is identified by

$$(1000S)q_*^{0.2}\sigma_g^{0.2} = \begin{cases} 0.2413d_{gr}^2 - 2.385d_{gr} + 17.52 & d_{gr} < 14 \\ 3.805\left(d_{gr} - 14\right)^{0.2} + 30.44 & d_{gr} \geq 14 \end{cases} \quad (2.28)$$

where $q_* = Q/\left\{B\sqrt{(\gamma_s/y - 1)gd_{50}^3}\right\}$ and $d_{gr} = d_{50}(g\,(\gamma_s/y - 1)/\nu^2)^{1/3}$, and ν is the kinematic viscosity of water. The next step is to calculate χ and ξ. To calculate χ use $\chi = \ln(\theta/\theta_{cr})$. To calculate ξ use

$$\xi = \begin{cases} 1 & R_b/d_{50} > 300\chi \\ \left(\dfrac{300\chi}{R_b/d_{50}}\right)^{0.1} & R_b/d_{50} \leq 300\chi \end{cases} \quad (2.29)$$

If $1 < \theta/\theta_{cr} < 250$ and the flow is in a lower flow regime use $\lambda = -0.0044\chi^3 + 0.0661\chi^2 + 0.352\chi + 1.0$ to calculate λ. But if $7.5 < \theta/\theta_{cr} < 250$ and the flow is in an upper flow regime use $\lambda = -0.0337\chi^3 - 0.4687\chi^2 + 1.916\chi - 1.644$ to calculate λ. Finally, compute the new depth averaged velocity with

$$U = 6.7\xi\lambda\sqrt{gd_{50}}\left(\frac{R_b}{d_{50}}\right)^{2/3} S^{1/2}, \quad (2.30)$$

The goal with this computation process is to get the new depth averaged velocity to match the velocity that was calculated at the beginning of the process. If they are not equal or close enough to be equal, a new water surface elevation is assumed, and the process is redone.

While Yu and Lim (2003) focus on modeling flow velocity and bed resistance in alluvial channels with bedforms, their approach sets the stage for understanding the dynamics of sediment transport in such systems, a concept further explored by van Rijn (2007). Building on the principles of sediment transport and flow resistance, van Rijn delves deeper into the complexities of bed roughness and its impact on sediment movement, especially in channels with a range of bedform regimes. van Rijn (2007) describes a model framework for the sediment transport of fine silts to coarse sand and gravel. The erosion or pickup process of the sand particles is slowed down by the presence of clay-silt particles. Natural sand-bedded or finer sediment beds have lower densities, and thus natural channels of these types have lower critical bed-shear stress. With the lower densities and critical bed-shear stress, the cohesive effects are crucial for the finer sediments. van Rijn discusses the basic problems in the prediction of sediment transport, one being the prediction of bed roughness. The bed roughness, in turn, depends on the sediment transport generated by the bed forms migrating over the bed. The bed form regimes for a steady flow over sand-bedded channels can be classified as lower transport regime, transitional transport regime, and upper transport regime. The lower transport regime is with a flat bed, ripples, dunes, and bars. The transitional regime is with washed out dunes and waves. The upper transport regime is with flat mobile beds and anti-dunes. The bed forms created at low velocities are washed out by higher velocities. However, it is unclear if the

bedforms are washed out by a decrease in the bed form height, an increase in the length of the bed form, or both. Bed load transport is affected by the grain roughness in steady-flow rivers, and bed roughness overall has a large influence on bed load transport in the case of larger flows.

Building on van Rijn's (2007) discussion of sediment transport and the influence of bed roughness, Smith (1971) examines how specific river systems, like the Niobrara River, exhibit similar dynamics, particularly with respect to discharge variations and sediment transport processes. Smith highlights how factors such as flow conditions and shifting bar formations play a significant role in altering the river's morphology and sediment distribution, further illustrating the complexities of sediment transport in braided river systems. According to Smith (1971), the Niobrara River is like the Lower Platte River in terms of width, flows, transverse bars, and braiding within the river. The discharge is high between the months of March and June, and the discharge is low in August and September. During the high flows, the bed is completely covered, and there is no braiding. Braiding occurs at intermediate and low flows when the river is choked with shifting bars and shallow anabranches which vary considerably in number and size. The braiding develops during the low flow months, the channel depths are very shallow, and the thalweg flows against the cohesive vegetated banks. In the thalweg, the depth can be up to 2 meters deep. Transverse bars vary in surface area and are subject to nomenclatural inconsistencies. Once the transverse bars are formed, the bars have a great effect on the local water surface slope. The steeper water surface slopes tend to occur over bars with the shallowest depths. Sediment is transported over the bar surface to its margins by small-scale bed forms ranging from ripples to anti-dunes. At the transverse bar mouth, in the stronger currents, more sediment is transported via suspension. The finer sediments are transported more quickly than coarse sediments; hence, there are finer sediments downstream.

2.3. Ice Erosion

Beltaos and Prowse (2001) discusses how river ice jams can cause extreme flood events that impact the economy, ecosystem, and close by communities. Because ice jams can become very thick (up to several meters), the water level has to accommodate for the river flow and the ice. In order to accommodate both the large additional resistance created by this new boundary and the keel of the jam, itself being a large part of the thickness. The gravity flow under the ice cover in terms of open-water depth with a set discharge can be described by the following equation:

$$\frac{Y_{cov}}{Y_{op}} \approx \left[1 + \left(\frac{n_i}{n_b}\right)^{\frac{3}{2}}\right]^{\frac{2}{5}} + 0.92\frac{h}{Y_{op}}, \tag{2.31}$$

where Y_{cov} is the water depth in ice-covered conditions, Y_{op} is the water depth in open water conditions, h is the thickness of the ice-cover, n_i is the Manning's roughness for the bottom of the ice-cover and n_b is the Manning's roughness for the riverbed. On the right-hand side of the equation, the first term denotes the ratio of the under-ice depth of flow to the open water depth and the second term denotes the ration of the submerged thickness of the cover to the open water depth. Ice jam flooding is sudden and allows little time in which to plan and implement mitigation measures or evacuation of local residents. The release of an ice jam creates a surge, which is when a large volume of water comes out at once. This is compared to a dam break. The

ice jam surges can cause a dramatic increase in stage and very high flow velocities that are capable of bank erosion and bed scouring.

According to Beltaos and Prowse, ice jams occur during both the freeze-up and the breakup periods. Since the stage and the flows are not as high, the ice jams during the freeze-up period do not cause as much damage as the breakup ice jams do. Beltaos and Prowse concentrate on the breakup ice jams, as they are the main cause of extreme ice-related events. The breakup period can be conveniently visualized in distinct phases such as pre-breakup, onset, drive, and wash. During the pre-breakup phase, the ice cover starts to become more vulnerable to fracturing and movement due to the thermally included reductions in thickness and strength. The onset phase happens around the same time, but the warming weather causes the snow and ice to melt, increasing the discharge and water level. The rise of the water level forces the ice to detach from the banks. The onset is governed by many factors, including channel morphology, which is highly variable along the river. The onset is followed by the drive, which is the current "driving" the ice fragments downstream. Ice jamming happens when there are areas of the river where the ice cover has broken up and starts to move downstream to an area of the river where the ice cover has not started the breakup process. When the ice jam finally breaks through, the surge begins. Any intact ice cover could be broken up by the surge, or it might stay in place and cause another ice jam. This process keeps going until the final ice jam is released. Then, the wash, or the final clearance of the ice, begins.

Beltaos and Prowse conclude that river ice processes, in particular the ice breakup and jamming, are determined by three factors: the flow hydrograph, the thickness of the winter ice cover, and the stream morphology. The river ice can be a key factor in geomorphological change in channels. It is known to create numerous erosional and depositional features within river channels and on-channel floodplains. Beltaos and Prowse provide an example of a study that found breakup events can produce sediment concentrations that are compared to flow events of between 2-5 times greater discharge in open-water conditions. This can be from bank erosion and from the ice carrying the sediment downstream.

Following Beltaos and Prowse's (2001) analysis of ice jam-induced flooding, Beltaos (2016) further explored how ice breakup influences sediment concentrations and loads. His research revealed that the release of ice jams, or javes, amplifies the erosive power of the flow, creating significant sediment pulses that can substantially alter sediment transport dynamics in rivers. Beltaos (2016) did a further study on how ice breakup affects sediment concentrations and loads. For this study, Beltaos attempted to find data sets on breakup sediment pulses and their relationships to javes and associated ice runs; and to assess the magnitudes of pulse concentrations and loads. Javes are waves created by the release of ice jams. The effect of the ice breakup process on suspended sediment transport in rivers, based on the results, is the creation of sediment pulses. These pulses are caused by the amplified erosive capacity of the flow during the passage of javes, while as many as three pulses per site have been observed during a breakup event observed by Beltaos. Depending on the intensity of the ice run that ensues upon ice jam release, the peak of the pulse may coincide with the peak of the jave (moderate runs) or occur before it (heavy runs) (Beltaos, 2016). Beltaos used the Rising Limb Analysis Method (RLAM),

which utilizes the St. Venant equations of motion to determine velocity, discharge, and shear stress based on measured water level-time variations along the rising limb of the jave (Beltaos, 2016). The following equation applies to the rising limb of a jave:

$$\frac{\partial y}{\partial t} \approx \frac{C\left(S_f - S_e\right)}{1 - a\frac{U^2}{gh} + \frac{C^2}{gh}\left(\frac{(1+a)U}{C} - 1\right)}, \tag{2.32}$$

where S_f is the friction slope calculated from Manning's equation; t is time; U is the average flow velocity; C is celerity of the waveform; y is the water depth calculated by taking the "virtual bed invert" elevation and subtracting that from the water surface elevation; h is the average flow depth, which varies in proportion to y so that $h = ay$; a is the site or reach specific dimensionless coefficient that depends on the shape of the channel cross-section ($a = 1$ for simple rectangular channels and $a < 1$ for natural bathymetries). The "virtual bed invert" is defined as the elevation intercept of a linear fit to a plot of average depth versus water surface elevation. The value S_e is quantified with

$$S_e = S_{wo} + \frac{aU^2}{gh}(S_o - S_{wo}), \tag{2.33}$$

S_{wo} is the pre-jave water surface slope; and S_o is the normal water slope (slope of the water surface under steady flow conditions, or the bed slope in the condition of a prismatic channel). Using the continuity equation, U, can be expressed as,

$$U = \frac{q_o + \int_{y_o}^{y} C dy}{h}, \tag{2.34}$$

where q_o and y_o are the pre-jave discharge per unit width and the flow depth, respectively. The integration indicates that C is not assumed to be constant, but changes along the waveform, a property that is responsible for the looped appearance of the stage-flow variation during the passage of the wave. Now $\frac{\partial y}{\partial t}$ can be computed as a function of y and the numerical integration process is programmed into a spreadsheet, and calculations and measurements can be compared instantly. The sediment pulse loads were estimated using the RLAM on four occasions where sufficient concentration data were available in order to fully define the associated suspended sediment concentration-time curve (Beltaos, 2016). For heavy runs, the pulse loads can amount up to 25% of the total carrier load during a breakup event. The carrier load is the suspended particles that are transported by the water in the ice jam/breakup. For moderate runs, the net pulse loads were less than 10% of the carrier loads. The sediment concentrations and net loads transported by pulses depend heavily on carrier river discharge and sediment availability.

Building on Beltaos' findings, Turcotte et al. (2011) explored the intricate ways ice dynamics influence sediment transport in rivers. They highlighted how various ice forms, such as frazil ice, bankfast ice, and anchor ice, interact with sediment supply and transport, often leading to

dramatic changes in sediment movement and channel morphology. Turcotte et al. (2011) document a range of unique ice and sediment transport processes and how much of a role ice plays in the sediment transport process. Sediment transport is often associated with physical parameters such as shear stress or stream power. These parameters are affected by water properties. The water density remains constant year-round in most rivers that are affected by ice, but the kinematic viscosity increases rapidly with decreasing temperature. The kinematic viscosity of the cool water affects the sediment transport process in terms of sediment transport capacity, rates, and the increase in flow drag on bed particles slowing the fall velocity of suspended particles. Another effect the cooling of the water has on sediment transport is when the river starts to freeze up, frazil ice particles form and are carried with the flow of the river. The drop in suspended sediment is linked to this type of event. A key source in providing sediment to river channels is the banks. Their stability depends on numerous interrelated factors including soil saturation, material cohesion, bank slope, sediment size distribution, and water table elevation. The freeze-thaw cycle affects the stability of the banks, thus affecting factors of the stability. How much the soil is saturated before freezing influences how much the bank will weaken during the freeze-thaw cycle. In mild climate conditions, there are repeated freeze-thaw cycles through the winter season. The repeated freeze-thaw cycles result in weaker banks. Meanwhile, snowmelt and rain-on snow events contribute to modifying the hydraulic gradient in riverbanks and water levels in the river channel. How the freeze-thaw cycle affects sediment transport is by increasing the sediment supply to the channel, especially before the spring freshet period. Bankfast ice is where the formation of the ice occurs from the bank material and any emerging bed material by the slow-flowing water. Bank material and bed material tends to get trapped in the ice and when the ice breaks away, it takes all the sediment with it. How bankfast affects sediment transport is it protects the bank and surrounding bed material from being eroded during the winter. When the water levels and velocities change, the ice can break away with the bank and bed material, revealing the weaker material, which can lead to drastic erosion. Ice-rafted particles released from bankfast ice flows will likely remain in the water column if enough turbulence is present (fine material) or will randomly settle to the bed (coarse material). However, the distance that the sediment transport travels depends on the hydrological, hydraulic, and weather conditions. Another ice process that affects sediment transport is stable ice cover. Stable ice cover causes the water velocity to drop because of the added rough boundary at the surface of the water. Due to the reduction in average velocity, the water depth will increase. Given that the total shear boundary affecting ice-covered flows must be divided between the water-bed and water-ice interfaces, a reduction in shear stress at the bed can be expected. Once stable ice cover forms, the bedform changes shape and celerity. These changes suggest that bedload transport rates decrease once a stable ice cover is formed. The flow depth influences dune wavelength and height but not the ripple geometry. The flow intensity and particle size affect the dune steepness. The effect of stable ice cover on sediment transport over time depends on how long the ice cover stays stable. The upstream hydraulic effect of a stable ice cover is limited to its backwater region and there is almost no hydraulic influence of the cover past its downstream edge. Anchor ice is commonly in turbulent channels where ice particles stick to the riverbed and accumulate, or when the ice grows in place on the riverbed. The effects of anchor ice on sediment transport are that it creates a wall that interferes with bedform migration and

shields bed material and prevents the entrainment of particles by flowing water. In that sense, anchor ice temporarily reduces the sediment available for transport. But anchor ice usually forms during the falling limb of a hydrograph or in stable hydraulic conditions, so the capacity of sediment transport is reduced already. The main documented effect of anchor ice on sediment transport occurs when anchor ice is released from the channel bed. When anchor ice is released, it is a natural sediment transport and scavenging agent. The formation and sudden breaking of ice dams and anchor ice dams have compound effects on sediment transport through dynamic ice action and through repeated high discharge pulses. Ice processes are key in changing and sculpting channels in different ways than unfrozen water.

3. Study Site

3.1. Introduction

The primary site for this study is the Highway 281 bridge across the Niobrara River, north of O'Neill, Nebraska. For many years, the bridge at this location has been partially shielded from high flows and ice jams by Spencer Dam, which was located immediately upstream of the bridge. Spencer Dam was a low-head dam with a drop of only about 25 ft. It was a run-of-the-river dam with very little storage, but it did reduce sudden surges in flow. More importantly, since its construction in 1927, the dam restricted outflow to a narrow channel on the north side of the active flow area. This allowed a relatively short bridge (compared to upstream and downstream bridges) to be built across the river. The reservoir behind the dam stored a large amount of sediment and reduced downstream sediment during low flows. The narrow channel downstream of the dam also allowed sediment to be more effectively transported past the Highway 281 bridge during sediment flushing events.

This changed in 2019 when a massive ice flow breached the dam and destroyed the approach to the Highway 281 bridge. Destruction of the dam has resulted in a wider channel, one that is similar to upstream and downstream reaches of the river that were comparatively unaffected by the effects of the dam. In this chapter, information about the physical characteristics and hydrology of the site is presented.

3.2.Site Description

3.2.1.Highway 11 to Highway 281

Figure 3.1 shows aerial imagery of the Niobrara River between Highway 11 and Highway 281 collected from NAIP (2022). This aerial-mosaic is from the month of August 2022. In Figure 3.1, bedforms in the channel are unsubmerged because the discharge is low, and the amount of visible sediment in the channel and the floodplains between the two bridges is significant. The distance from Highway 11 to Highway 281 is just over 18 kilometers. The remnants of Spencer Dam are located immediately upstream of the Highway 281 bridge shown in the lower right corner of Figure 3.1. Prior to failure, the backwater of the dam is estimated to have extended between 6 and 10 km upstream of the dam, based on residual sediment deposits.

The complete study reach is from Highway 11 to 503rd Avenue, a distance that is approximately 40 km. Appendix C provides details of aerial imagery of the site from 2018 to 2024 for the entire reach of the Niobrara on the Boyd and Holt County lines. This covers the entire study area with additional reach length on the upstream and downstream sides. Additional detail is provided in four aerial images of the site that show how erosion of the available sediment in the reservoir has progressed prior to and over the duration of the study period. Appendix C also shows that it is reasonable to estimate sediment storage in the reservoir based on a 6 km reach upstream of the dam.

Figure 3.1 Overview of Highway 11 to Highway 281(NAIP, 2022)

3.2.2. Niobrara River at Highway 281

An enlarged image of the study site is shown in Figure 3.2. In this aerial, sediment movement at the site is more clearly visible. In places, the channel is a single filament, but for higher flows, the channel braids. For very high flows, it transforms into a wide active alluvial channel that can transport large quantities of sand.

Figure 3.2 NAIP (2024) aerial of the 7 km reach upstream of Highway 281

3.3. Hydrology

Figure 3.3 is a watershed map of the Niobrara above Highway 281. The watershed is long and narrow and covers an area that stretches from within Wyoming to the Highway 281 bridge. The watershed contains contributions from parts of Wyoming and South Dakota, but the vast majority of the watershed is within Nebraska.

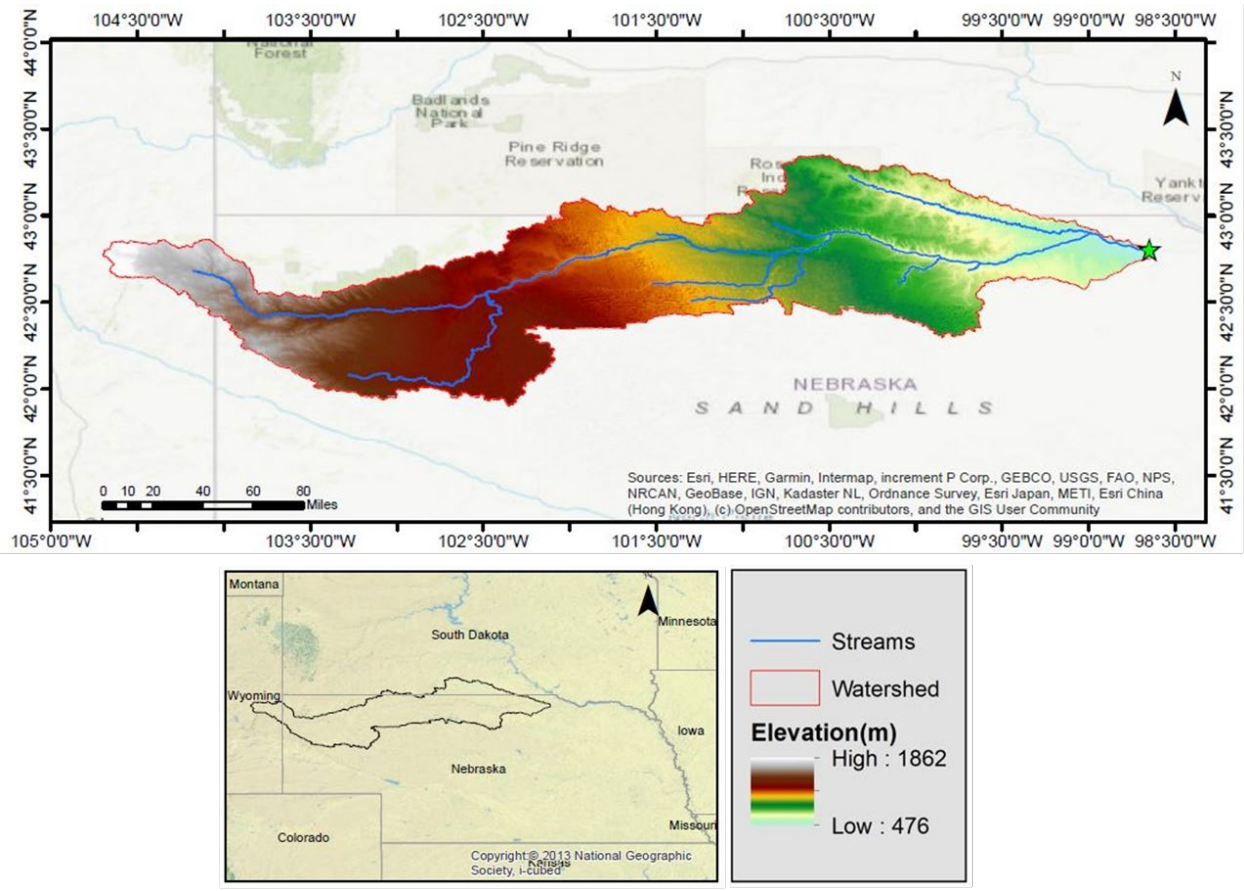

Figure 3.3 Watershed map for the Spencer/Highway 281 site.

There are two stream gages that are particularly relevant in the present study. There is a gage at Highway 11, near Butte, Nebraska that is located at the start of the study area (gage 06464930). There is another gage that is located near Verdel, Nebraska, downstream of the study area (gage 06465500). While the Highway 11 gage is the closest gage to the study site, it was installed by NDNR in 2010 and only has about 14 years of data. The USGS gage, on the other hand, is located farther down from the study site but has over 60 years of data.

Figure 3.4 is a Log-Pearson Type III plot of the Verdel data made with HEC-SSP 2.3 following USGS Bulletin 17C. The highest and second highest annual peak flows on record at Verdel are from 2019 and 1960, respectively. The sixth highest flow is from 1966. Baker et al. (2020) indicate that all of these flows were the result of spring ice jams, and all of them resulted in damage to Spencer Dam, with the last ice run in 2019 destroying it. Based on USGS records at Verdel, the flow rates for these three events were 123,000; 39,000; and 16,000 cfs, respectively. According to Baker et al., Spencer Dam also failed in 1935 as the result of a spring ice jam, but this was prior to the collection of flow records at Verdel. Based on the data collected from Verdel by HEC-SSP, 46 percent of the peak flows at Verdel are from the months of February and March.

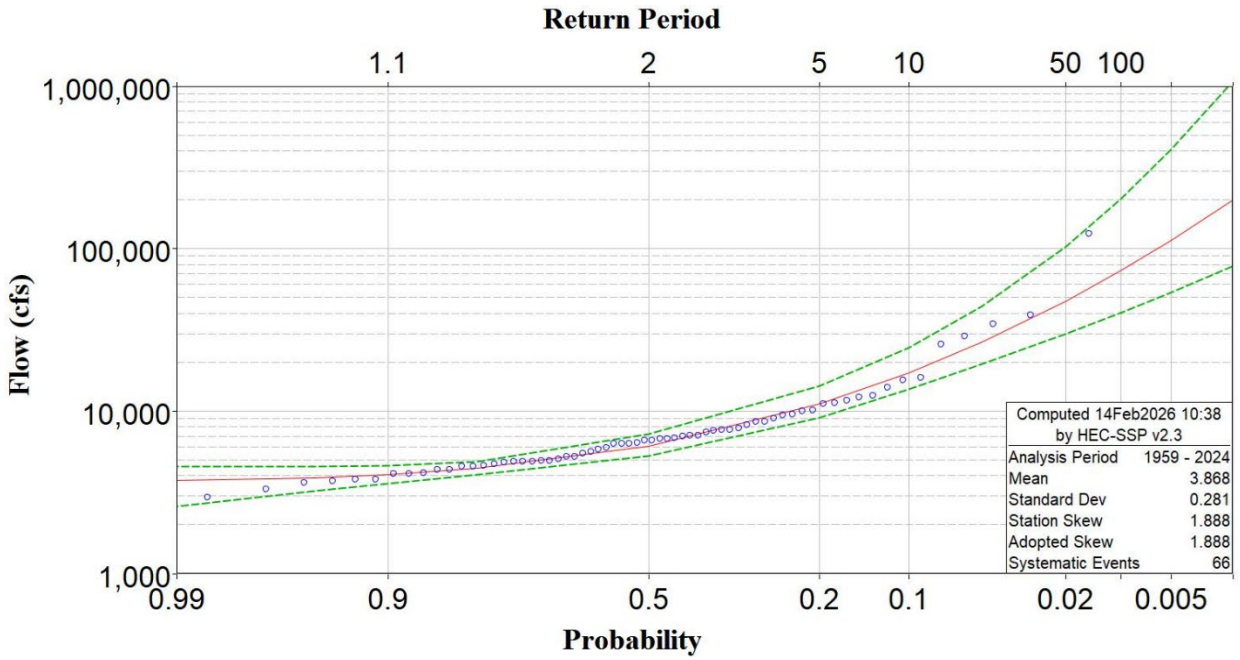

Figure 3.4 Log-Pearson Type 3 plot of Niobrara River annual peak flows at Verdel, NE

Figure 3.5 is a Log-Pearson Type III plot of the Highway 11 data made with HEC-SSP 2.3 following USGS Bulletin 17C. For these data, winter data were discarded based on information from the Verdel gage because flowrate measurements are not possible when the river is frozen. There is a problem when trying to measure flows associated with ice runs, because it is often not known if the river is freely flowing or if a high stage is associated with an ice jam. In other words, rating curves are erroneous or tenuous when the river is frozen and often during ice break up. The Highway 11 gauge has only been in operation since 2010, so there are only about 14 years of record. After discarding high flows that were potentially caused by freezing of the river, approximately 20 percent of the remaining peak flows are in February and March. The highest flow recorded at the Highway 11 site was 36,600 cfs on June 21 in 2011; the flowrate at the Verdel site was only 11,100 cfs for this event but the dam was still in place in 2011, and the flow was likely attenuated between Highway 11 and Verdel. The second highest flowrate was 22,000 cfs in March 2019. Most of the other highest peak flowrates did not occur in February or March, but it is difficult to be certain because of the discarded winter data. Quality control of the Verdel data is better and many large peaks occur right at the end of ice breakup.

When we look at the history of Spencer Dam and the flow records between 1960 and 2025, it is clear that ice flows contribute greatly to the highest and most damaging flows. Part of this is because of temporary high flows that happen when ice jams store water and then suddenly release. The flows can be exacerbated as a result of rain-on-snow events. In any case, four major events in the 100 years between 1925 and 2025 (1935, 1960, 1966, and 2019) are certainly cause for concern about the current elevation of the Highway 281 bridges. In the event of a major ice flow, the low elevation of the island between the two bridges make it vulnerable.

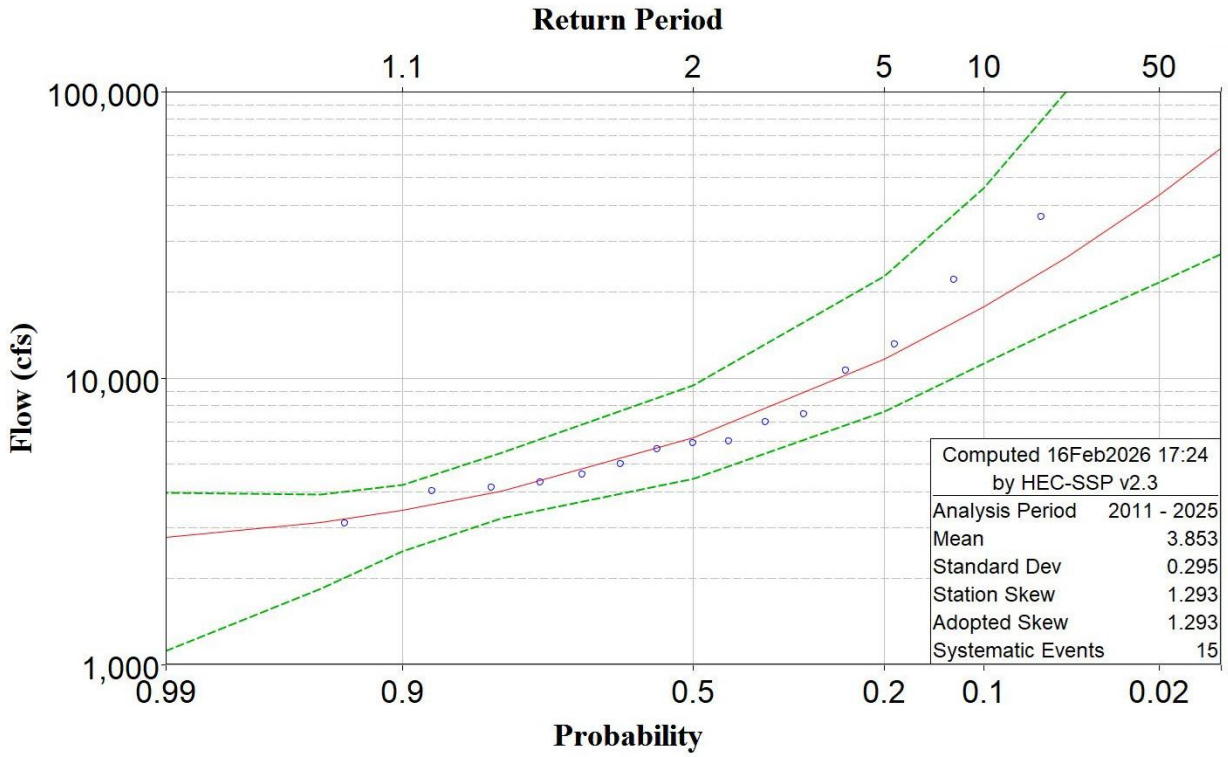

Figure 3.5 Log-Pearson Type 3 plot of Niobrara River annual peak flows at Highway 11, NE

4. Data Sources and Processing

4.1.Introduction

The previous chapter provided details about the study site. This chapter provides information about data collected from external sources, data collected at the field site, and how all of the data were prepared and processed. The chapter is divided into two parts: (1) an overview of the source data and its preparation, and (2) descriptions of individual field visits.

4.2. Source Data and Data Preparation

4.2.1.Data summary

Numerous data were collected during the project from external sources and by doing field work. Table 4.1 is a summary of the sources of data used for characterizing the topography and changes to the topography that occurred before and during the project. In this section, the sourced and collected data are presented in detail.

Table 4.1 Data retrieved from external sources and field measurements (green rows)

Data Type	***Source***	***Date***	***Description***
Aerial Imagery (1-meter resolution)	USDA NAIP (United States Department of Agriculture, 2018; 2020; 2022; 2024)	2018, 2020, 2022, 2024	Aerial imagery of Boyd and Holt counties that shows the entirety of the Niobrara River in the counties.
DEM (2-meter resolution)	NDNR (Nebraska Department of Natural Resources, 2013)	2013	Digital Elevation Model of the Niobrara River from Highway 11 to Redbird Creek pre-dam failure.
DEM (1-meter resolution)	USGS (U.S. Geological Survey, 2022)	2020	Digital Elevation Model of the Niobrara River from Highway 11 to Redbird Creek post-dam failure.
Point Cloud (1-meter resolution)	USGS (U.S. Geological Survey, 2021)	2020	LiDAR point cloud for the Niobrara River.
Orthomosaics (8-cm resolution)	Current Project	2022 (Sept.), 2023 (Mar.), 2023 (Aug.), 2024 (Feb.)	Orthomosaic imagery collected with a UAS (drone) during site visits to Highway 11 and Highway 281 bridges.
Point Clouds (2-meter resolution)	Current Project	2022 (Sept.), 2023 (Mar.), 2023 (Aug.), 2024 (Feb.)	Point clouds collected with a UAS (drone) during site visits to Highway 11 and Highway 281 bridges.
PPK GPS Data	Current Project	2023 (Aug.)	Elevations (cross-sections, longitudinal profile, and water surface elevations) collected in the Niobrara River floodplain at Highway 11 and Highway 281.

4.2.2.Aerial imagery

In Table 4.1, the aerial images that were used were NAIP images from 2018, 2020, 2022, and 2024 (NAIP, 2018 – 2024). The NAIP images were used to help identify the upstream extent of the reservoir and to identify bank erosion of reservoir deposits in locations that could not be measured with the UAS due to range limitations.

To help identify the extent of the reservoir, the two oldest NAIP aerial images (2018 and 2020) were imported into QGIS. The two images were toggled back and forth to identify the extent of

the reservoir by finding the upstream location where removal of the dam had limited impact on the channel.

For identifying bank erosion, polygons were created to represent changes in bank position from year to year based on the aerial images. For instance, a polygon was created between the bank line of the 2020 NAIP image and the bank line of the 2022 NAIP image. This method was used to identify the progression of the bank in multiple areas of erosion. The polygons were then used to help calculate available and eroded sediment volumes within the reservoir area. The results of this progression and volume analysis can be found in Chapter 5.

4.2.3. External DEMs and point clouds

In Table 4.1, the DEMs that were used in the project included Nebraska Department of Natural Resources DEMs of Holt and Boyd counties from 2013 and USGS DEMs from 2020. The 2020 USGS LiDAR Point Cloud was also used. The DEMs were used to find cross-section information, determine sediment availability, assess volumes of eroded sediment, assess longitudinal changes in the river elevation, and set up hydraulics models. The point cloud was used primarily for aligning point clouds surveyed in the current project to the same datum.

The DEMs were used to determine sediment availability and volumes of eroded sediment. In particular, the 2020 USGS DEM was used to calculate available sediment volume and eroded volume over the duration of the project in regions of the reservoir that could not be surveyed with the UAS. The 2013 DEM from NDNR was used to help estimate the initial loss of sediment caused by failure of the dam. The DEMs were also used to establish water surface elevations from the Highway 11 bridge to the 503rd Avenue bridge. This was then used as a baseline for assessing grade changes of the river.

The 2020 USGS DEM was used as the terrain basis for HEC-RAS models because of its large spatial extent. DEMs created in the current project did not cover a large enough area to be used for entire HEC-RAS models.

4.2.4. Orthomosaics

The project-based UAS orthomosaics shown in Table 4.1 were used to identify bank erosion rates at the study site, but were used primarily downstream of the dam. These images were used in conjunction with NAIP imagery in locations where both sets of imagery were available.

UAS surveys collected at the Highway 281 site cover only part of the study area – approximately 3.5 square kilometers of the river near the bridge. Extending beyond this area was not possible because of limitations in the legal range of the UAS and limited accessibility to upstream reaches. However, the data collected comprised a rich dataset, and typical surveys consisted of about 4000 images collected at a flying altitude of about 120 meters. The resulting images have a ground resolution of about 2 cm/pixel, providing detailed imagery of the site. This is much higher resolution than the NAIP images, which typically have a resolution of about 60 cm/pixel.

4.2.5. Project-based point clouds

In Table 4.1, point clouds surveyed during the current project were used to create high resolution DEMs. The DEMs were created in CloudCompare. The DEMs were used to find cross-section

information, determine sediment availability, assess volumes of eroded sediment, assess longitudinal changes in the river elevation, and set up flow models.

Similar to externally-sourced DEMs, project-based DEMs were also used to measure sediment availability and erosion downstream of the dam. Using the project-based DEMs in conjunction with USGS DEMs provided higher temporal resolution. Also similar to the NDNR and USGS DEMs, the project-based DEMs were used to establish temporal changes in water surface elevation along the length of the river. Although the observed water surface elevation adjustments were limited to a shorter reach of the river, they provided a good method for assessing changes in the local water surface over the duration of the project.

Finally, the project-based DEMs were used as reference maps to help locally identify the centerline of the river and bank lines.

4.2.5.1. Project-based point cloud processing

The point clouds collected in the current project have resolutions of as high as 2 cm, but they require filtering to eliminate spurious elevations, and translation to ensure that they are aligned with a local CRS. Much of the filtering was done during processing of the UAS imagery. For example, the pre-processing routine found digital terrain points and discarded canopy points. Prior to point cloud alignment, additional outlier points were also filtered from the point clouds by eye.

4.2.5.2. Project-based point cloud alignment

The processed point clouds do not align well with existing DEMs because the absolute position of the base station while collecting point cloud data is not known. To accurately calculate changes in the main channel and floodplains, the point cloud data had to be realigned so that all DEMs from different datasets had the same datum. To do this, the alignment shift for each of the DEMs had to be determined. DEMs that were created in CloudCompare were uploaded into QGIS through the Data Source Manager by adding them as raster files. In QGIS, the elevation profile tool was used to compare parts of the DEMs that were known to be unchanging over the course of the project. The elevation profile tool is found under the View tab in QGIS, and a screenshot of the tool, when opened, is shown in Figure 4.1. A side note of interest is that in Figure 4.1 the change in channel elevation between 2013 and 2020 is about 5 meters, an indication of the vast amount of sediment that was washed downstream when the dam was breached. The elevation profile tool dialog window shows the elevation profile of a selected transect of a DEM. To use the tool, the imported DEMs were selected for creating the elevation plot. Then, the capture curve button was activated from the menu ribbon, and lines were drawn over surfaces that were known to be unchanging, such as roads and buildings. There were four project-based DEMs that needed to be aligned. A transect line was drawn over the island in the middle of the Highway 281 bridge at the Spencer site, and the DEMs were compared. The September 2022 DEM was about a meter higher than the other three DEMs, but the other DEMs were only slightly different from each other in both the horizontal and vertical directions.

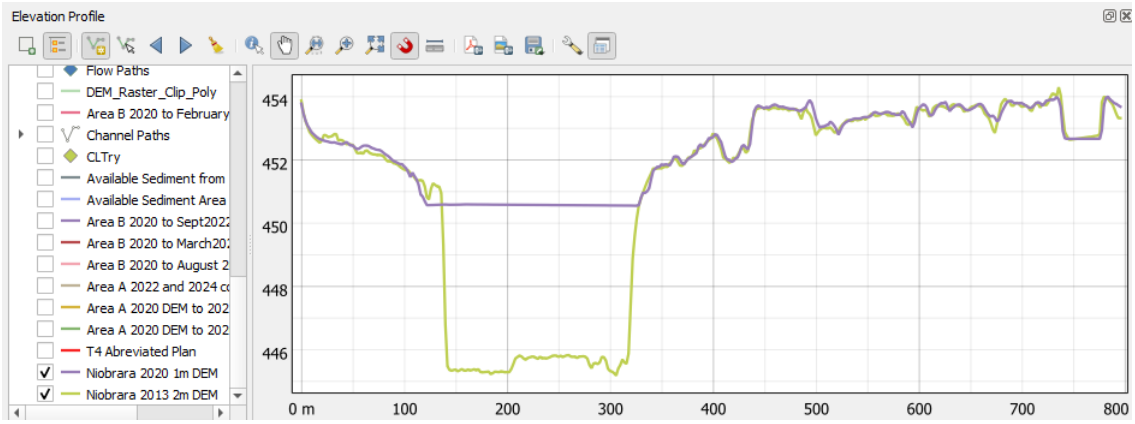

Figure 4.1 Example of the elevation profile tool in QGIS showing 2013 (green) and 2020 (lavender) cross sections of the Niobrara immediately downstream of Highway 281.

The differences in horizontal and vertical positions were resolved by aligning the point clouds prior to recreating the DEMs in CloudCompare. To align point clouds, a reference point cloud and the point cloud to be aligned were selected in CloudCompare before running the process "Align two clouds by picking equivalent point pairs". Then points were identified in the point cloud images that were unchanging in time. These points included points on roads, buildings, parking lots and parts of the dam. Once a minimum of 4 points was chosen for the reference cloud and the cloud to be aligned, the align button was selected and then the OK button was pressed and the point cloud was realigned with the reference point cloud. The August 2023 point cloud was selected as the reference cloud for our data. From the aligned point clouds, DEMs were created and again uploaded into QGIS for comparison of elevation profiles. The aligned profiles were found to be within 20 centimeters of each other.

4.2.5.3. Realignment of project-based point clouds

Ultimately, we wanted to compare UAS data with the DEMs from USGS and NDNR. However, the vertical datums of the datasets were not the same as for our data, nor were our data horizontally aligned with existing DEMs. To align our data to these datasets we worked with the original USGS point cloud, but the USGS dataset was very large. It worked better to use only a few merged tiles from the USGS dataset. The USGS point cloud was collected during the construction of the new bridge over the river. So, to ensure that alignment points were unchanging, points on the road and undamaged sections of the dam were used as alignment points and not points over the bridge or on the island. Aligning the point clouds to the USGS point clouds was tricky because the USGS point clouds had so many points that it was difficult to tell which points to align our point clouds with. The August 2023 point cloud was realigned with the USGS point cloud iteratively with different alignment points to identify the best possible alignment. Then the other point clouds were realigned to the August 2023 point cloud.

4.2.5.4. Creation of DEMs from project-based point clouds

After initial processing and realignment, digital elevation models were created from the point cloud data using CloudCompare. These DEMs were useful for estimating sediment loss and floodplain cross-section data (for raster points that were above the water line). To create the DEMs, obvious outliers of the point cloud were filtered by eye, identifying them by viewing the

point cloud at different angles, selecting them, and using the cut tool. The point cloud was then selected, and under the Tools tab, Projection/Rasterize was chosen. The rasterized window then came up and a step size was chosen, spaced in meters. For our analysis, we selected a spacing of two meters. The active layer of the raster was set to the height grid values. For the projection, the direction was set to Z, and the cell height was set to average. Empty cells were left empty. Then the Export tab was selected, and Raster was pressed. Export heights was the only box checked in the window prior to selecting OK to create the raster. The raster was then saved as a TIFF file, and the DEM was created. The DEM could then be directly uploaded into QGIS as a raster. A profile tool was used to compare our four final DEMs to the USGS DEM at fixed locations. The profiles of all five DEMs were found to be within 20 centimeters of each other at fixed locations.

4.2.5.5. Identification of local river channel plane

To quantify changes in the main channel over time, CloudCompare was used to create a plane that represented the slope and direction of the main flow area of the channel. This plane is needed as a datum to determine the amount of available sediment stored in the floodplain above the active channel. Using the Aerial Imagery in point cloud format (.las file), we created a plane at the level of the active alluvial area – the area above the water surface but below the banks. The active alluvial area is the part of the channel that is covered with ice during the winter. Four methods were attempted to identify the best datum representation of the active flow area from the point cloud data:

- ***Filtered*** - After eliminating points in overbanks, floodplains, and obvious water flow areas, a plane was fitted to the remaining pre-filtered points
- ***Selective*** - Additional banks were eliminated and a plane was fitted only to points within the river. For any areas that were obviously above the water surface (islands) the points were eliminated. The remaining points were points adjacent to the water surface. These data are more selective than the filtered data.
- ***Manual*** - Points that were representative of the upstream and downstream reaches of the river were manually selected and a plane was fit to them.
- ***High-Res*** - A plane was fitted to the unfiltered, high-resolution point cloud after the overbanks, obvious water flow, and floodplains were eliminated. The high-resolution point clouds were tiled and the files had to be merged to fit the plane to all the tiles.

The parameters provided by CloudCompare that describe the fitted plane are the *dip* and *dip direction*. The dip is the angle of the plane relative to the horizontal in the direction of the maximum gradient. Dip direction, also known as the strike, is the angle measured from north (azimuth) to the direction of the maximum gradient. The September 2022 point cloud was used to create the base plane because it was the first dataset that was collected.

The *dips* found using the ***Filtered*** and ***High-Res*** data were about the same (0.0949° and 0.1028°, respectively), but the *dip direction* was smaller for the ***Filtered*** data (76.8888°) than for the ***High-Res*** data (95.6705°). The *dip* for the ***Selective*** data was 0.2798°, and the *dip direction* was 153.8924°. The *dip* for the ***Manual*** data was 2.4765°, and the *dip direction* was 171.9762°. Based on observation of aerial photos of the test site, the slope of the floodplain is in a general

direction between 75 and 105 degrees. Neither the ***Selected*** nor the ***Manual*** approach produced results that were acceptable. For the final river channel plane, we selected the result of the ***High-Res*** approach because the *dip direction* of the ***High-Res*** plane was closest to the observed dip direction of the Niobrara River.

4.2.6. Hand collected GPS data

GPS elevation data were collected by hand to obtain a better interpretation of the river bathymetry so that flow modeling would be more accurate. The data were intended to provide accurate cross-section shape information and to be used in conjunction with point cloud data to better understand local river morphology.

4.2.6.1. Data collection

On August 29, 2023, bathymetry data were collected using a hand-held GPS in the Niobrara River floodplain at Highway 11. Data collection began upstream near a chute where the water was too swift to cross. Many points were collected, containing several complete cross sections, but the river was too swift and deep in most locations to cross all the way from bank to bank. Although we could only collect a few cross-sections, we were able to collect many water surface elevations and riverbed elevations. In most locations, the water depth ranged from 0 ft to 4 ft. Some locations were deeper, and we could not collect data in those locations.

On August 30, 2023, additional GPS bathymetry data were collected at Highway 281. The Niobrara River at Highway 281 was shallower than at Highway 11 and the terrain was not as rough. Learning from the previous day at Highway 11, we were able to collect a larger data set. Data were collected from well upstream of the dam, near where a chute enters the lower reservoir. At Highway 281, we collected more complete cross-sections along with water surface elevations and a few partial cross-sections in locations where the water was too swift to cross completely.

The GPS data collected from Highway 11 and Highway 281 were corrected using Post-Processed Kinematic corrections. The corrections were obtained using a fixed base station. Once corrected, the data were entered in Excel with columns of longitude, latitude, elevation, x, y, distance, and depth. The longitude, latitude, and elevations were directly from the hand-collected data. The x and y points were calculated in QGIS based on the longitude and latitude and using a local Coordinate Reference System (CRS) for Northeast Nebraska. The eastings and northings that x and y represent could then be used to calculate distances, areas, and volumes. For cross-section distances and longitudinal distances between GPS points, distances were calculated using the x and y points and a distance equation,

$$Distance = \sqrt{(x_2 - x_1)^2 + (y_2 - y_1)^2}$$

For cross-sections, depths were found by subtracting measured elevations from the local water surface elevation of the cross-section. The local water surface elevations were determined by measuring the water surfaces on the banks of the cross sections. Once the columns were complete, scatterplots were created using the distance and the elevation points. Cross-sections are displayed in Chapter 6 with distance on the x-axis and the elevation on the y-axis.

4.2.6.2. Alignment of PPK GPS data

The hand-collected PPK GPS data were aligned to the August 2023 Point Cloud since the coordinates of the base station used for the GPS data were also arbitrary. The PPK GPS data were imported into QGIS and then exported as a shapefile using the EPSG:26914 NAD83/UTM Zone 14N CRS. The new shapefile was imported into CloudCompare without any Global shift or scale. The new points were displayed under the August 2023 ortho point cloud, which was already open in CloudCompare. The GPS points were then aligned in the same way as described for the point clouds. The only issue was that the GPS points were not spaced similarly to the point clouds. So, selecting points that exactly matched up was difficult. But to ensure that the GPS points and the point clouds were aligned, bridge points to be aligned were selected and then the *Fine Registration* button under *Tools/Registration* was chosen. Using the point picking tool, GPS alignment points and the August ortho point cloud were compared. Once the GPS points were aligned properly, the *Points Registered File* button was selected and the data were saved as a ascii/csv file with a **.csv** extension. The csv file was then reimported into QGIS to make sure that the GPS points were properly aligned.

4.3. Site Visit Overview

4.3.1. September 2022 site visit

Table 4.2 contains what data was collected at Highways 11 and 281 and how the data were collected. In the September 2022 site visit, the only data that were collected were the aerial survey, one cross-section profile just downstream of Highway 281 bridge and many pictures.

Table 4.2 Summary of September 2022 data collection

Data Collected	How Data were Collected
Aerial Surveys	UAS (Unmanned Aerial System)
Cross-section Profile at Bridge Crossing	Profiler (PPK)
Photos	Mobile Device

Figure 4.2 shows the orthomosaic collected at Highway 11 in September 2022. There is banding in the orthomosaic. One possible reason for the banding is the cloud cover. The weather was partly cloudy, the images under the clouds come out differently than images taken in full sun. Another possibility was the time of day. Since this aerial was taken at the beginning of September, the sun was beginning to set earlier. The images can change brightness as the time of day changes. The flow rate range during data collection was between 1184 and 1342 cubic feet per second. This flow rate range is slightly below average. The bed forms under the water surface are very clear in the aerial imagery. There is a lot of sediment in the active flow area.

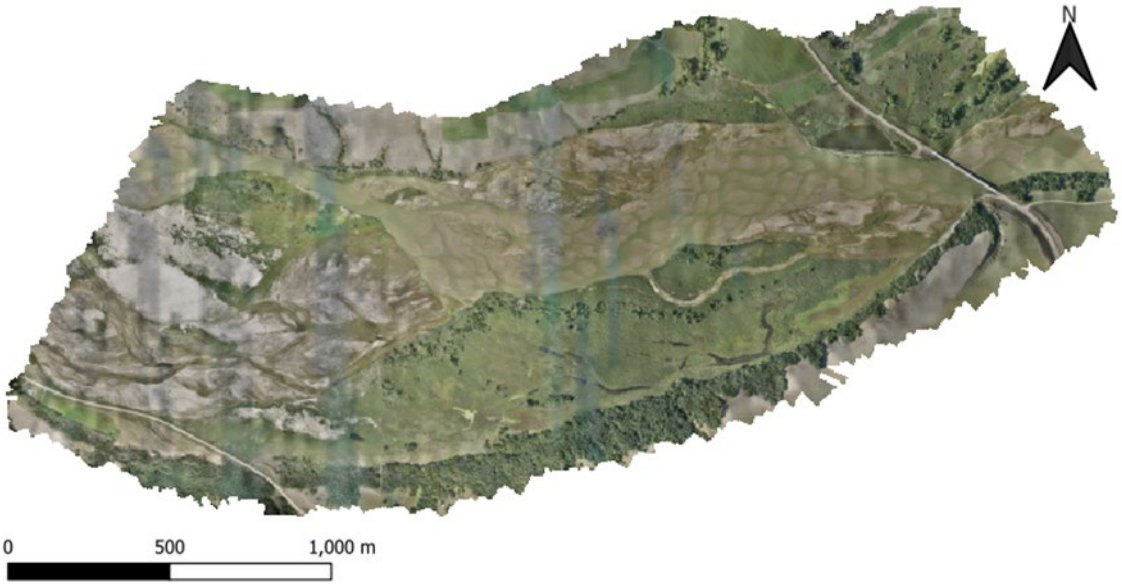

Figure 4.2 September 2022 orthomosaic at Highway 11

Figure 4.3 shows the orthomosaic that was collected at Highway 281 in September of 2022. This orthomosaic does not have as much banding as Figure 4.2 but the aerial was collected earlier in the day, where the time of day does not have as much effect. The flow rate range was considered similar to the Highway 11 flow rate range though the stream gage was stationed at Highway 11. In this aerial image, like Highway 11, there is a lot of sediment in the active flow area and the main channel is clearly defined as well as bedforms.

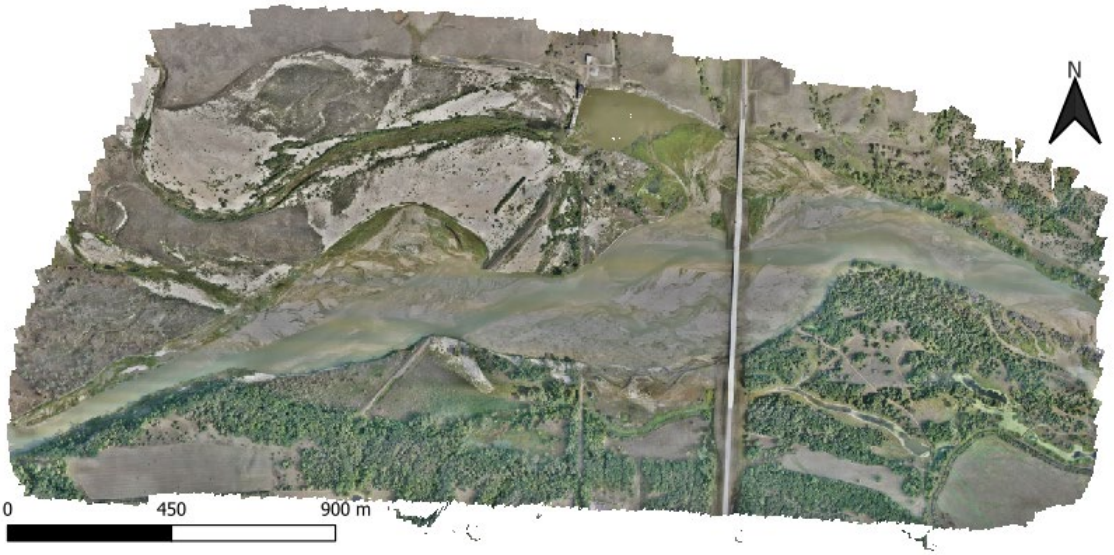

Figure 4.3 September 2022 orthomosaic at Highway 281

4.3.2.March 2023 site visit

Table 4.3 describes data and how it was collected during the March 2023 site visit. The difference between the March 2023 site visit and the September 2022 site visit is that the cross-

section at the bridge was not collected due to high flow rates, floating ice, and high stage across the channel. However, images were collected from a timelapse camera to show any changes happening during the high flows and ice break up. The timelapse camera captured images where the bank was clearly eroding and the main channel was changing lateral position.

Table 4.3 Summary of March 2023 data collection

Data Collected	How Data were Collected
Aerial Surveys	UAS (Unmanned Aerial System)
Photos	Timelapse Camera and Mobile Phone

Figure 4.4 shows the orthomosaic collected at Highway 11 in March 2023. In this aerial image, the main channel is clearly defined and there are large areas of anchor ice, where ice is stationary over the riverbed. These areas are mostly where there are large banks of deposited sediment. Looking back at Figure 4.2, there was not a clearly defined main channel, but there were a lot of defined dunes across the channel, which in Figure 4.4 were completely covered in ice. Some floating ice chunks were darker than the stationary ice, suggesting that the floating ice was carrying sediment downstream. The discharge range during the site visit day was between 2500 and 3365 cubic feet per second. The are temperature was as high as 38 degrees Fahrenheit and as low as 22 degrees Fahrenheit and it was cloudy in the morning but cleared up later in the day.

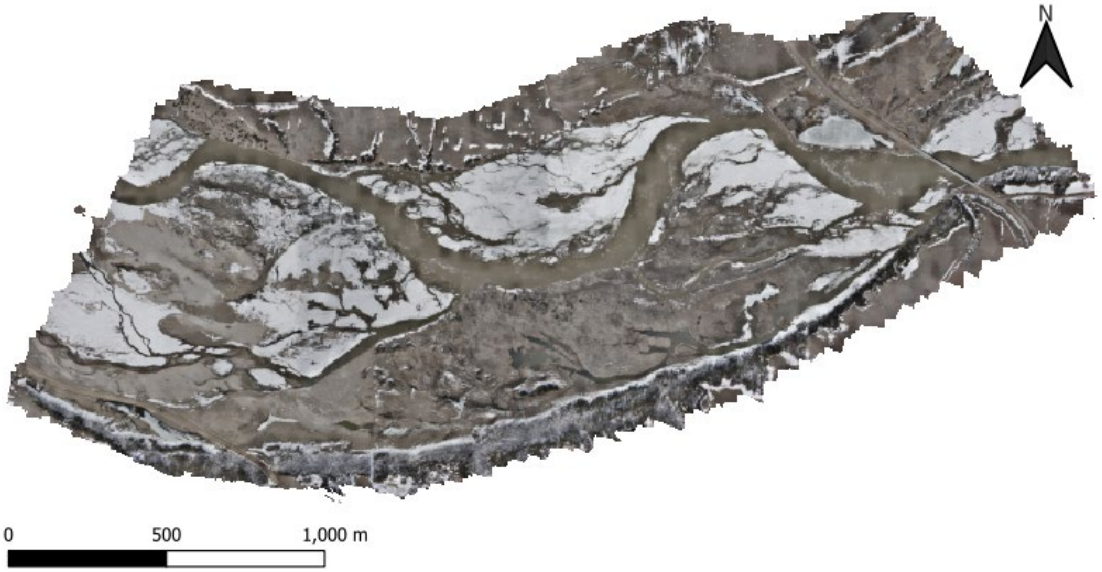

Figure 4.4 March 2023 orthomosaic at Highway 11

Figure 4.5 shows the orthomosaic that was collected at Highway 281 in March 2023. Like the aerial image at Highway 11, there is a clearly defined channel and ice formation over the shallow bedforms. But in this aerial image, there were some areas where there was a buildup of floating ice. Comparing this aerial image with Figure 4.3, there is some erosion between the dam and the bridge on the left-descending bank. Observing the area of erosion, there was rip rap placed around the electrical poles to prevent the bank from eroding. The stage during this site visit was so high that the water surface was close to touching the bottom of the bridge. The discharge

range was similar to the Highway 11 discharge range and the weather was the same due to collecting the aerials on the same day.

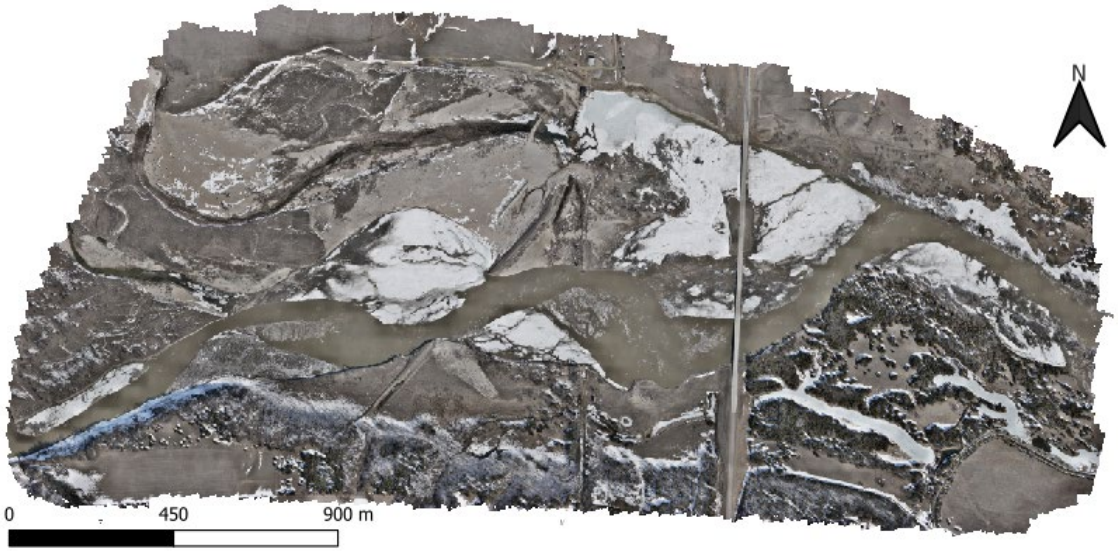

Figure 4.5 March 2023 orthomosaic at Highway 281

4.3.3.August 2023 site visit

Table 4.4 summarizes the data collected and how the data were collected during the site visits in August 2023 for Highway 11 and Highway 281. The main difference between the data collected in the previous two site visits and the data collected in August 2023 is that cross-section profiles and longitudinal profiles were collected using a GPS unit. The cross-sections and longitudinal profiles were manually collected. There were 6 cross-section profiles collected at Highway 11 site and 9 cross-sections collected at Highway 281.

Table 4.4 Summary of August 2023 data collection

Data Collected	How Data were Collected
Aerial Surveys	UAS (Unmanned Aerial System)
Cross-section Profiles along River	Profiler (PPK)
Longitudinal Profile at Highway 281	Profiler (PPK)
Photos	Mobile Device

Figure 4.6 shows the orthomosaic collected at Highway 11 in August 2023. In this aerial imagery, the main channel is still clearly defined from March 2023. There are areas where dunes of sediment protrude above the water surface where there was anchor ice in March, but the thalweg has changed positions. The main differences between September 2022 and August 2023 are the definition of a main channel and the size and number of bedforms. In Figure 4.6, there are fewer but larger bedforms than during September of 2022. There are clear differences between September 2022 and August 2023 but no bank erosion. The discharge range during this site visit was between 1334 and 1452 cubic feet per second. The weather conditions were fair with a high of 92 degrees Fahrenheit and a low of 55 degrees Fahrenheit.

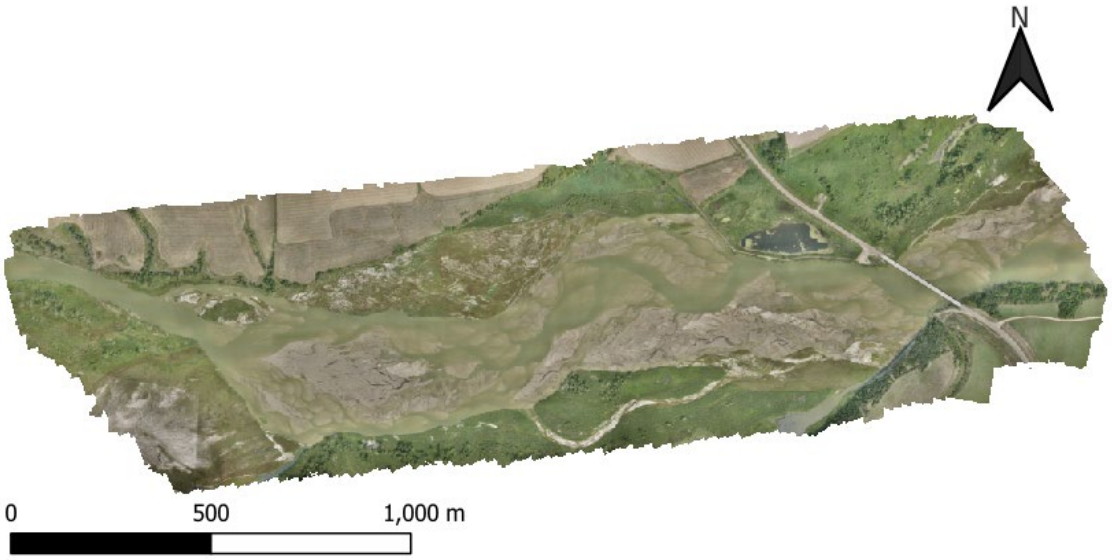

Figure 4.6 August 2023 orthomosaic at Highway 11

Figure 4.7 is the orthomosaic collected at Highway 281 during August 2023. Comparing this aerial image with Figure 4.3, the main channel meanders more and there has been major erosion on the left descending bank between the dam and the bridge. The pool downstream of the old spillway contains more water and more sediment has been transported under the bridge north bridge, but there is no indication that the main channel is moving back to the north bridge. Comparing this aerial image with Figure 4.5, both aerials have the same defined main channel. Where there was anchor ice in Figure 4.5, those areas are filled with sediment in Figure 4.7. Since this aerial was collected the day after Highway 11 the discharge range is different. The discharge range during this site visit was between 1397 and 1543 cubic feet per second. The weather conditions were fair with a high of 89 degrees Fahrenheit and a low of 52 degrees Fahrenheit.

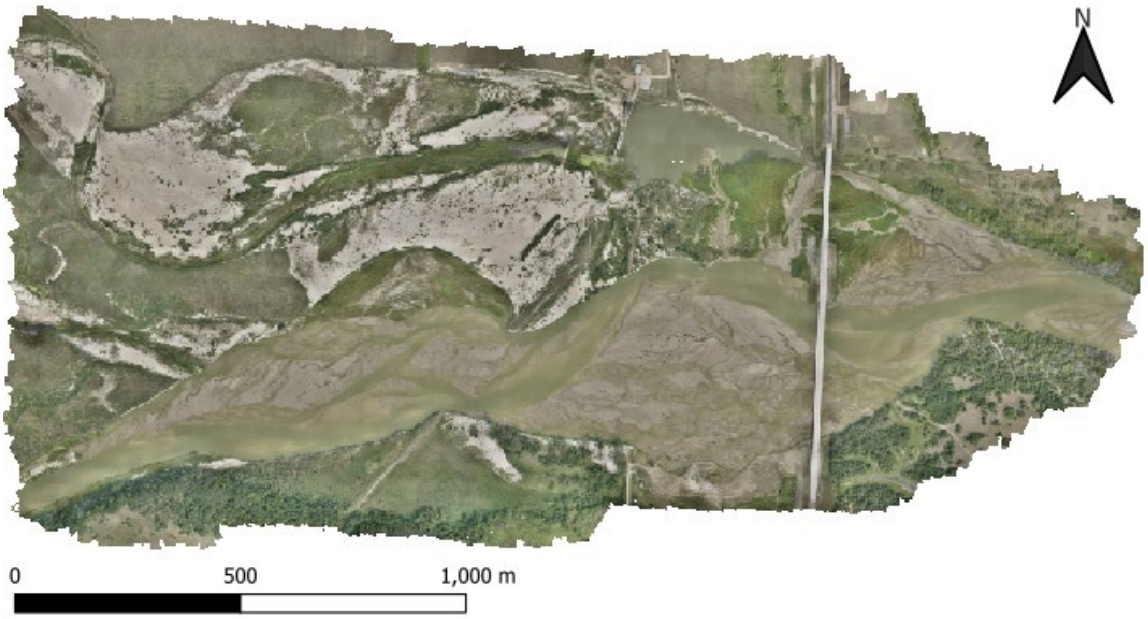

Figure 4.7 August 2023 orthomosaic at Highway 281

4.3.4. February 2024 site visit

Table 4.5 lists the data collected during the last site visit in February of 2024. Figure 4.8 shows the orthomosaic collected at Highway 11 in February 2024. In this aerial the water is turbid and the stage is high. This indicates that there is a lot of suspended sediment transport. Although there was more ice in Figure 4.4, the water was moving quickly. The discharge range during February 2024 was between 1820 and 3450 cubic feet per second. There was a large variation in the discharge range. Another difference between February 2024 and March 2023 was that the ice in 2024 appeared dirtier, which means that either the 2023 ice was thicker or that the 2024 ice was carrying more sediment. The weather conditions were fair with a high temperature of 62 degrees Fahrenheit and a low temperature of 26 degrees Fahrenheit.

Table 4.5 Summary of February 2024 data collection

Data Collected	How Data were Collected
Aerial Surveys	UAS (Unmanned Aerial System)
Photos	Timelapse Camera and Mobile Phone

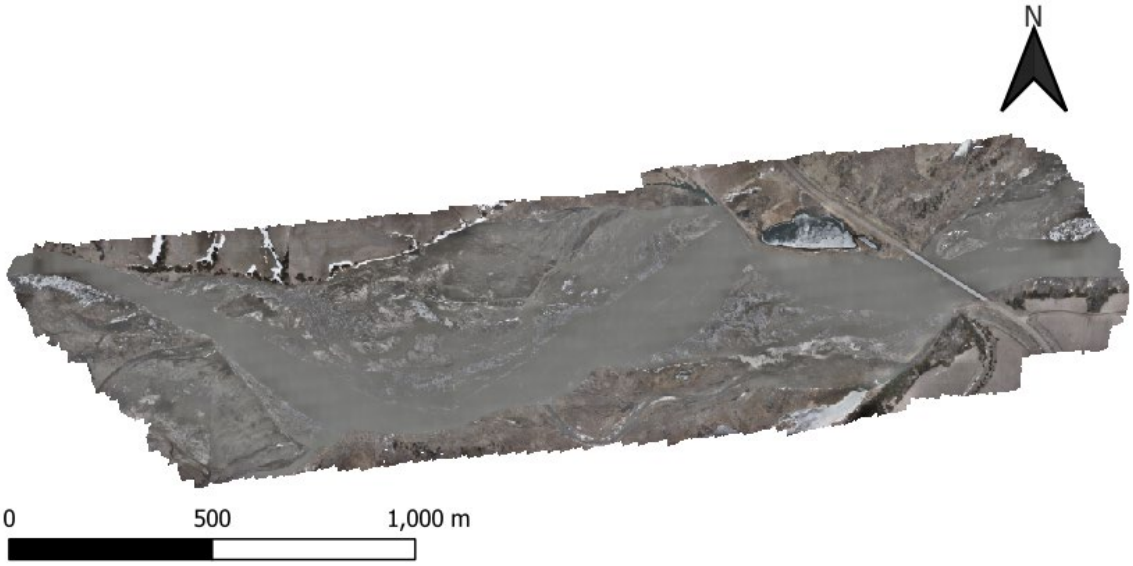

Figure 4.8 February 2024 orthomosaic at Highway 11

Figure 4.9 is the orthomosaic that was collected in February of 2024. This aerial shows a straighter channel path than in Figure 4.5. Like Figure 4.8, the stage was greater, there was not as much ice cover, and the water was more turbid. Some changes between March 2023 and February 2024 that can be seen in this aerial image are the channel path, the width of the river, and the amount of erosion that occurred. In this image there was erosion happening in multiple spots. One was upstream on the lower left side of the image, where the channel makes a hard-left turn before entering a chute, another was between the dam and the bridge on the left descending bank, and the last spot was just downstream of the bridge where the channel used to flow when the dam was functional. The flow range is similar to the Highway 11 discharge range of 1820 to 3450 cubic feet per second. The weather was also similar to the Highway 11 site visit weather.

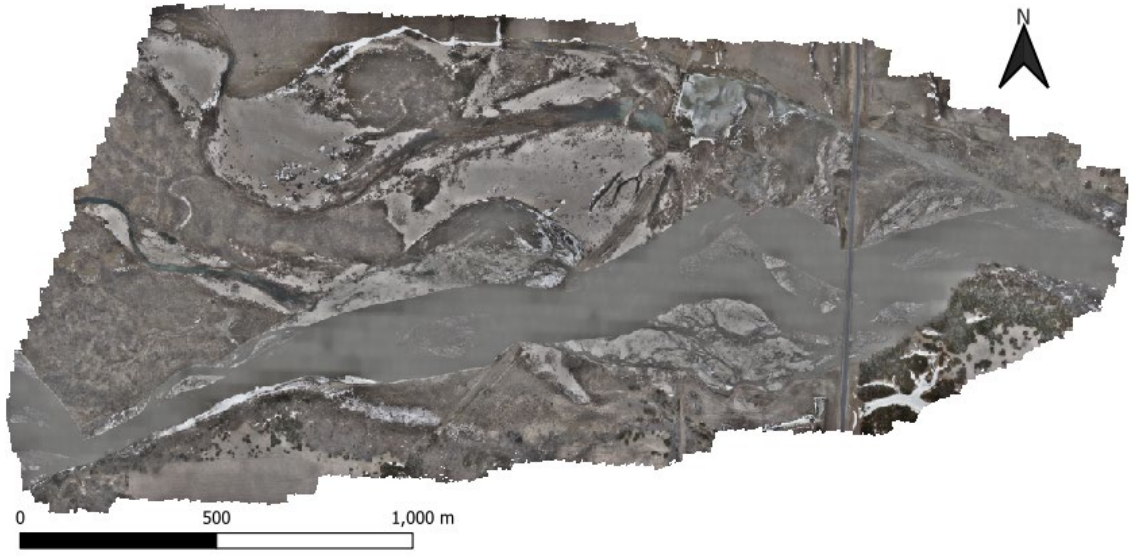

Figure 4.9 February 2024 orthomosaic at Highway 281

5. Sediment Budget Calculations and Measurements

5.1. Introduction

For accurate understanding of sediment transport at the study site, a thorough analysis of the volume of sediment that is readily available for transport and the amounts that have already been eroded is needed. In this chapter, quantities of readily available sediment will be identified and reported. In addition, using time-lapse aerial images of the site, point cloud elevation data, and digital elevation models (DEMs), areas of sediment that have been eroded over the course of the project will be identified and volumes of sediment lost to erosion will be quantified. This information is valuable as an input for the sediment model and for validation of model performance.

5.2. Longitudinal Elevation Profile of Niobrara River

A longitudinal elevation profile of the river was created using equally spaced cross sections that were found for the Niobrara floodplain using a script that did the following:

a. A rough centerline was sketched from upstream of Highway 11 to downstream of 503rd Avenue.
b. Initial positions of cross sections were determined by starting on the downstream end of the rough centerline and working upstream at a specified interval. For the current work the cross section spacing was 200 meters.
c. The cross sections were placed by finding a line orthogonal to the rough centerline points. The cross sections were made to be much wider than the floodplain.
d. The minimum elevation was found for each cross-section by sampling the 2020 DEM at the resolution of the raster.
e. The edges of the floodplain were determined by finding where the elevations of each cross-section exceed a specified height above the minimum cross-section elevation. For this study, the threshold height was 7 meters. The cross sections were trimmed at these locations on both the right and left bank.
f. Center points of the trimmed cross sections were identified.
g. Filters eliminated some of the cross sections. If the width of a cross-section was too small, the cross-section was discarded. If the cross-section width was not similar to the widths of the cross-sections upstream and downstream, it was discarded. The filters were necessary because of features like the dam, roads, and mouths of streams.
h. A spline was fit to the remaining center points to get an optimized centerline. The routine was then rerun using the optimized centerline in place of the rough centerline.
i. Additional cross-sections were interpolated between the cross-sections determined by the optimization routine. Interpolation was necessary in locations with sharp corners so that cross sections would not overlap. Interpolation also was used to replace cross-sections that were lost when filtering. Interpolated cross sections had a spacing of 50 meters.

The result is a set of evenly spaced cross sections that are defined by the edges of the active floodplain – not by the currently active channel. Figure 5.1 shows a close-up of cross sections with 50-m spacing near a bend in the channel to demonstrate what the final cross sections look like.

Figure 5.1 closeup of cross sections

Figure 5.2 shows the cross sections for the entire reach between Highway 11 to 503rd Avenue, which is about 40 km.

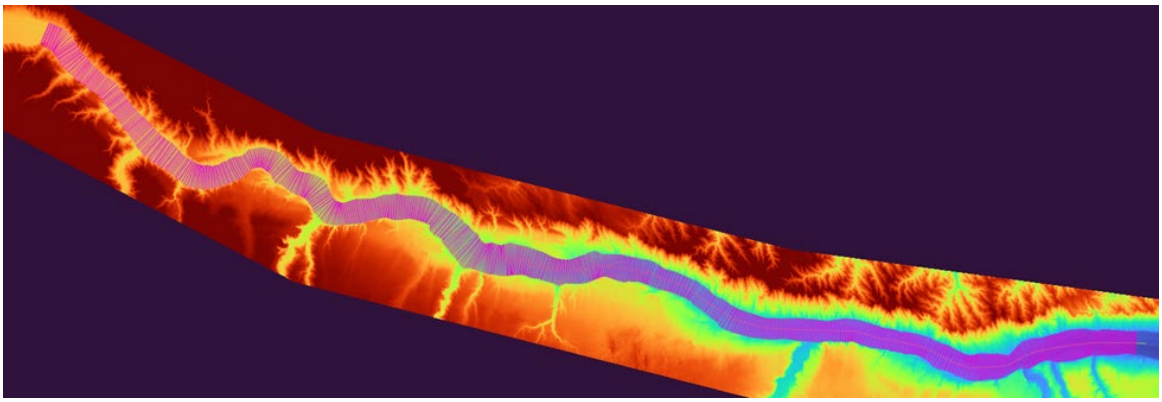

Figure 5.2 Cross sections spaced at 50-m intervals for the entire reach from Highway 11 to 503rd Avenue.

Once the cross sections were found, minimum elevations were found for each cross section using another subroutine. The minimum elevations were found using DEMs from both 2013 and 2020. The results shown in Figure 5.3.

The following assumptions were made to create Figure 5.3:

a. Minimum elevations were the elevations of the water surfaces (not the bed). The minimum bed elevations are unknown. It was assumed that water surface elevations provide a good estimate of the channel slope over these long distances. It is known that in the reservoir, the water depth was not much greater than the bed elevation.

b. The seven-meter bluff elevation was arbitrary and was intended to find a reasonable place to terminate cross sections. It does not identify the actual floodplain but goes slightly beyond what was identified as the floodplain from aerial imagery. The lengths of the cross sections do not play a role in the determination of water surface elevation or sediment deposit estimations.
c. The optimized centerline is the centerline of the floodplain, not the centerline of the active flow channel. There are purposes for both of these, but for the longitudinal profile and sediment availability estimates it makes sense to use the floodplain centerline because the active channel centerline is much more complex and as the flow changes, the length of the active channel changes. For high flows, the length of the active channel becomes similar to the length of the channel defined by the floodplain.
d. Figure 5.3 only considers the elevation of the main channel and not the off-channel storage of sediment. There is a lot of sediment stored off-channel upstream of the dam. This will become a part of the active river over time (quickly in some conditions).

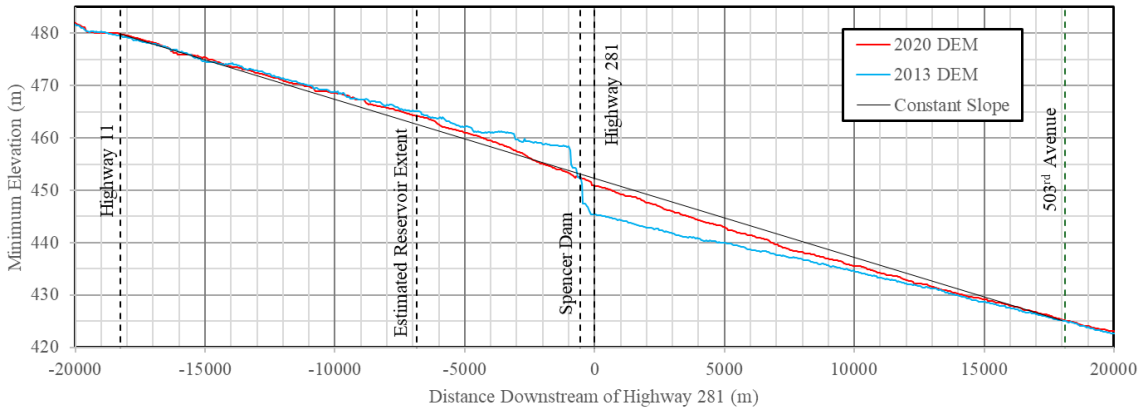

Figure 5.3 Comparison of minimum elevations as a function of distance downstream of the Highway 281 Bridge

Figure 5.3 is a one-dimensional longitudinal profile of the Niobrara River from Highway 11 to 503rd Avenue (Redbird Creek). The red line is the elevation of the water surface from the 2020 USGS DEM, and the light blue line is the elevation from the 2013 Holt and Boyd County DEMs from the Nebraska Department of Natural Resources. The dark line is a straight line that was created to show the expected change in elevation upstream and downstream of the inflection point, which is at Spencer Dam. Figure 5.3 also shows the locations of the bridges along the reach, Spencer Dam, and an estimated location of the extent of the reservoir.

The width of the active alluvial channel from Highway 11 to 503rd Avenue is relatively uniform, and there are no major tributaries between the two endpoints. So it might be reasonable to assume that the final equilibrium slope and elevation of the river will be similar to the constant slope line, though this is somewhat oversimplified. This is a one-dimensional perspective, one that does not clearly portray the amount of sediment stored in what was once the reservoir of the dam. Much of this sediment will eventually make its way downstream, evening out the longitudinal profile and causing the bed elevation to continue to rise downstream of the dam for some time. The amount of available sediment is discussed in more detail later in this report.

Additional data collected during the study were used to provide more information about changes in the bed profile that occurred over the course of the project near the Highway 281 bridge. Figure 5.3 was extended to include point cloud information collected during the summers of 2022 and 2023. This was done using a QGIS plugin called *Profile Tool* that plots elevation profiles of polylines that traverse a specified DEM. Adjustments were made to the profile tool that allowed us to record the positions of river banks, identify elevations of all points between selected banks, and save the elevations and bank locations of the profiles in a table. The *Profile Tool* was applied to a set of channel cross-sections from the upstream end of our UAS study area to the downstream end. Cross sections were manually entered at 50-meter intervals as polylines in a shapefile. Banks and profiles were identified for each cross-section. Then the bank coordinates and profile elevations of all of the cross sections in the shapefile were copied and pasted into Excel. For each cross-section in the shapefile, the spreadsheet had a column with cross-section numbers, profile points (each point in the profile had distance from the start of the cross-section, longitude, latitude, and elevation), and bank locations. Points that were outside of the banks or had elevations that were erroneous could be removed from each profile in the spreadsheet. The remaining elevations between the banks were averaged for each cross-section to get an average bed elevation for the cross-section. The cross-section number, average elevation of the cross-section, and active channel width were saved. Then using the measurement tool in QGIS, distances between cross-sections were measured. These were saved with cross-section information in the spreadsheet.

Scatterplots of average cross-section elevation versus the longitudinal cross-section location were constructed, showing the profile of the bank-to-bank alluvial bed of the river from upstream to downstream in Figure 5.4. The process was repeated for the 2013 NDNR DEM, the 2020 USGS DEM, September 2022 elevation data, and August 2023 elevation data. The August 2023 dataset has slightly fewer cross-sections than the others because the size of the surveyed area was smaller. Note that the elevations produced from the NDNR and USGS DEMs represent hydro-flattened elevations, whereas the elevations from the orthophotos represent elevations of the average active alluvial area (below permanent banks). We expect that these two elevations are roughly the same, but do have some computational differences.

Figure 5.4 shows the elevation of the active main channel at Highway 281 starting from the upstream edge of the September 2022 orthomosaic. The location of Spencer Dam and Highway 281 are shown on the chart to show changes upstream of the dam, downstream of the dam, and downstream of the bridge. There is a major jump from the pre-dam data to the current data both upstream and downstream of the Spencer Dam, which was to be expected. The bed elevation did not rise as much between 2022 and 2023 as it did between 2019 and 2022. However, it is difficult to predict how the bed will adjust in the future because changes are strongly dependent on flow.

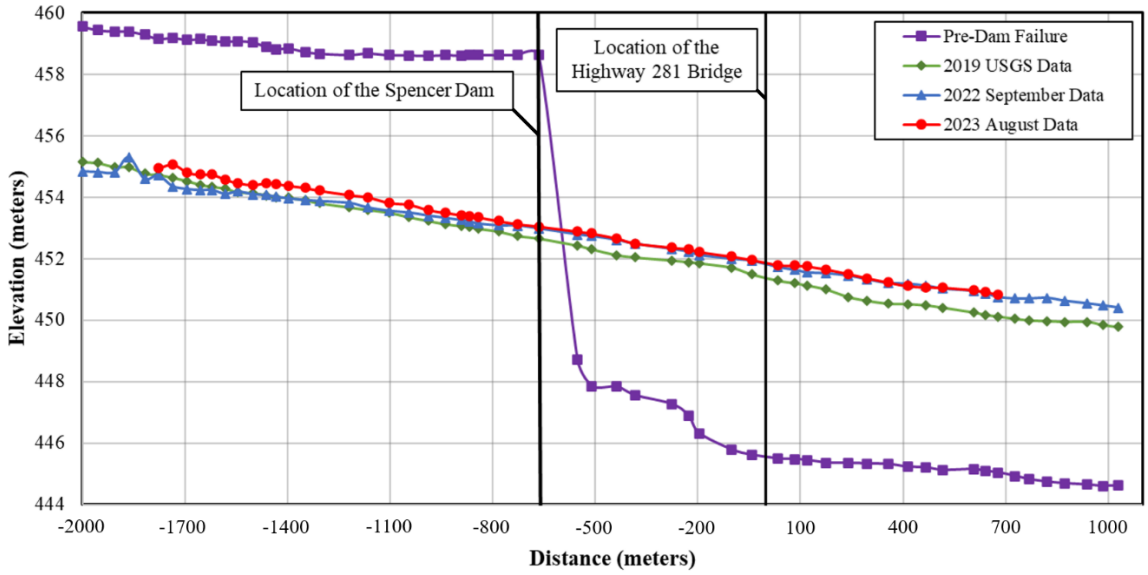

Figure 5.4 Longitudinal profiles of water surface at Highway 281

Figure 5.5 shows the same longitudinal profile of the active main channel as in Figure 5.4 but without the pre-dam failure data so that the y-axis can show more detail. The 2020 USGS data shows a nearly uniform slope until the dam, and there is a deposit of sediment slightly upstream of the bridge. Downstream of the bridge, the elevation drops more rapidly. The September 2022 data appears to have an erroneous point at the upstream end, this could be because the data are near the edges of the orthomosaic. The profile starts a little below the 2020 USGS profile and then rises above the 2020 USGS profile upstream of the dam. The slope of the 2022 profile is consistent between the dam and the bridge. Downstream of the bridge, the river continues at the same slope. The August 2023 profile is more consistent than the 2022 profile.

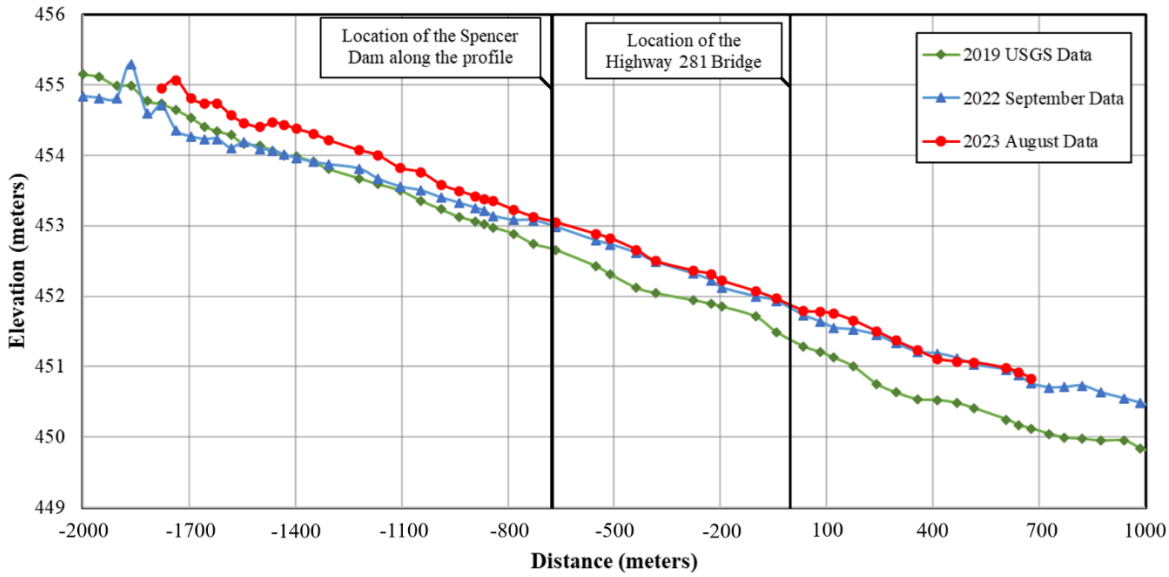

Figure 5.5 Longitudinal profile of water surface at Highway 281 (enlarged)

The elevations for the 2023 profile start and end above the 2020 profile. This could mean that the sediment from the reservoir is filling in the channel and evening out the channel bed more. The 2023 profile starts above the 2022 profile and finishes around the same elevation as the 2022 profile. The slope of the 2023 profile is steeper than that of the 2022 profile and is similar to the slope of the 2020 profile. In all cases, the bed continues to rise, though the rate of aggradation appears to be lessening. With vast amounts of sediment still in storage upstream of the dam, increases in flow rate could lead to increased aggradation rates in future years.

5.3. Sediment Volume Calculation Methods

Two methods were applied to estimate available and eroded amounts of sediment prior to and during the project. The first method was based on the point cloud data collected with the UAS and the local river channel plane. The second was based on uniformly spaced USGS DEMs. Both methods required good assessment of changes that have happened at the study site since 2019, so we relied on DEMs, aerial photographs, and orthomosaics to assess these changes. There were three areas that were examined during the project: two areas upstream of the dam that were called Areas A and B, and an area between the dam and Highway 281 called Area C. These areas are identified in Figure 5.6. Areas A through C have large deposits of sediment, and all have rapidly receding banks. Due to the range of the UAS, Areas A and B were primarily examined using aerial imagery and DEMs from USGS, NDNR, and NAIP. Area C, on the other hand, was examined using preexisting information and information collected during the project.

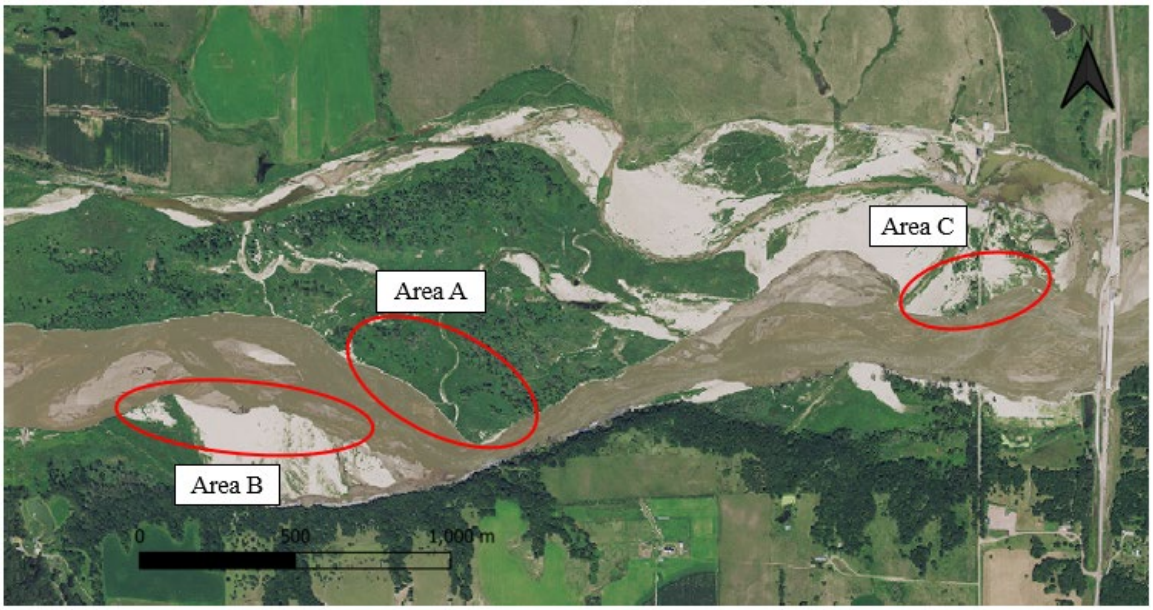

Figure 5.6 Plan view of the study site showing Areas A through C

Flow charts are provided in Figure 5.7 showing the two methods used to assess sediment volumes. In the first method, we used the aligned project DEMs and the local river channel plane to determine how much sediment had been eroded from Area C. To do this, available aerial imagery, including aerial photographs and orthomosaics were opened in QGIS.

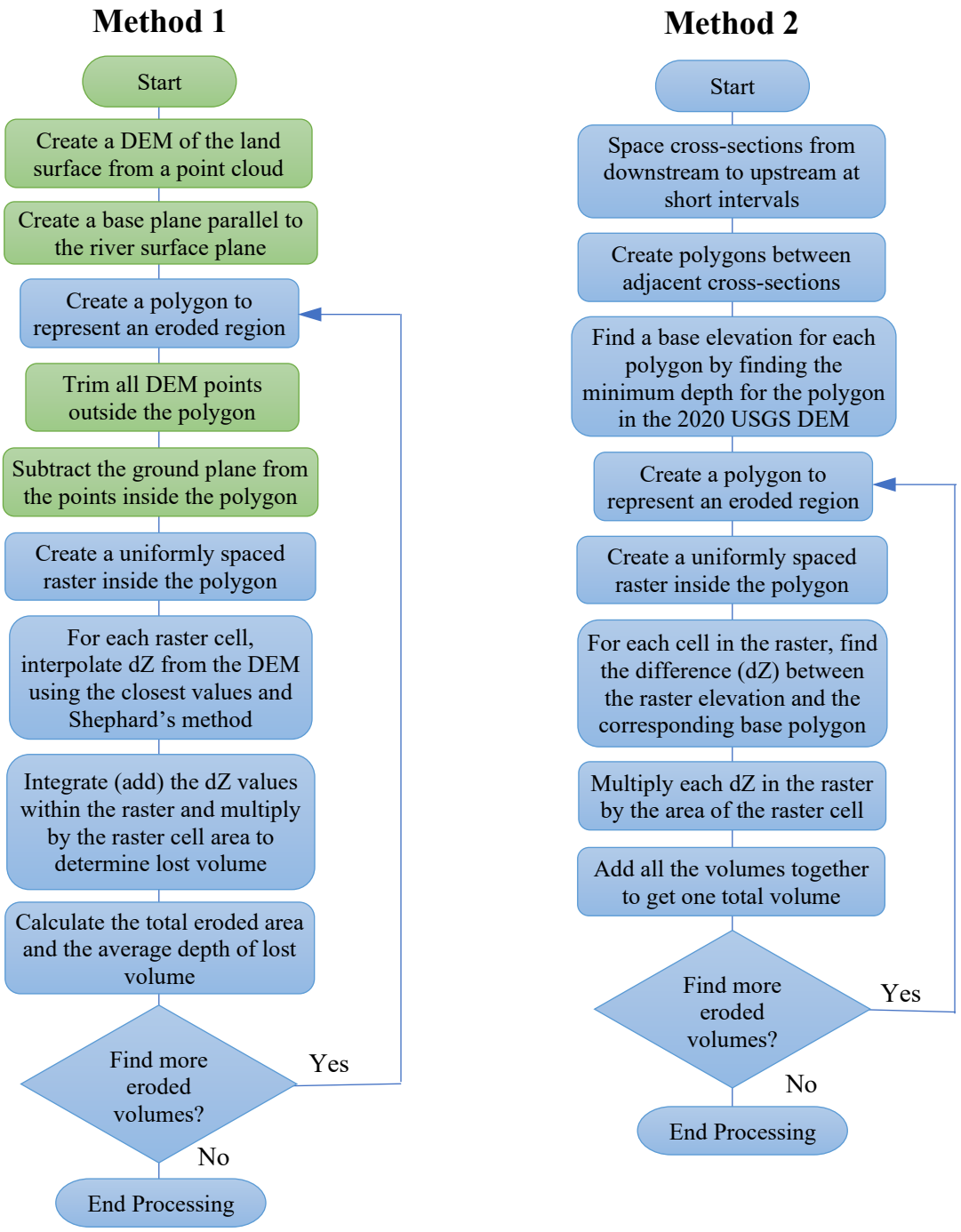

Figure 5.7 Flowchart of methods for finding available and eroded area volumes: Method 1 is for point cloud data and Method 2 is for uniformly spaced DEM rasters. Green cells were done in CloudCompare and Blue cells were done in QGIS.

Polylines representing the left descending bank (LDB) of the river between the dam and the road and adjacent to Area C were identified for each available image of the site and traced by hand in QGIS. Four polylines were drawn representing the LDB for September 2022, March 2023,

August 2023, and February 2024. In QGIS, a plug-in called *Join Multiple Lines* was used to merge pairs of LDB polylines into one polyline to form a polygon. The polygons formed from the riverbanks of two study dates could then be used in combination with a DEM to estimate areas and volumes of sediment eroded by the river during the period between the two field visits. The process and scripts used to identify eroded area polygons are then:

- Identify the positions of the LDBs of the main flow channel using aerial images or orthomosaics collected on two different dates.
- Draw polylines at the positions of the LDBs in QGIS for both dates
- Combine the two polylines into one vector file using the *Merge Vector Layers* tool, which is found in the *Vector/Data Management* menu of QGIS
- Select the vector file layer in the *Layers Panel*, select the two polylines, and select the *Join Multiple Lines* plugin.
- Save the layer edits as a single polyline.

For area C, three polygons surrounding eroded areas (September 2022 to March 2023, September 2022 to August 2023, and September 2022 to February 2024) were created. These new polylines were imported into CloudCompare as a shapefile. The aligned August 2023 DEM was highlighted in CloudCompare, and the *Segment* tool was clicked. There was a narrow box in the upper left corner of the screen and a button that showed intercepting lines. A down arrow next to the button was selected, the option *Use the existing polyline* was chosen, and one of the new polylines was used. The selected polyline turned green, and the box with the red pentagon was selected, followed by the green checkmark. This process allowed us to select only cloud points within the eroded area.

To create a DEM that represented the eroded volume of sediment, the local river channel plane found earlier was subtracted from the high-resolution point cloud that gives land elevations prior to erosion. Differences were calculated between all point clouds and the September 2022 local river channel plane. To compute the height differences within each eroded area, the *Compute cloud/primitive distance* button was selected from the tool panel, the points were double-checked to make sure that they represented the elevation difference, and the resulting file was highlighted and saved as an ascii/csv file, making sure that the file extension was **.csv**. This file contained a list of points that were spaced at 2m intervals, each point having x and y location, elevation (z) of the non-eroded land surface at the point, and the difference between the non-eroded land surface and the local river channel plane (dz). Since each 2m x 2m interval had many point cloud points, z and dz for the interval represented average values. While the point data were spaced on a 2m grid, seams between point data from different tiles of point clouds caused the larger collection of points to be irregularly spaced in some locations; this is the reason why interpolation onto a raster was required.

A python script was written in QGIS that read the 2m spaced point file made in CloudCompare into an array. As stated previously, the file contained x, y, z, and dz (the difference in elevation between the new point cloud and the local river channel plane). To calculate the volume of sediment lost, the point data were interpolated onto a regularly spaced raster with the same extent

and resolution as the point data. In this way, we could determine the average depth, planform area, and volume lost of each region of sediment that was eroded away. The difference between the point data and the raster was that the raster cells are evenly spaced and are much easier to integrate than irregularly distributed points. The Python script does the following:

- All raster cells inside the polygon of the eroded area are identified.
- For every raster cell inside the polygon, the five nearest points from the CloudCompare file are identified and used to calculate the average depth of the cell. The average is weighted using Shephard's method with an exponent of 2.
- The depths of all raster cells inside the polygon are summed and divided by the number of cells to get an average depth of the eroded area.
- The summed depths of the raster cells are multiplied by the raster cell area to find the total volume of lost sediment.

A second method for finding eroded and available sediment volumes was based on the 2020 USGS DEM. The second method was necessary because available UAS data did not cover the entire area of interest. Polygons that define eroded and available sediment deposits were identified in the same way as described in the first method. Again, these polygons were found using available aerial photography and orthomosaics. However, the process of finding elevations of deposits of sediment was somewhat different. A script was written to segment the river channel into polygons at 50-meter intervals from Highway 11 to Redbird Creek. To compute the volume of available sediment deposits from the 2020 DEM, local values of the lowest elevations in the 2020 DEM were used as a reference. Thus, the minimum elevation of each segmented polygon was determined from the 2020 DEM. This minimum elevation represented the local base elevation datum from which sediment availability can be determined. The base elevation datum changes along the length of the river. Much like the first method, the polygons were rasterized and each raster cell within the polygon area was filled with the difference between the elevation from the 2020 USGS DEM and the base elevation datum of the polygon that the raster cell fell within.

Method two computes available or eroded volume in the following steps:

1. Cross sections were spaced from downstream to upstream at 50 m intervals for the study reach – a script was written to automatically determine the cross sections and is described in Chapter 5.2.
2. Adjacent cross-sections were used to create quadrilateral polygons.
3. The base elevation of each polygon was found by averaging the minimum depths of the two adjacent cross sections used to create the polygon. The minimum depths were found from the 2020 USGS DEM using a profiling script in QGIS.
4. A raster was constructed containing all of the points within the polygon of interest (whether it contained available sediment or eroded sediment).
5. All of the cells within the polygon of interest were integrated. To get a dz for each cell, the base elevation of the cross-section polygon that the raster cell was in was subtracted from its 2020 DEM elevation.

The method is demonstrated for the available sediment deposits shown by the hatched areas in Figure 5.8, which shows sediment deposits in Areas A (yellow), B (orange), and C (red). These deposits were identified using automated scripts in QGIS and the 2020 USGS DEM.

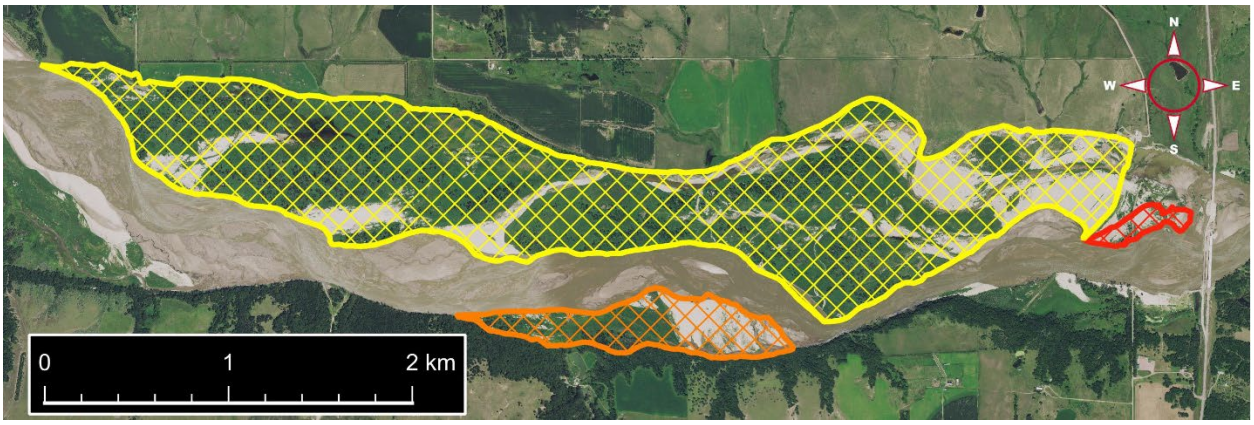

Figure 5.8 Sediment deposits upstream and downstream of the dam based on the 2020 DEM.

Figures 5.1, 5.9, and 5.10 show the process of calculating the available sediment volume from the 2020 USGS DEM. Figure 5.1 shows a closeup of cross-sections at 50-meter intervals around a bend of the river near Highway 11. The centerline is the centerline of the floodplain not the active flow channel. Figure 5.9 is an overview of the cross-section polygons that cover the extent of the reservoir. Each of these polygons has a base minimum elevation; the base elevations decrease along the length of the river in the downstream direction and represent a moving elevation datum. Figure 5.10 shows the resulting map of sediment availability upstream of Spencer Dam in 2020 (yellow and orange) and the sediment that has eroded downstream of the dam since the start of the project (red). In Figure 5.10, the dark blue color represents a 0-meter difference between the 2020 USGS DEM elevations and the base elevations of each polygon and the dark red color represents a 7-meter difference. There is a greater difference between the DEM elevations and base elevation closer to the dam than farther upstream of the dam because sediment deposits are much thicker closer to the dam. Evidence of sediment already eroded from the deposits during the failure of the dam is clearly visible in the Figure 5.10.

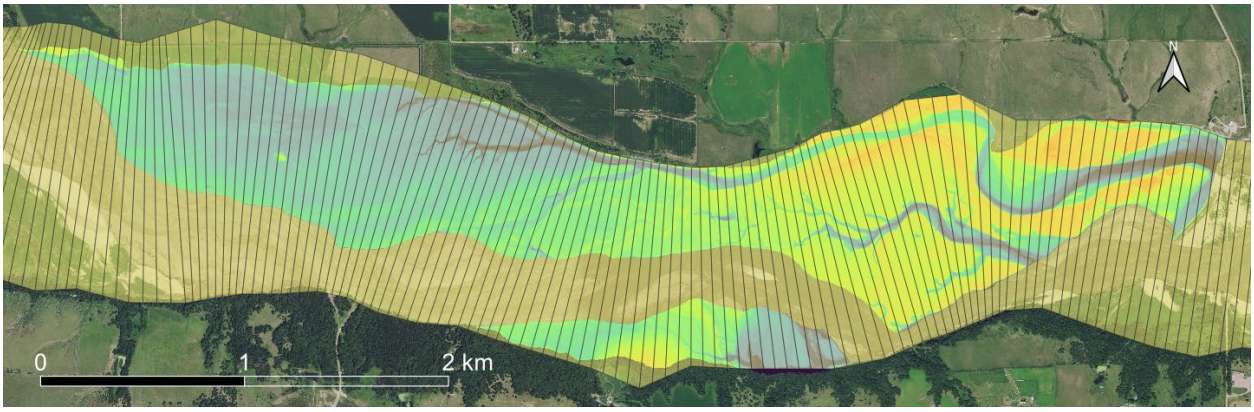

Figure 5.9 Cross section polygons covering the study reach

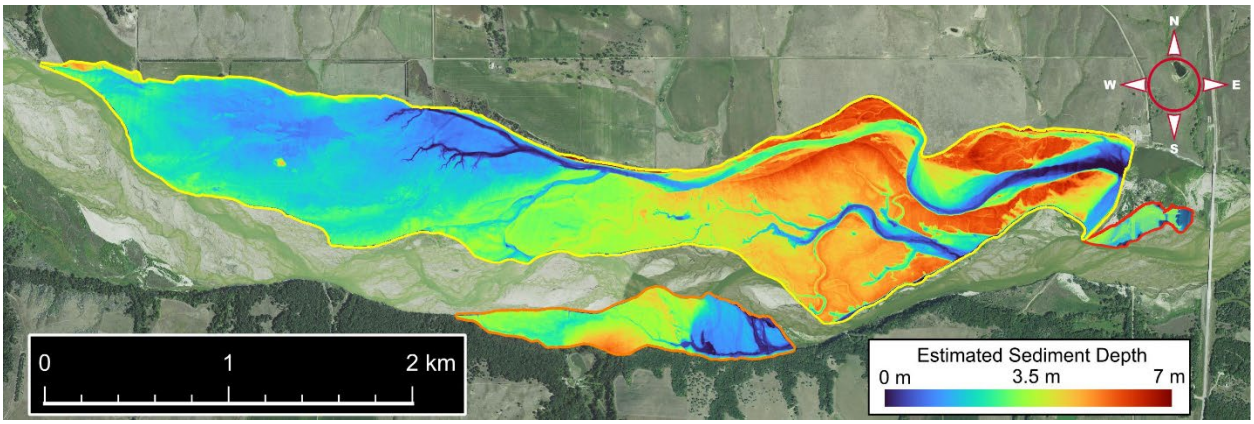

Figure 5.10 Sediment availability in the vicinity of Spencer Dam as determined from the 2020 DEM using a moving datum based on minimum channel centerline elevations

5.4. Sediment Erosion and Availability Volume Results

Aerial imagery and orthomosaics clearly show that there has been major erosion happening at the Spencer site. Calculating available and eroded sediment upstream and downstream of the dam is useful for sediment transport models. USGS DEMs, aerial imagery, and imagery collected between 2022 and 2024 were used to identify banklines and the extent of sediment deposits upstream of the dam. Historical NAIP imagery and DEM data were also used to locate how far upstream the reservoir extended prior to failure. Then, in QGIS, polygons were created to map erosion locations and deposits in the reservoir and downstream of the dam based on NAIP imagery, study imagery and 2020 USGS DEMs, creating polygons for each aerial image that was investigated. Figure 5.8 shows a 2020 aerial of the study site at Highway 281. Three polygons that represent sediment deposits are shown in Figure 5.8. Additional polygons were created that represent eroded material from 2020 to 2024 for three separate locations. The erodible bank areas are found in Areas A (yellow), B (orange), and C (red), shown in Figure 5.8.

5.4.1. Sediment erosion downstream of the dam

Figure 5.11 shows the progression of erosion of the bank line at Area C downstream of the dam. This progression starts with the 2020 USGS DEM, then the September 2022 orthomosaic, then the March 2023 orthomosaic, then the August 2023 orthomosaic, and finally the 2024 orthomosaic. Changes in the bankline from 2020 are shown by the red-hashed areas. The most significant changes are between early spring months and fall months. Erosion begins immediately downstream of the dam and ends just upstream of the bridge.

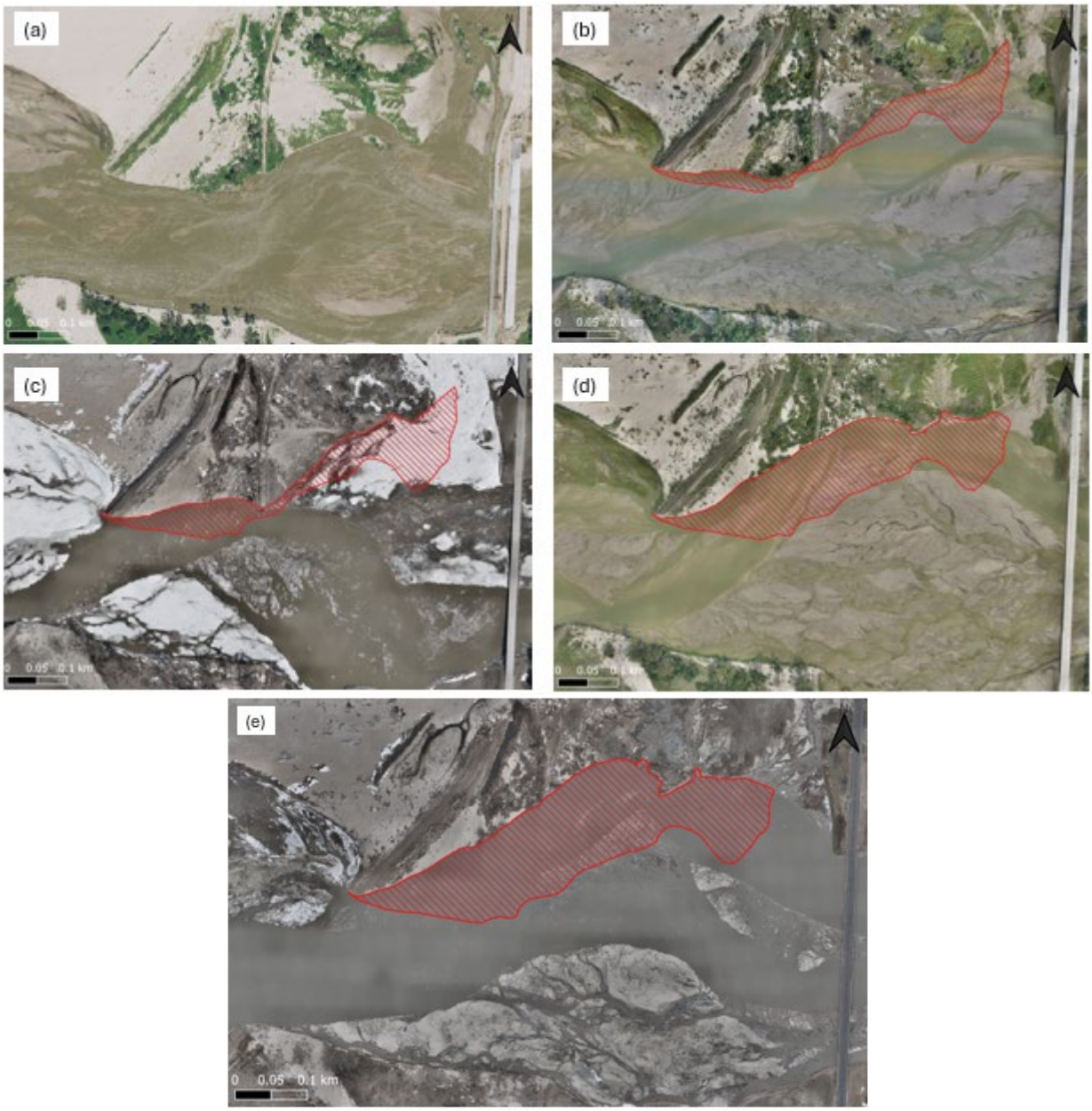

Figure 5.11 Progression of receding bankline at Area C from (a) 2020, (b) 2020 to Sept. 2022, (c) 2020 to March 2023, (d) 2020 to Aug. 2023, and (e) 2020 to Feb. 2024.

Figures 5.12, 5.13, and 5.14 show the process of calculating the eroded volume for Area B. Figure 5.12 shows the polygon that represents the areal difference between September 2022 and February 2024. Figure 5.13 shows the locations of measured elevation changes from the point cloud that was collected during the site visit. Some of the points are irregularly spaced and do not quite reach the bank; our script interpolates to correct for these discrepancies. Figure 5.14 shows the resulting raster with the lost elevation for each cell. The elevations are from 0 (dark blue) to 6 meters (dark red). Note that there are a few trees that bias the results high, but they make up a small part of the overall calculation and did not significantly affect the results.

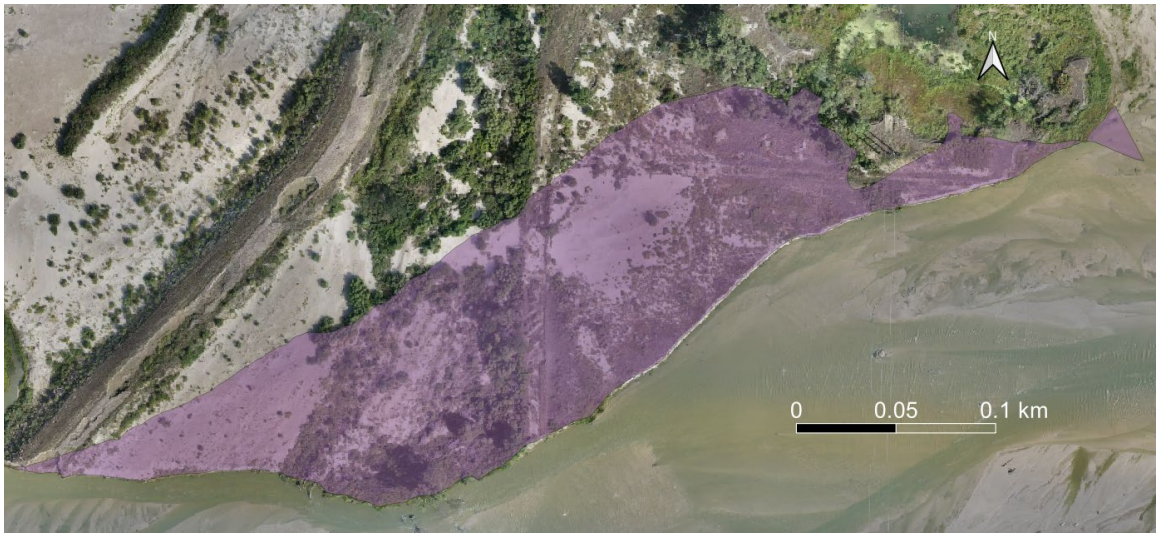

Figure 5.12 Area lost between September 2022 and February 2024

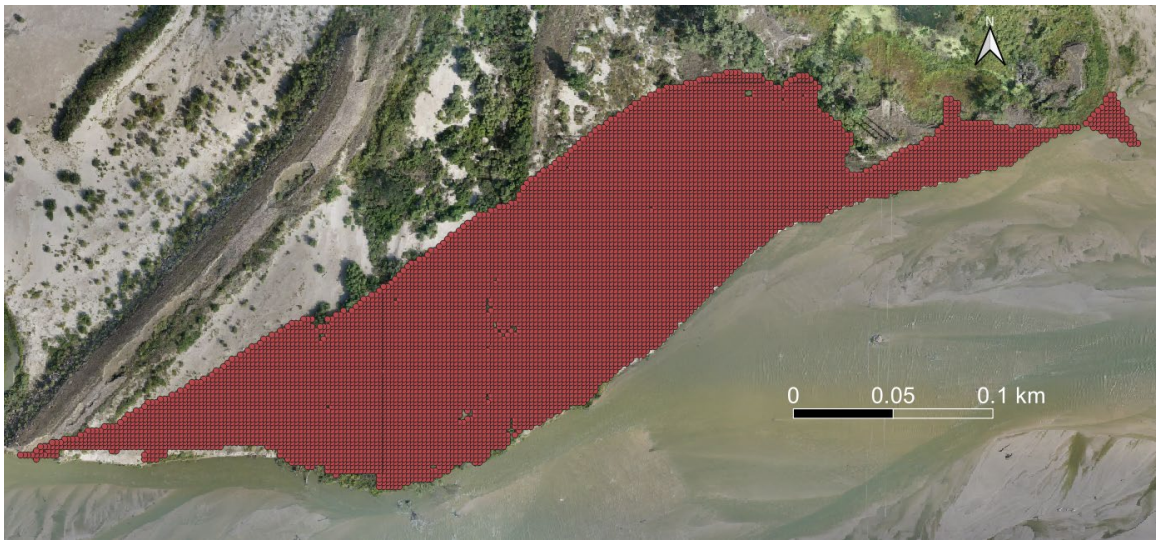

Figure 5.13 Point cloud elevation grid (irregularly spaced) (Sept 2022 – February 2024)

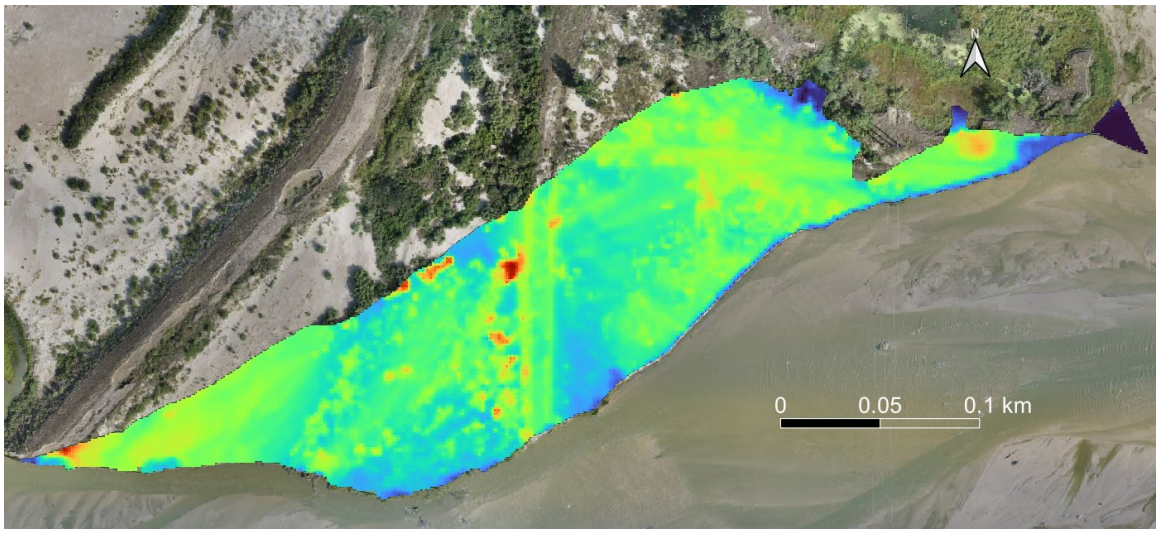

Figure 5.14 Resulting raster with lost elevation in each cell (Sept 2022 – February 2024)

Table 5.1 shows the volume loss in Area C with respect to the data collected in Fall 2022. For each period average elevation loss, planform area loss, and the total volume loss are shown. The lost planform areas calculated from the rasters were compared with polygon areas determined in QGIS and were within 1% (with slight variations due to rasterization of the areas). Between March 2023 and August 2023 a larger amount of volume eroded than between August 2023 and February 2024. The most erosion occurs between spring and fall.

Table 5.1 Eroded volumes for Area C

Period	Average elev. loss (m)	Lost planform area (m^2)	Lost volume (m^3)
9/22 to 3/23	2.12	9,500	20,150
9/22 to 8/23	2.38	30,670	72,970
9/22 to 2/24	2.39	35,780	85,690

Erosion losses can also be determined for Area C using Method 2 shown in Figure 5.7. The estimates for eroded volume in Area C using the second method are shown in Table 5.2. These losses are relative to the 2020 USGS DEM. There is an additional row of information because the 2020 DEM has been added to the list of available data.

Table 5.2 Estimates of sediment eroded from Area C since 2020 – calculated using 2020 DEM

Period	Average Elev. Loss (m)	Planform Area (m^2)	Estimated Volume (m^3)
4/20 to 9/22	1.75	20,800	36,520
4/20 to 3/23	1.98	30,610	60,520
4/20 to 8/23	2.35	50,450	118,730
4/20 to 2/24	2.43	54,658	132,890

Table 5.3 shows the difference in average elevation and volume calculations between methods one and two. The differences in average elevation between the methods were calculated by subtracting the elevation calculated between April 2020 and September 2022 from the rest of the volume calculations, then subtracting the result of those differences from the average elevations from method one. The differences between the volume calculation methods were calculated in a similar way as the differences in average elevation. The volume calculations between April 2020 and September 2022 were subtracted from the rest of the volume calculations in method two, then subtracting the volume calculation lost in method one from the respective resulting calculation. When calculating the average lost elevation using the two methods, it was nearly the same as the difference in the base elevations. In other words, the USGS DEM and the DEM produced by the point cloud produce similar results, but the average bed elevation of the river, which is used as the datum, has risen significantly between 2020 and 2022. In fact, the bed has risen by about 0.3 to 0.4 meters in the location of Area C, as shown in Figure 5.5. This corresponds to the difference in average elevation observed in the last column of Table 5.3.

Table 5.3 Comparison of Area C calculations

Period	Area lost (m^2)	Volume Lost Method 1 (m^3)	Volume Lost Method 2 (m^3)	Difference between Volumes (m^3)	Difference in avg. elevation (m)
9/22 to 3/23	9,500	20,150	24,000	3,850	0.405
9/22 to 8/23	30,670	72,970	82,210	9,240	0.301
9/22 to 2/24	35,780	85,690	96,370	10,680	0.298

5.4.2. Sediment availability and erosion upstream of the dam

The yellow and orange cross-hatched areas in Figure 5.8 represent available sediment deposits upstream of Spencer Dam. Determining the full extent of the Spencer Dam reservoir was challenging, but was done based on comparison of pre- and post-failure bed elevation profiles (Figure 5.3) and aerial images. The reservoir extended slightly upstream of the polygons shown in Figure 5.8, but the polygons represent the bulk of available sediment in the reservoir. Compared to Areas A and B, deposits upstream of Area A are much smaller and are similar to floodplain deposits in locations unaffected by the dam.

Table 5.4 shows the calculated estimates of available sediment deposits from the 2020 USGS DEM. This table includes the estimated average elevation, planform area, and estimated volume. From Table 5.4, in 2020, area A had an estimated volume of 11 million cubic meters and Area B had 1 million cubic meters. Collectively, the estimated volume of available sediment was almost 12 million cubic meters. These were post-dam failure amounts.

Table 5.4 Available sediment deposits estimated from the 2020 DEM in Areas A and B

Location	Planform Area (m^2)	Estimated Volume (m^3)
Area A	3,539,148	10,979,468
Area B	365,792	986,721

Figure 5.15 shows the progression of receding bank lines between April of 2020 and August of 2024. Much of the erosion is from Areas A and B immediately upstream of a chute which leads to the dam breach site. The progression starts with observations of the 2020 USGS DEM, followed by the 2020 NAIP aerial, then the 2022 NAIP aerial, and finally, the 2024 NAIP aerial. Colored areas show the erosion that occurred between the USGS DEM and each subsequent aerial image. Areas eroded between April 2020 and July 2020 are shown in green, areas eroded between July 2020 and August 2022 are shown in yellow, and areas eroded between August 2022 and August 2024 are shown in red. The period between April and July 2020 is shorter than the other two periods because an NAIP aerial was collected during the same year as the USGS DEM. The estimated eroded volumes for each time period are shown in Table 5.5.

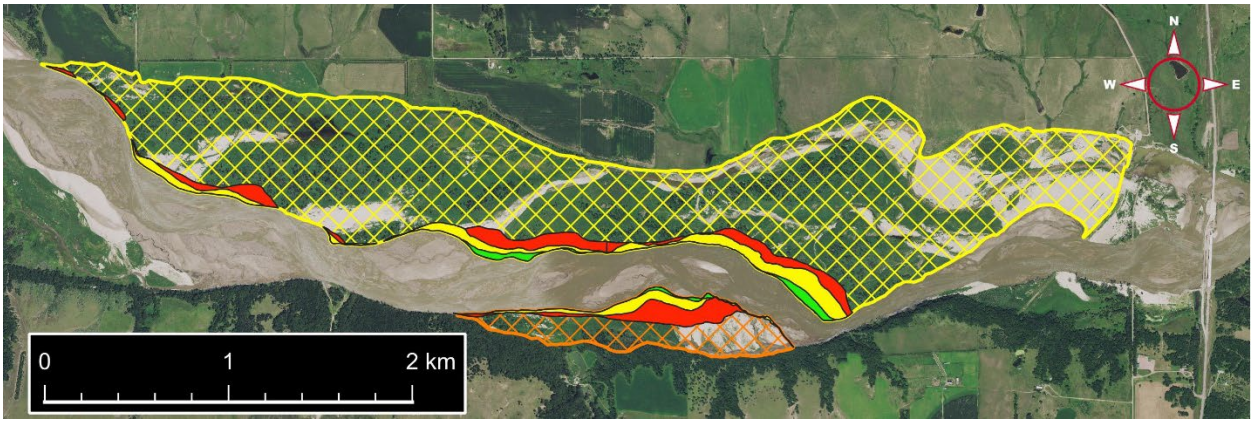

Figure 5.15 Biannual sediment loss polygons based on NAIP observations. Green – 2020 DEM to 2020 NAIP. Yellow – 2020 NAIP to 2022 NAIP. Red – 2022 NAIP to 2024 NAIP

Between the time of the 2020 USGS DEM and the 2020 NAIP aerial very little erosion was observed in Area B. The amount of erosion in Area B increased significantly between the 2020 and 2022 NAIP aerial images, and even more was observed between 2022 and 2024. Both areas of erosion clearly provide significant contributions to river sediment during high flow events.

Table 5.5 Estimates of sediment deposits eroded since 2020 – calculated using the 2020 DEM

Location	**Period**	**Planform Area (m^2)**	**Estimated Volume (m^3)**
Area A	4/20 to 7/20	27,792	102,047
Area A	4/20 to 8/22	160,236	586,598
Area A	4/20 to 8/24	296,316	1,058,381
Area B	4/20 to 7/20	5,084	17,393
Area B	4/20 to 8/22	46,409	153,490
Area B	4/20 to 8/24	116,059	354,407
Total A-B	4/20 to 8/24		1,412,789

5.4.3. Summary of sediment availability and erosion at the study site

Areas A and B are different than Area C because for Area C the UAS data from the project were used for calculating eroded volumes, while Areas A and B rely on historical external DEMs and aerial imagery. Areas A and B provide insight on the behavior of the channel and the progression of bank movements in the reservoir upstream of the project orthomosaics. Table 5.6 shows all the estimates of eroded volume since 2020 using the 2020 USGS DEM. For Area A, the eroded volume between 2020 and 2024 is just over a million cubic meters. This area provided the most eroded volume between all the areas of interest. Area B has contributed an estimated 350,000 cubic meters of eroded sediment. Sediment eroded from Area C was calculated using two different methods. For Area C, Table 5.6 shows calculations using the second method for direct comparison with calculations for Areas A and B. Between 2020 and February 2024, the estimated eroded volume for Area C is nearly 133,000 cubic meters. The total eroded volume between 2020 and 2024 for all three areas is estimated at about 1.5 million cubic meters. Based on the estimates provided in Tables 5.4 and 5.5, the sediment eroded from reservoir deposits since 2020 is roughly 12% of the volume of deposits available in 2020. Note that it is unlikely that all of the available sediment will be released in the near future, but there is potential for large quantities of it to be eroded in the coming years, especially as previously cut channels are reopened in Area A.

Table 5.6 Estimates of cumulative eroded sediment since 2020 – calculated using the 2020 DEM

Location	**Period**	**Planform Area (m^2)**	**Estimated Volume (m^3)**
Area A	4/2020 to 7/2020	27,792	102,047
Area A	4/2020 to 8/2022	160,236	586,598
Area A	4/2020 to 8/2024	296,316	1,058,381
Area B	4/2020 to 7/2020	5,084	17,393
Area B	4/2020 to 8/2022	46,409	153,490
Area B	4/2020 to 8/2024	116,059	354,407
Area C	4/2020 to 9/2022	20,800	36,520
Area C	4/2020 to 3/2023	30,610	60,520
Area C	4/2020 to 8/2023	50,450	118,730
Area C	4/2020 to 2/2024	54,658	132,890
Total A-C	4/2020 to 8/2024[†]		1,545,679

[†]A small amount of erosion was observed at Area C between 2/2024 and 8/2024 that was not included in this calculation

5.4.4. Sediment volumes released immediately after the dam failure

For reference purposes, sediment released between the time of the dam breach and the time when the USGS DEM was produced in 2020 were estimated by determining the difference between the 2020 DEM and the 2013 DEM collected by NDNR. This was done for the entire region upstream of the dam, using the same script that was used to calculate sediment deposits. The script did require some modification because the 2013 DEM is a 2-m by 2-m raster and the 2020 DEM is a

1-m by 1-m raster. Nevertheless, we were able to estimate the total volume lost between 2013 and April of 2020. The majority of the sediment difference between these two years is due to what was eroded during the dam breach. Eroded volumes were estimated for the two reaches shown in Figures 5.16 and 5.17, which are 6 km and 10 km reaches upstream of the dam, respectively. For these two reaches, the estimated depths of eroded sediment are shown in 2-m by 2-m rasters. Note that in contrast with Figure 5.10, red areas in Figures 5.16 and 5.17 represent eroded sediment and blue areas represent remaining deposits.

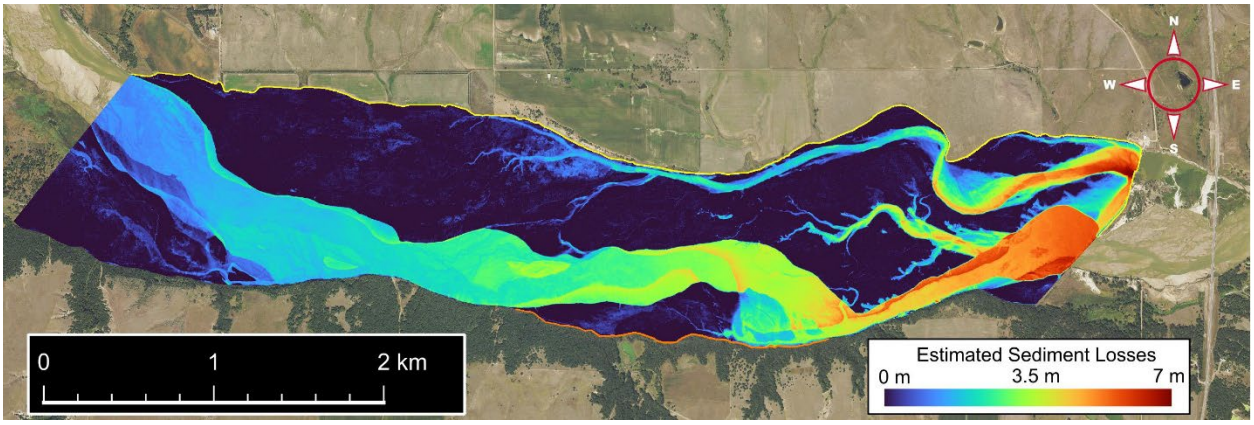

Figure 5.16 Sediment losses upstream of Spencer Dam between 2013 and 2020 DEMs for a 6 km reach upstream of Spencer Dam

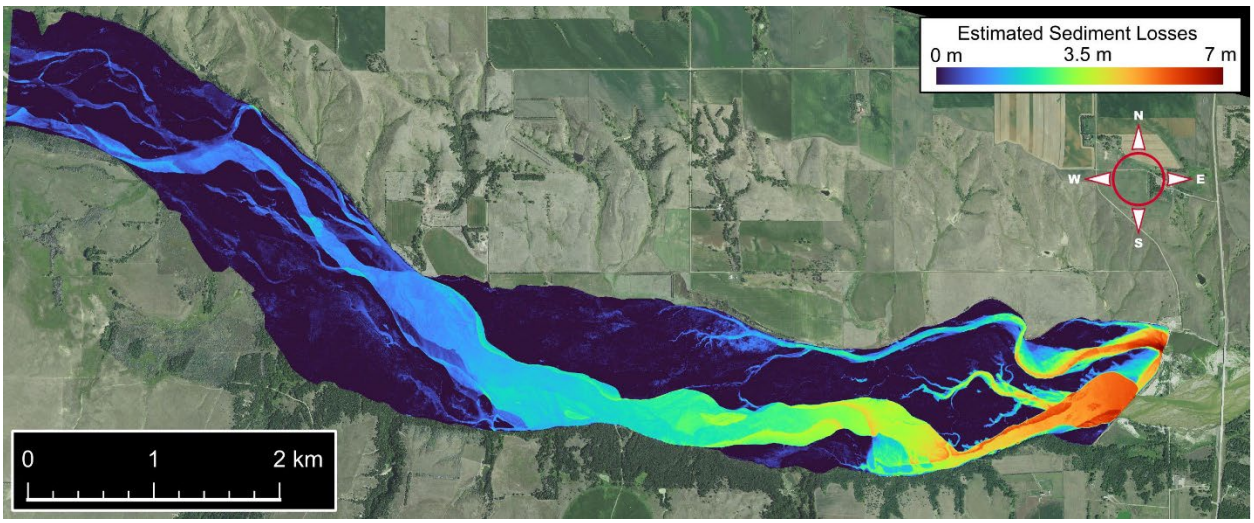

Figure 5.17 Sediment losses upstream of Spencer Dam between 2013 and 2020 DEMs for a 10 km reach upstream of Spencer Dam

The eroded sediment depths were then integrated over both rasters, and the resulting eroded volumes are provided in Table 5.7. The volumes of sediment shown in Table 5.7 are about five times greater than the volumes eroded between 2020 and 2024. Also of note is that the eroded volume calculated for the 6-km reach is about 95% of the eroded volume calculated for the 10-km reach. This confirms that the Area A and B deposits represent the vast majority of the sediment remaining in the reservoir.

Table 5.7 Differences between 2013 and 2020 DEM upstream of the dam

Sediment Deposit	***Volume Eroded (m^3)***	***Rasters used to Identify Remaining Sediment***
Area 6 km upstream of dam	7,419,438	This is basically the sediment that was eroded between 2013 and 2020 after the dam failure, but only up to 6 km upstream. There are far less signs of erosion upstream of this point.
Area 10 km upstream of dam	7,830,965	Same as above but for 10 km upstream of the dam.

6. Hydraulic Modeling

6.1. Modeling Approach

To model the long- and short-term changes of the Niobrara, QGIS and HEC-RAS were both used. QGIS is an open-source geographic information system. HEC-RAS is the Hydrologic Engineering Center's River Analysis System. HEC-RAS is used to perform one-dimensional steady flow, one and two-dimensional unsteady flow calculations, and sediment transport/mobile bed computations. In this study, it was used primarily for one-dimensional modeling. Efforts were made to also produce a two-dimensional model, but difficulties associated with self-formed bathymetries and river ice impacts led to a 2-D model that was unsatisfactory. Some discussion of two-dimensional modeling is provided for future use.

6.1.1. Preliminary one-dimensional model

Prior to data collection, the 2020 USGS DEM and image-based raster files were used for the development of the hydraulic model. These were imported into QGIS, merged and clipped to the area of interest. Imagery raster files were also merged and clipped. Using the USGS elevation data, cross-sections were created in QGIS as well. The clipped DEM and cross-sections were uploaded to HEC-RAS.

Once the DEM and cross-sections were uploaded to HEC-RAS, the right and left bank lines and the center line of the Niobrara River were directly defined on the RAS Mapper. Boundary Conditions were defined: the inflow conditions used a flow hydrograph from the gaging station at Highway 11, and the outflow conditions used normal depth. The inflow boundary condition line was at the start of the river thalweg line. The outflow boundary condition was positioned after the last cross-section. The flow rate (cfs) data was collected from the Nebraska Department of Natural Resources. By then, a site visit had been completed, and orthomosaics of the site were available. The discharge hydrograph for the HEC model was for the same time period as the September 2022 site visit. To run the 1D steady model, the geometry (DEM and cross-sections) and hydrograph data were entered into the model (the discharge was set to be constant for simplicity).

The first model run worked but the DEM data collected by USGS did not contain bathymetry data, only water surface elevations and elevations outside of the flow area. The DEM data may work okay for high flows but not as well for typical flows in the river. The first step to improve the model was to better assess Manning’s roughness. Land cover data was found and uploaded into the HEC-RAS model. The model was rerun with the land cover data, but the model results were not affected much.

In QGIS, a shapefile was created to represent the land cover data. Using the create polygon tool, polygons were created and labeled with Manning’s roughness coefficients for homogenous areas identified in aerial images. This was done for both Highway 11 and Highway 281 sites, and Manning’s roughness coefficients were assessed for each polygon using the UAS images collected in September 2022. The resulting shapefile was saved as a GeoTiff file and uploaded into HEC-RAS. The model was rerun, and the model changed but flows covered the entire river and the flood plains. The results were clearly inaccurate, with much of the inaccuracy being from

excessive Manning's roughness but also still due to the lack of accurate bathymetry. To improve Manning's roughness, literature about rivers in Nebraska was reviewed and a Manning's roughness of 0.02 was selected. This was based on Randle and Samad's (2008) estimation of Manning's roughness for the Platte River. The Niobrara River is similar to the wide, shallow, and sandy Platte River.

To improve topography estimation, a digital elevation model was rasterized from the UAS point clouds. In CloudCompare the point cloud (.las file) was selected in the DB Tree. Under the Properties window, the RGB was switched to a Scalar field. Then under the tools tab, *projection* and *rasterize* were selected. The active layer that was used was the height grid values, the direction was in the Z direction, and the cell height was averaged and interpolated with average values. Cells that had no data were left empty. Although the new DEMs were a more accurate representation of the actual flow area for HEC-RAS, the UAS data still did not add bathymetry because photogrammetery results did not include submerged areas. The next important step, the inclusion of better bathymetry, was not possible until bathymetry data were collected in August of 2023 and processed.

6.1.2. One-dimensional model

To improve the Niobrara River model, a simple one-dimensional bathymetry was implemented. First, two project models were created, one using metric units and the other using US Customary units. The two models were created to confirm that data were being correctly entered in HEC-RAS. Both models had the same reference image – the August 2023 orthomosaic image; cross-sections were in the same positions; and widths, depths, and the profile slope of the channels were the same. Both models also had the same flow rate (1500 ft^3/s or 42.47 m^3/s), and all cross-sections had the same shape (rectangular). The two models showed no differences in results, so we elected to use the metric system for the one-dimensional model.

Starting with simple cross sections, the cross sections were slowly modified to make them more realistic and representative of the model site. The cross-section shapes and depths were slowly adjusted to provide an accurate representation of the river. The shapes of cross-sections and possible flow depths were assessed based on bathymetric data collected in 2023 and on estimates using the orthomosaic imagery as a reference. At river bends, cross-sections were slightly more triangular with the thalweg moved to the outside of the channel bend and with the depth slightly deeper on the outside. Where the thalweg was positioned depended on the channel planform. For instance, the thalweg was positioned on the left side of the cross-section for turns to the right and on the right side of the cross-section for turns to the left. Where the flow was straight or if there were braids in the channel, the cross-sections were left as rectangular. The cross-sections were adjusted manually in the *Graphical Cross-section Editor* of HEC-RAS by clicking and dragging the points in the cross-section to move them. Points were deleted or added from the *Options* tab using *delete points* or *Add Sta/Elev points*. Once the cross-sections were adjusted, the river profile was checked to verify the expected changes in the water surface. The model was re-run, and the process was repeated, making sure that the water surface was similar to the banks identified in the orhomosaics; this was repeated until the banks were within about 10 centimeters of expected locations.

After the water surface elevation was close to identified banks for each cross-section, hand-held GPS cross-sections were used to further improve the model. Nearby cross-sections were modified to better match the six cross-sections collected at Highway 281 using GPS. For GPS cross-sections that were incomplete, the measurement tool in QGIS was used to determine the distance between the last measured point and the opposite bank. The unmeasured part of the profile was then extrapolated in HEC-RAS to represent the missing information. Extrapolated points were estimated using the orthomosaic image and realistic prediction of the shape and depth. Once the implementation of the six cross-sections was complete, the profile of the river was checked to make sure the water surface slope was reasonable. The model was rerun to make sure that the water surface edges were in agreement with orthomosaic observations.

Finally, cross-sections that did not have GPS measurements were adjusted to improve model performance. This step required some well-educated guesses of how the river transitioned between sections where the cross-section shape was directly measured. Using the observed data and UAS orthomosaics as guidelines, the interpolated cross-sections were created for a smooth transition between the observed cross-sections. The depths of these interpolated cross-sections were adjusted to maintain the slope of the river and to imitate flow conditions of the observed data.

6.1.3. Quasi-unsteady sediment transport model

A one-dimensional quasi-unsteady flow model for sediment transport was developed to understand the outputs of the analysis. Quasi-unsteady flow, like unsteady flow, produces a hydrograph but it is created by a series of steady flow pulses. The durations of the pulses can vary in time. The quasi-unsteady data needs cross sections for the initial boundary conditions. The boundary condition for the first cross-section is a flow series. The inputs for the quasi-unsteady flow series are the simulation time, flow duration in hours, computation increments in hours, and the flow in meters cubed per second. The flow duration is the duration of time where the flow remains constant. The computation increment is the hydraulic and sediment transport time step. For every computation increment, the cross-section and the hydraulics are updated. The computation increment cannot be larger than the flow duration. The computation increment is further subdivided into bed mixing time steps. The bed mixing time step is mainly for the constantly changing bed gradation. The outflow boundary condition is either normal depth, rating curve, and stage series, where the normal depth input is the friction slope at the outlet of the model. The rating curve inputs are the flow in meters cubed per second and the stage in meters. The stage series is set up similarly to the flow series but has stage duration in hours and the stage in meters. For the models we tested, normal depth was used for the outflow boundary condition. Once the boundary conditions were set, the next step was to input sediment information.

Within the sediment data window, there were four tabs. Two of the tabs were necessary for an initial run of the sediment transport analysis, these were the initial conditions and transport parameters and boundary conditions. For the initial conditions and transport parameters, it was important to choose the right transport function, sorting method, and fall velocity method for the Niobrara River. However, since this was an initial run, the Laursen (Copeland) transport

function, Copeland (Ex7) sorting method, and Rubey fall velocity method were chosen. Once those methods were chosen, the sediment information was entered in the Define/Edit Bed Gradation button. Then, in the table with all the cross-sections, the bed gradations were set to the bed gradation that was just created. Then "Use Banks for Movable Bed" was selected to allow lateral erosion, and the maximum depth was set to 1 meter. Under the boundary condition tab, for an initial run, an equilibrium load was run through the first cross-section. The next step for the initial run under the "Options" Tab was the Bed Change Options (1D), and we wanted the deposition for the main channel and the overbank to be Veneer and the erosion for the channel to be Veneer. The Veneer method was to allow cross-section changes, allowing the bed to change due to the river flow.

Finally, the model could be run under the sediment transport analysis button. The correct geometry, quasi-unsteady flow, and sediment files had to be in the sediment transport plan as well as the start date and time and end date and time. Then the sediment transport analysis could be run. The sediment output was shown on the home page under the View tab at the bottom as the "Sediment Output." This is where temporal changes in the river profile and individual cross-sections were plotted.

6.2. Estimating Points for Incomplete Cross-sections

Quite a few of the cross-sections measured with GPS in August 2023 were incomplete because of the swiftness of the river. In other words, many of the cross-sections that were collected were not from bank to bank. There was a total of 6 cross-sections that were collected at the Spencer site and only one was a complete cross-section (Cross section 4 - there are duplicates of Cross-section 4). The numbering of the cross-sections starts at 1 furthest upstream and increases in the downstream direction.

Figure 6.1 is an overlay of the cross-sections on the August 2023 orthomosaic. All 6 cross-sections are useful for estimating depths in locations where cross-sections were not measured. There is only one complete cross-section, and the other 5 cross-sections do not reach from bank to bank. Points were estimated to complete the incomplete cross-sections. These estimated points were determined using the measured points in combination with the August 2023 aerial imagery and approximation of the expected river cross section shape. Where the main channel was straight, the cross section was uniform in depth and relatively shallow, almost rectangular or trapezoidal in shape. In areas where the main channel meandered, the deepest part of the channel was towards the outer bank of the meander.

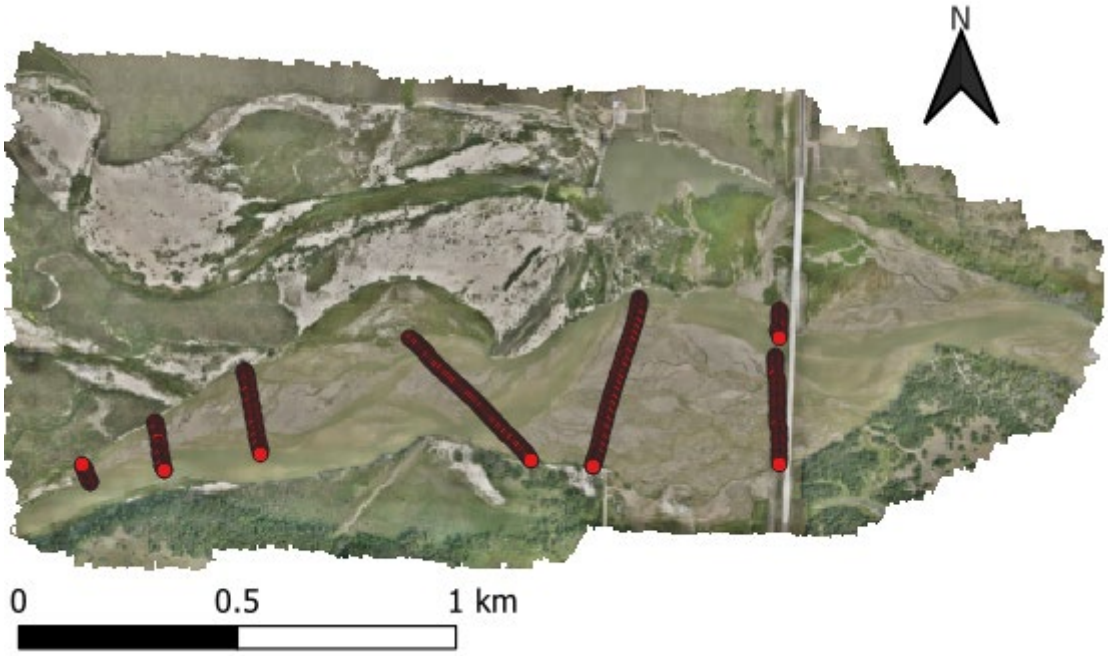

Figure 6.1 Overview of August 2023 measured cross-sections

Figure 6.2 shows the cross-section that is farthest upstream. The solid black line is the collected GPS data points that have been adjusted to the USGS vertical datum. The black points are the same points that are shown in the first cross-section in Figure 6.2. The red dashed line is the points that were estimated based on the brightness of the orthomosaic and the distance between banks. The dark blue line is an approximation of the water surface elevation. The approximate width of the cross-section is 94.8 meters. The farthest that the collected data reached was 43.85 meters. There was 50.95 meters of cross section that was estimated. There are estimates approximately every three meters to the far bank. Where data collection for cross-section 1 stopped on the orthomosaic, there are large standing waves. This indicates that the water is moving at critical velocity. The main channel is flowing straight, so the bed is expected to be relatively uniform in depth at this cross-section. Based on the orthomosaic and positions of standing waves, the bed appears to get shallow close to the bank. The depth of the main channel is estimated to be about 0.44 meters. The last approximated point on the RDB is at the same elevation as the measured water surface on the LDB.

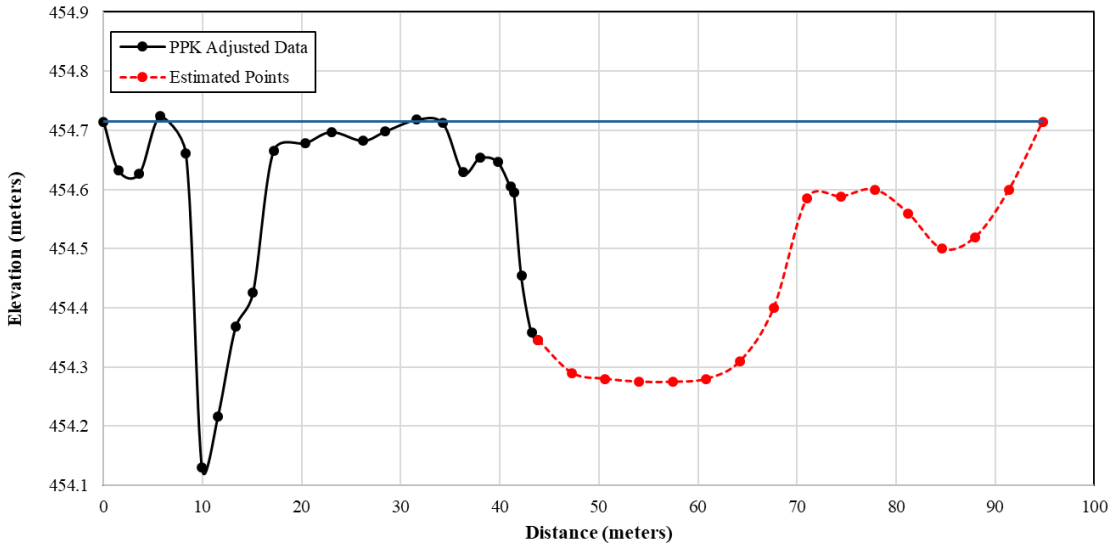

Figure 6.2 Cross-section 1

Figure 6.3 shows the second cross-section with an approximate total width of 142.92 meters measured using the QGIS measuring tool. The length of the collected part of the cross section was about 116.57 meters, and the part of the cross section that was estimated was about 26.35 meters in length. The cross-section itself is not far downstream of cross-section 1, meaning the overall shape of the channel should be similar. The cross-section appears to drop off at a gradual rate but standing waves in the aerial imagery show that the main channel flows along the right descending bank at critical depth, indicating a significant drop with the channel forming a U-shape. The estimated guess for the depth of the channel is about 0.51 meters. The water surface elevation of both the perched stream and the main channel are sloped because the cross-sections were not perfectly perpendicular to the flow (note, however, that the figure exaggerates the significance of the water slope).

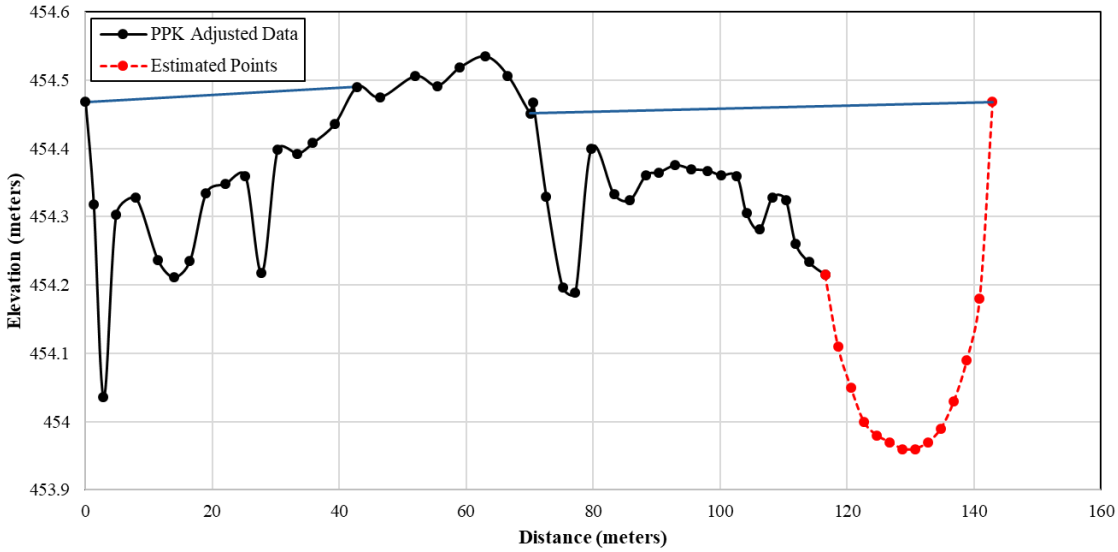

Figure 6.3 Cross-section 2

Figure 6.4 shows cross-section 3 with an approximated width of 261.13 meters measured using the QGIS tool. The collected data covered 194.43 meters of the cross-section, leaving 66.7 meters to be estimated. Cross-section 3 is similar in shape to cross-sections 1 and 2. However, the main channel has shifted away from the right descending bank just slightly compared to cross-sections 1 and 2. From the aerial image, it is shallow near the right descending bank, but the main flow channel is narrower than the previous two cross-sections. Because the main flow channel is narrow, the bed is expected to be deeper. The estimated depth is 0.67 meters. On the right descending bank is a smaller perched channel that can be seen in the aerial image. The water surface elevation, as in Figure 6.3, is again sloped.

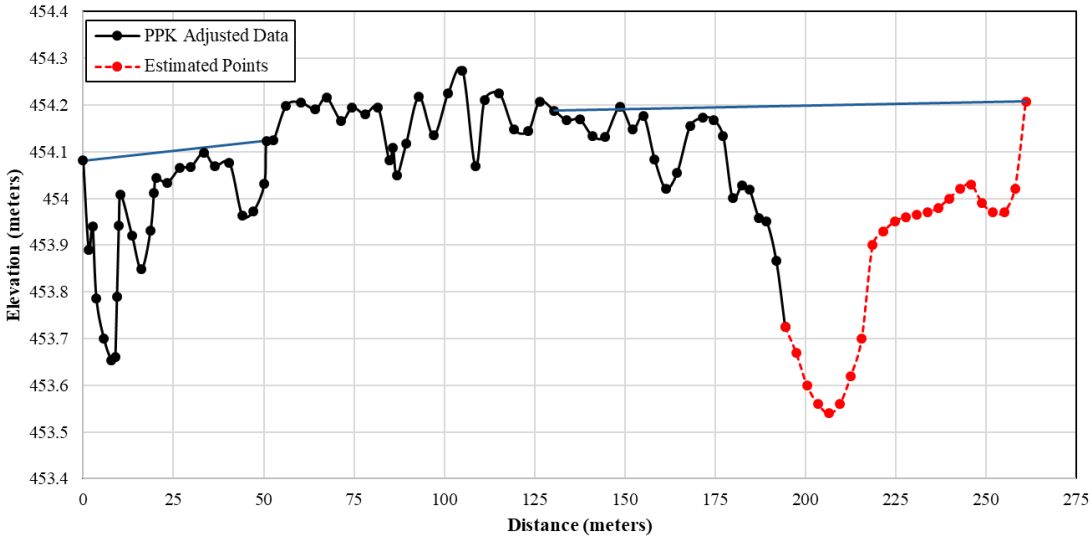

Figure 6.4 Cross-section 3

Figure 6.5 shows the only complete cross-section that was collected. The left bank of the cross-section is higher than the right bank of the cross-section. This is because the left bank is slightly upstream of the right bank. The cross-section itself was collected at a diagonal compared to the cross-sections previously mentioned.

Figure 6.6 shows the fifth cross-section, which is just downstream of the failed dam. This cross-section is incomplete at the left descending bank instead of the right descending bank. The approximate total width of the cross-section is 421.49 meters, but much of this is a wide sediment flat. The collected data covers 398.15 meters of the cross-section, leaving 23.34 meters to be estimated. For determining the water surface elevation of the main channel, the aerial image in QGIS was used since no collected data point was tagged as a water surface for this cross-section. Based on the aerial image and the site visit, the water was moving at great velocity, and the outside bank was very steep. From these observations, it was assumed that the channel was deep and U-shaped close to the outer bank. The estimated depth for the main channel was about 0.65 meters. The water surface elevation for the main channel was not sloped, though the water surface elevation in the perched streams was sloped.

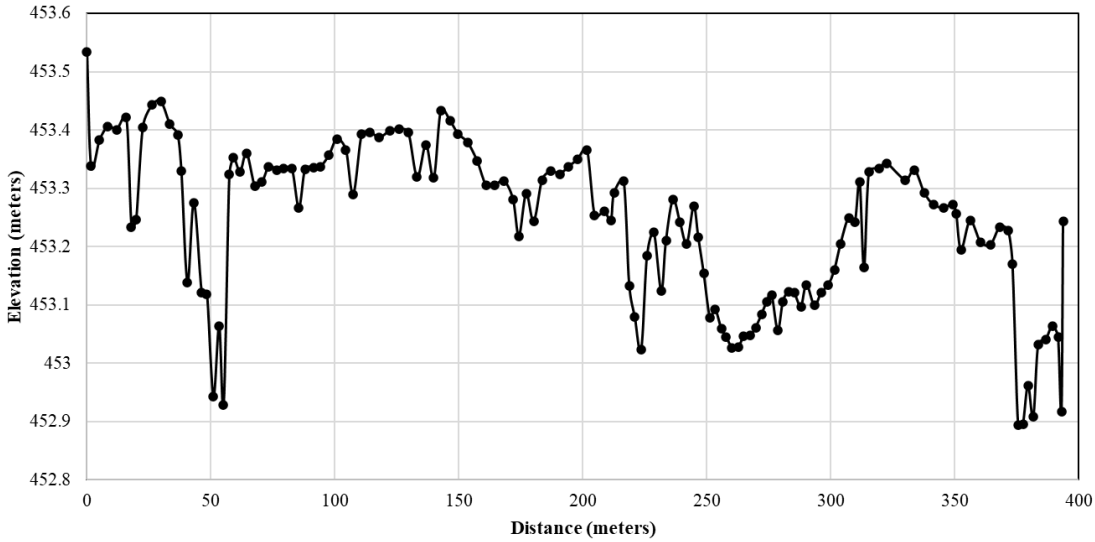

Figure 6.5 Cross-section 4

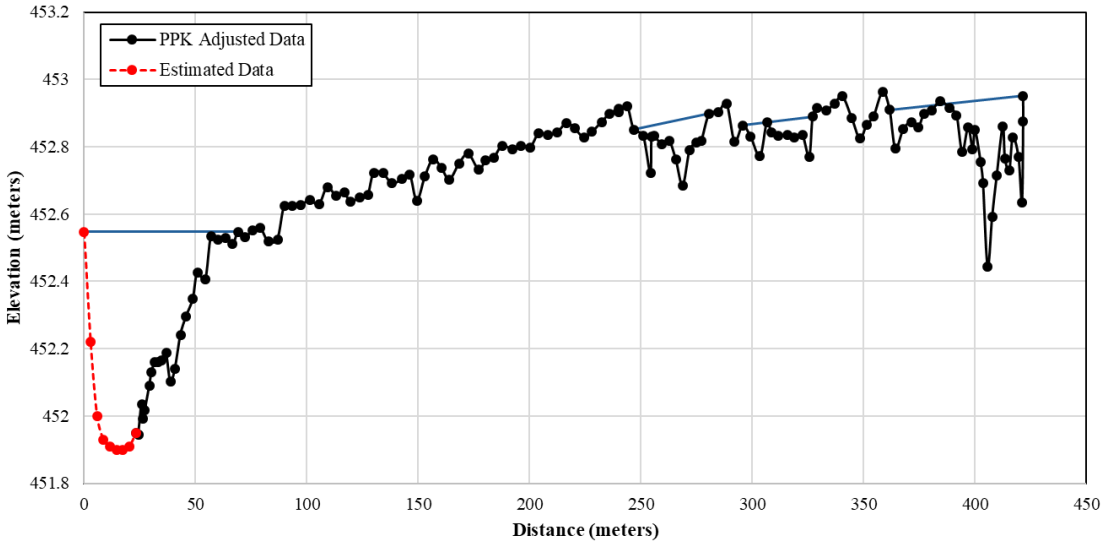

Figure 6.6 Cross-section 5

Figure 6.7 shows the sixth cross-section. When collecting this cross-section, we started at one bank and collected as far as we could into the main channel. Then we started at the opposite bank and collected as far as we could in the opposite direction. This left a portion of the cross-section to be estimated. The approximate total width of the cross-section was 351 meters. The data collected from the left descending bank spanned about 61 meters, and from the right descending bank, about 246.77 meters. There were about 43.23 meters in the middle of the cross-section to be estimated. The aerial image shows that where no data were collected, the water was moving very quickly, and there were standing waves. But on the left side of the cross-section, gradual sloping was observed in the image, followed by a drop-off. The bed appears to rise abruptly near the last point collected on the right side of the cross-section. The depth is estimated to be about

0.6 meters. The water surface elevation across the cross-section is sloped and each section has different slopes.

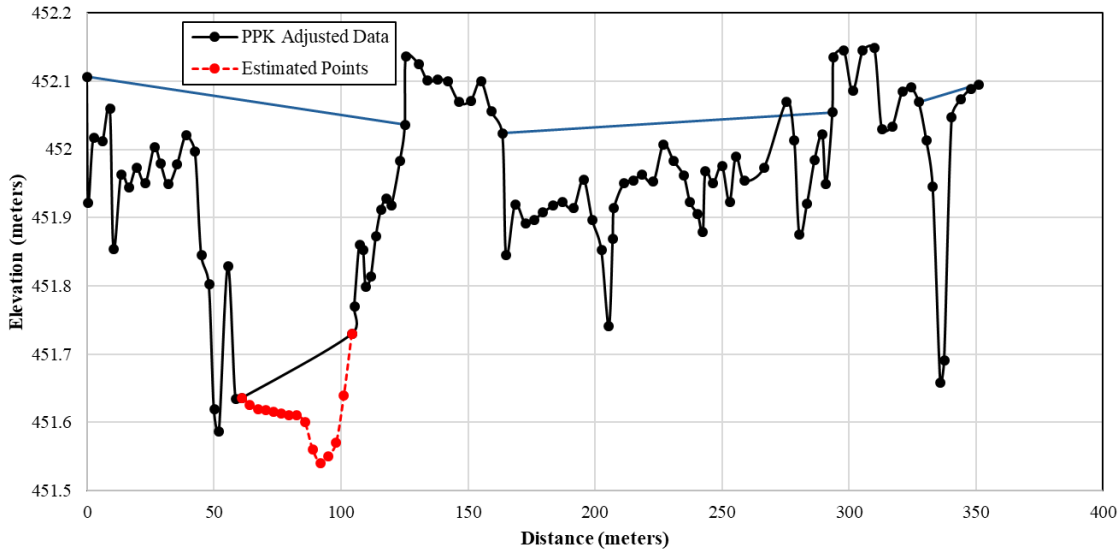

Figure 6.7 Cross-section 6

6.3.Model Runs

6.3.1.Simple Model Run

For the hydraulic model of the Highway 281 site, the slope of the longitudinal profile was the same slope as the PPK GPS data that were collected in August 2023. The slope of the profile was used as the baseline for elevation differences between the observed cross-sections. The main focus of the cross-sections was the flow in the main channel. HEC-RAS assumes the elevation of the water surface is level across the cross-section because the cross-section must be perpendicular to the flow. In HEC-RAS, the water surface elevation across each cross-section has no slope, but the cross-sections collected in the river during site visits had multiple channels with perched water surfaces and, in some cases, sloping water surfaces. This indicates that: (1) not all of the subchannels have the same slope, and (2) the collected cross-sections were not perfectly perpendicular to the flow. The boundary conditions for the steady flow data were critical flow for the upstream condition and normal depth with a slope of 0.001759 for the downstream condition. The flow discharge was 42.47527 cubic meters per second (1,500 cubic feet per second), and the Manning's roughness was set to 0.02 as previously stated. The flow regime for the steady flow analysis is mixed.

Figure 6.8 shows the result of the steady flow analysis in the longitudinal profile. This profile follows the "centerline" of the river. The centerline is placed where the thalweg is located. The black line represents the deepest part of the channel (the deepest part of each cross-section). The red dotted line is the critical profile line, and the green dashed line is the energy grade line. Figure 6.8 shows that the flow remains at or very close to critical throughout the entire modeled reach. We believe that this is correct because the August 2023 orthomosaic in Figure 6.1 shows standing waves in the main channel throughout the entire modeled reach.

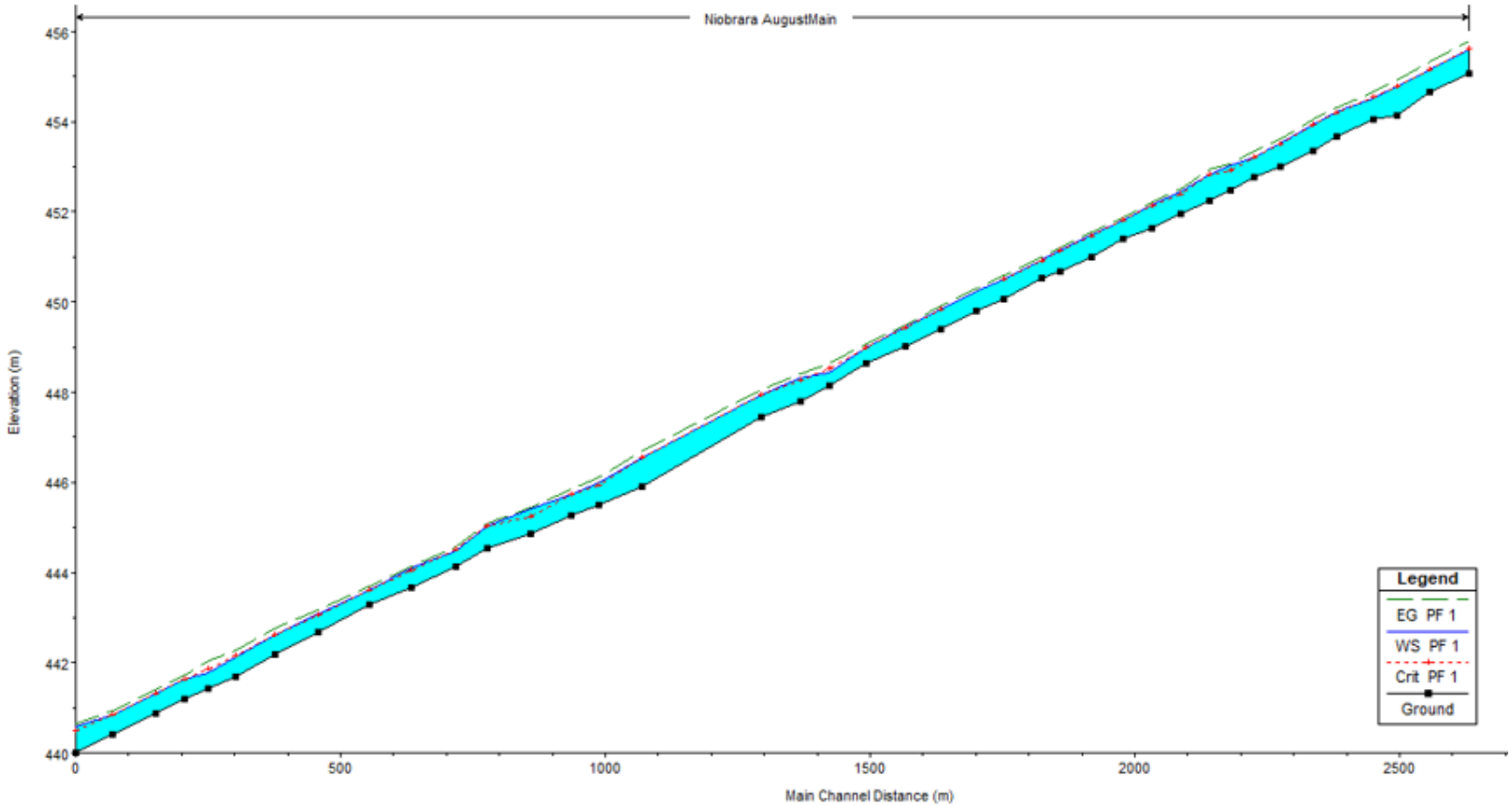

Figure 6.8 HEC-RAS longitudinal profile result

Figure 6.9 is the model result for cross-section 1, the same cross-section as in Figure 6.2. The water surface elevation was approximately 7 centimeters higher than the identified banks. The Manning roughness may have been a little too high or the approximated cross sections were a little too shallow. In any case, near critical flow depth, the flow depth is highly sensitive to inaccuracies. The colors in the cross-section represent the velocity of the water flowing through the cross-section. The light green-yellow color represents the velocity of 0.8 m/s. The green color represents the velocity of 1.0 m/s. The light blue color represents the velocity of 2.0 m/s. The dark blue color represents the velocity of 2.2 m/s. The velocity is highest around the area where the GPS Data for this cross-section stops.

Figure 6.10 is the model result for cross-section 2, the same cross-section as in Figure 6.3. Like Figure 6.9, the water surface elevation is slightly higher than the identified banks. The water surface is also slightly higher than the critical flow elevation. This cross-section result is similar to what is observed in Figure 6.3. The water surface elevation is approximately 5.5 centimeters above the identified banks. The highest velocity flows near where the GPS Data ended. The highest velocity is estimated to be 2.0 m/s.

Figure 6.11 is the model result for cross-section 3, the same cross-section as in Figure 6.4. This result is different than the previous cross-section results in terms of where the water surface elevation is and what the velocity distribution across the cross-section is like. There are two independent channels in the cross section but without applying bifurcations, HEC-RAS is unable to distinguish between them. As a result, the overflow channel on the left side of the floodplain is predicted to carry more water than it carries. The water surface elevation is higher than the identified left bank but is correct on the right bank. For the main channel on the right of the cross-section, the water surface elevation is below the right descending bank. The flow in Cross-section 3 is critical. The highest velocity is calculated to be 1.8 m/s, and like in the previous cross-sections, the highest velocities are predicted where the GPS Data ends.

Figure 6.12 shows the results for cross-section 5, the same cross-section as in Figure 6.6. The predicted water surface elevation for this cross-section is correct. The cross-section does not have an identified bank elevation, but measurements from nearby GPS data show that the predicted elevation is good. Figure 6.6 shows that there are several perched streams. HEC-RAS does not predict any flow in the perched streams since it presumes that all flow for a cross-section is at the same elevation. However, there is comparatively little flow in the perched streams, and the result is that HEC-RAS accurately predicts the flow distribution for this cross-section. The highest velocity is approximately 2.0 m/s in the main channel.

Figure 6.13 is the model result for cross-section 6, the same cross-section as in Figure 6.7. A depth adjustment was made to the channels on the right descending bank of the cross-section in Figure 6.6. This was done to force more flow into the main channel on the left descending bank to cause the water surface elevation to increase. The problem is that the channels on the right descending bank are low-flow channels with relatively deep bathymetry on the downstream end. This is problematic for the 1-D version of HEC-RAS because it does not distinguish between the different flow regions. Even with this adjustment, the predicted water surface elevation is below the expected water surface elevation across the entire cross-section. However, the flow is at

critical flow and the highest velocity is where there was no GPS Data. The highest velocity is calculated to be 1.6 m/s, which is slower than the previous cross-sections, but this cross-section is just upstream of the bridge crossing and just downstream of where the channel widens considerably.

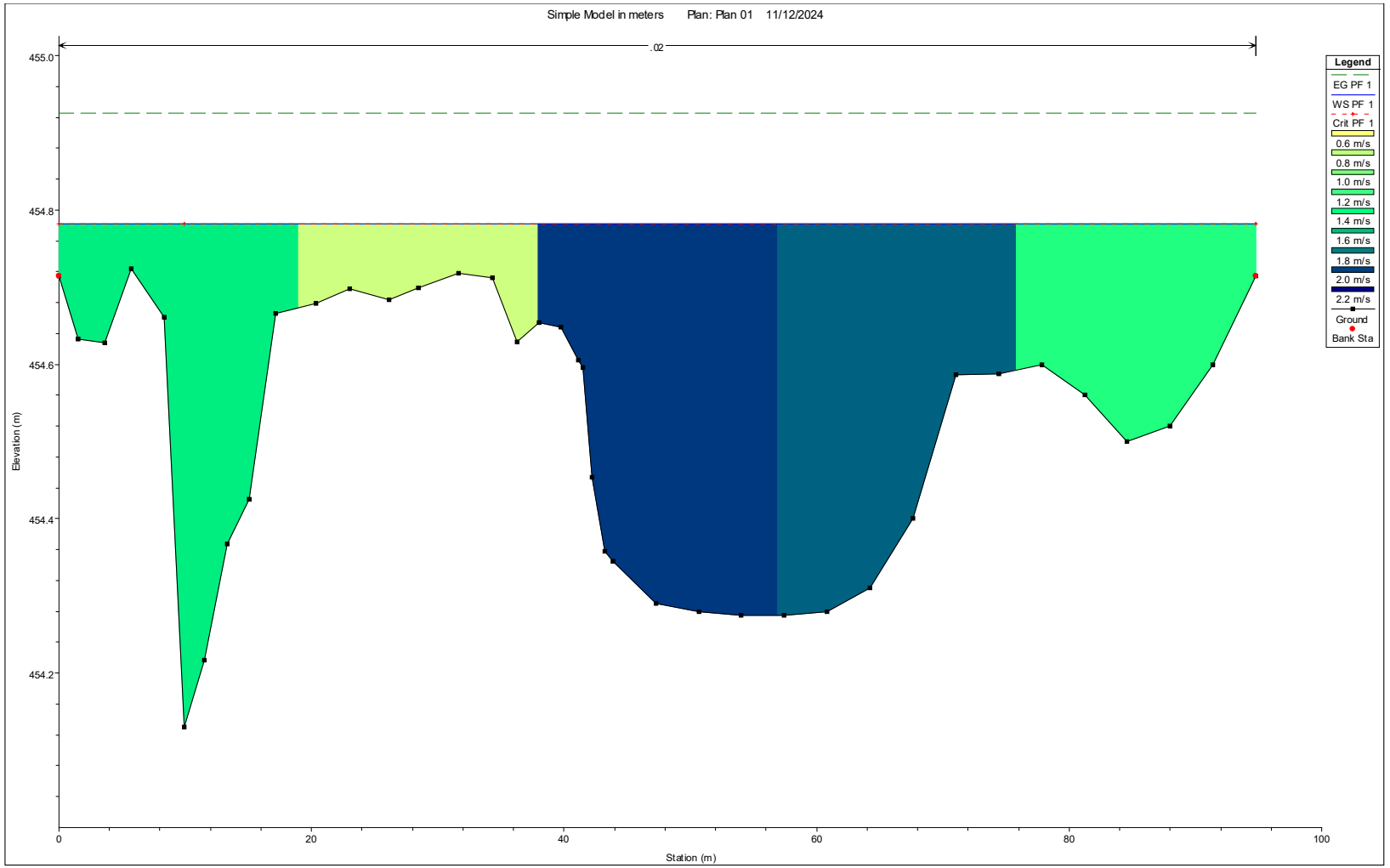

Figure 6.9 Cross-section 1 model result

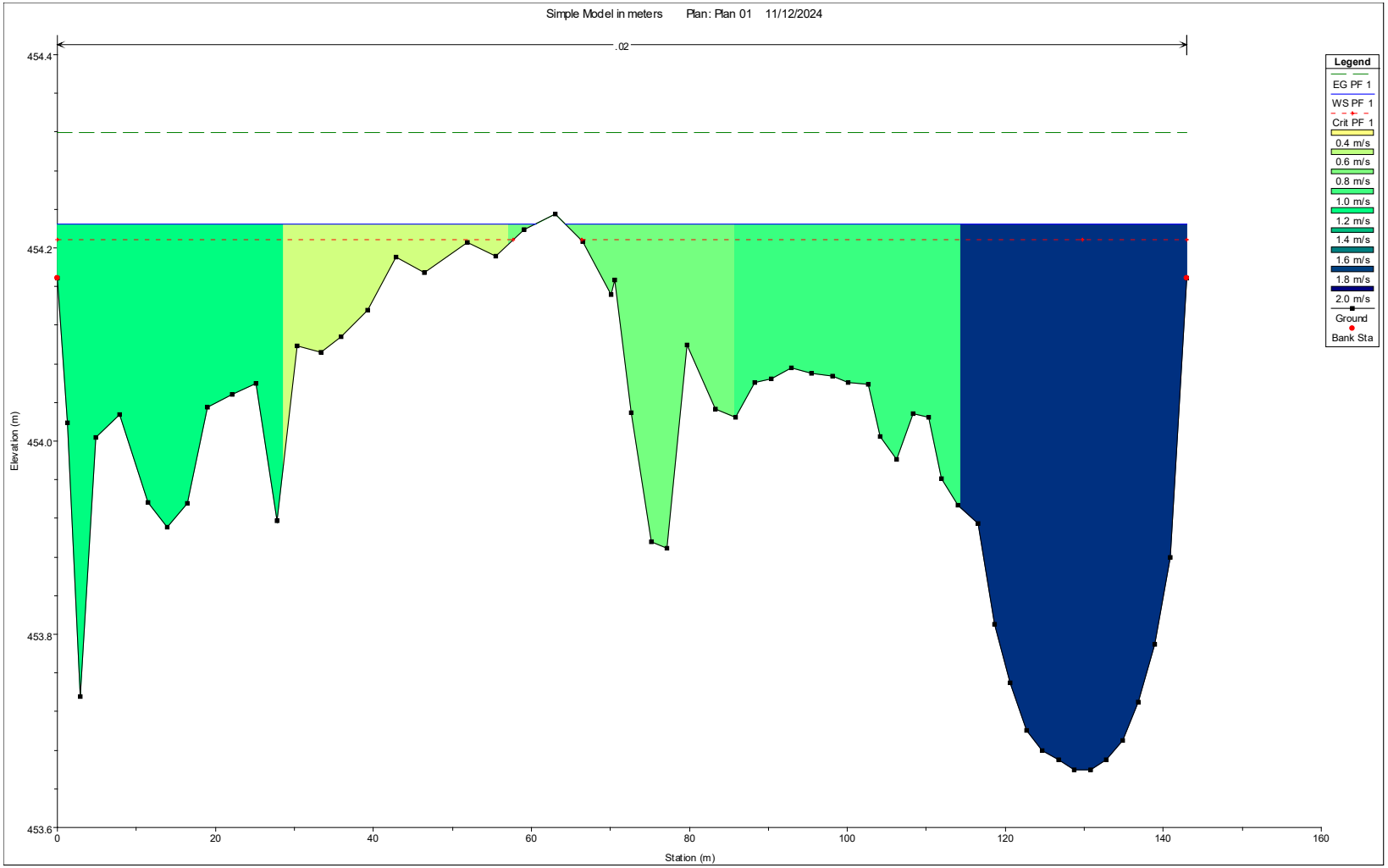

Figure 6.10 Cross-section 2 model result

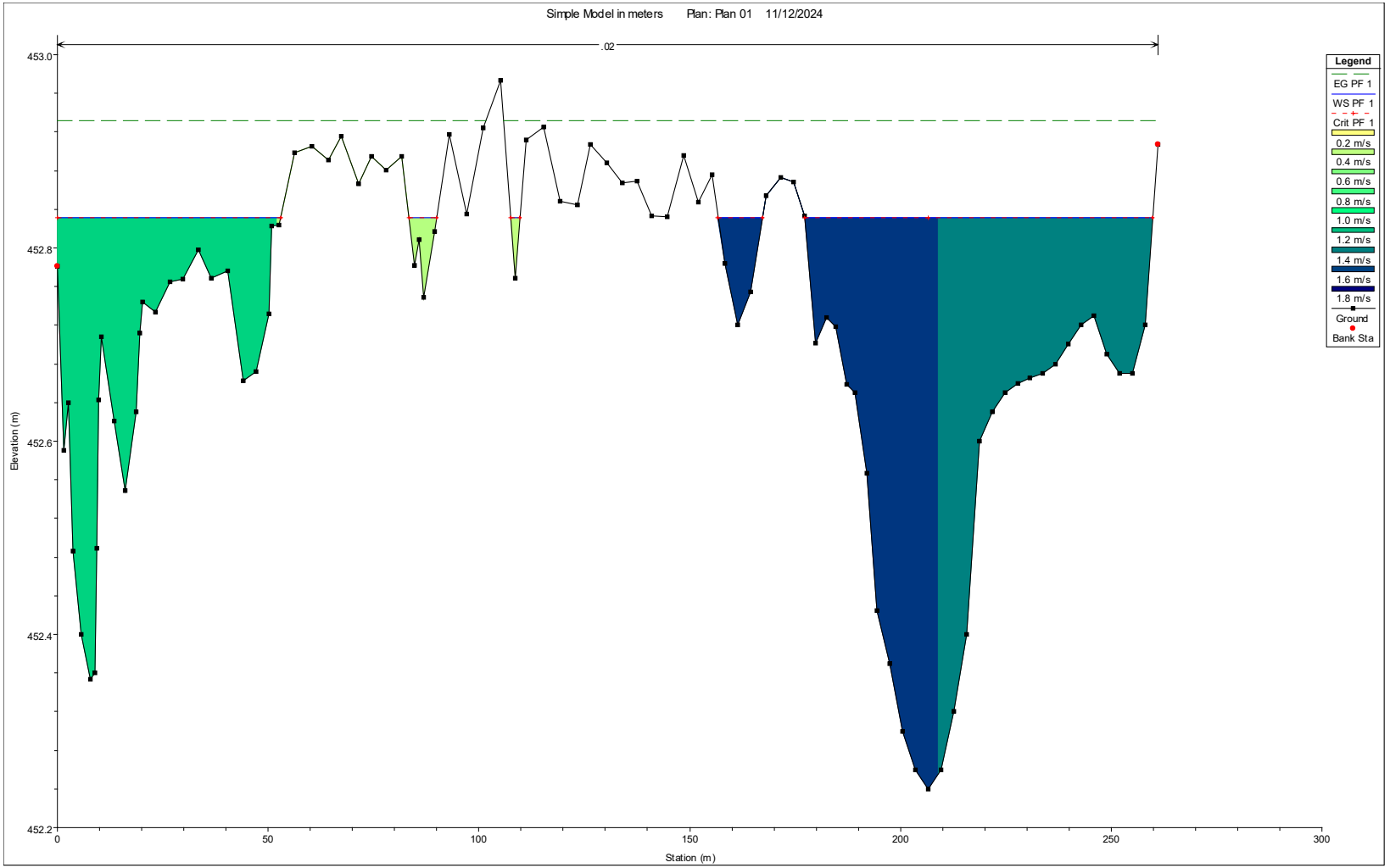

Figure 6.11 Cross-section 3 model result

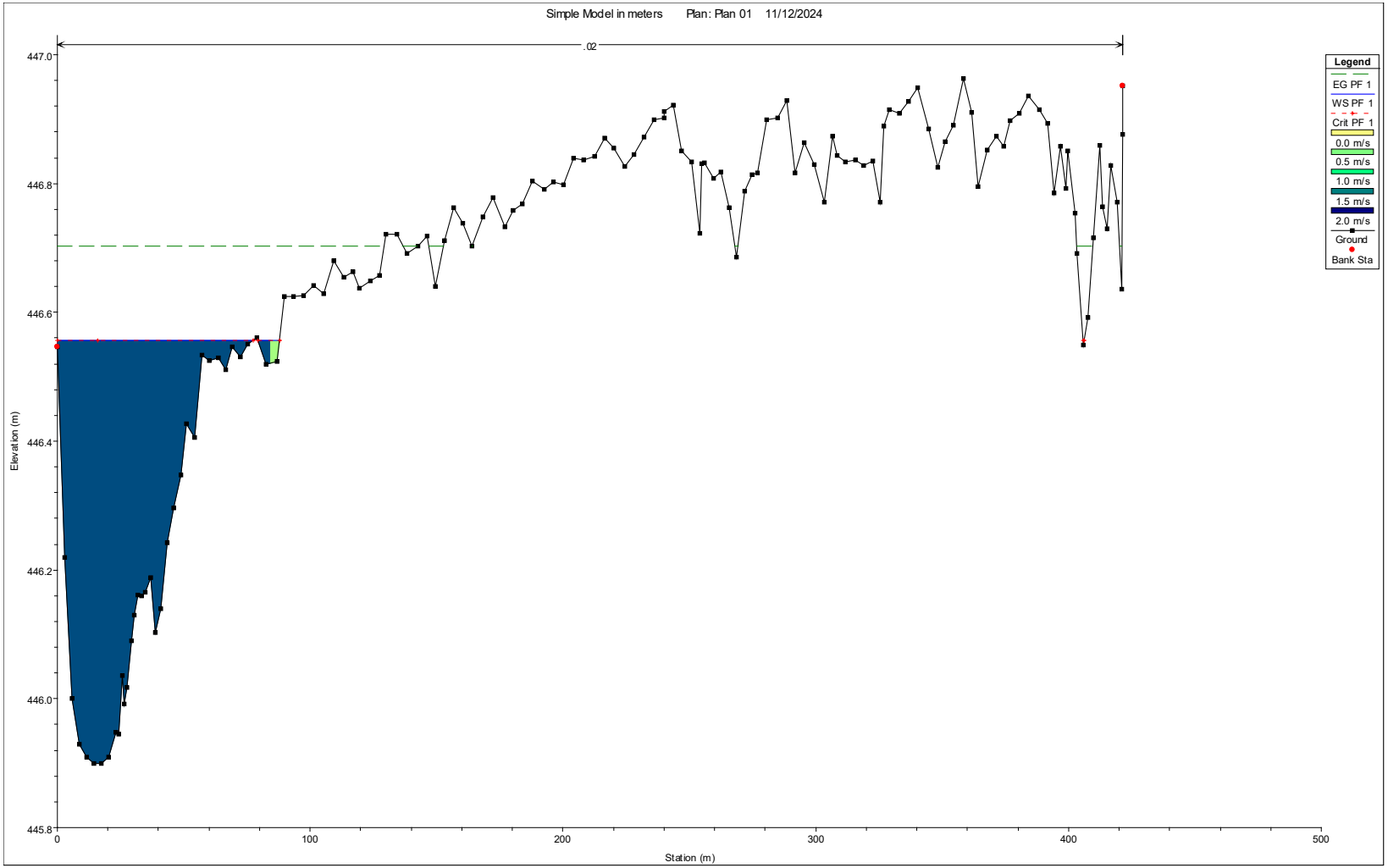

Figure 6.12 Cross-section 5 model result

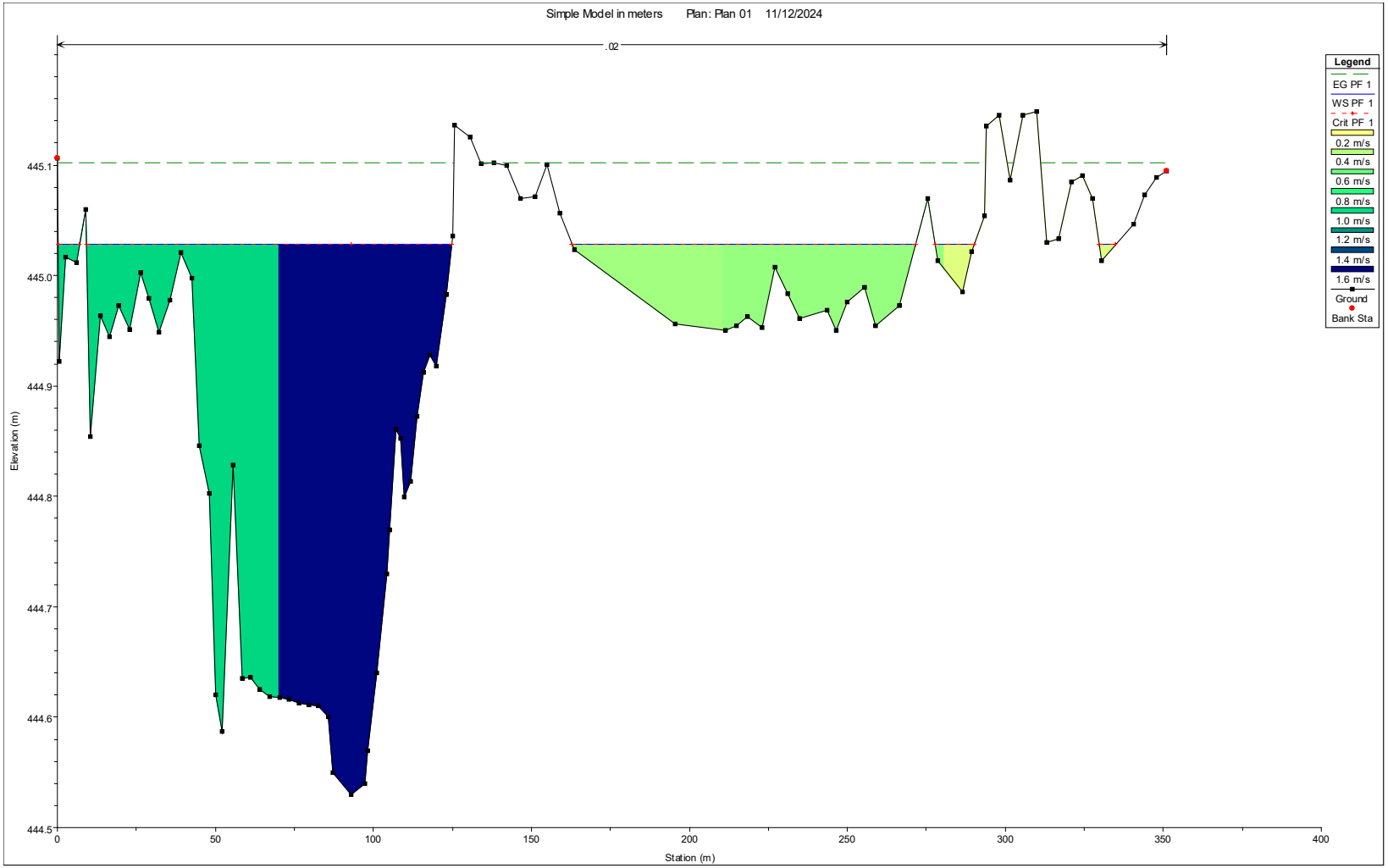

Figure 6.13 Cross-section 6 model result

After setting up a quasi-unsteady model in HEC-RAS to simulate unsteady flow conditions along a river, our plan was to develop a high-quality two-dimensional (2D) model. Unlike the quasi-unsteady model, which primarily focuses on one-dimensional flow, a 2D model would capture both longitudinal and lateral flow components, providing a more detailed representation of floodplain dynamics. By creating a computational grid over the study area and integrating topographic data, the 2D model should better simulate complex hydraulic conditions, including overbank flow and the effects of varying topography, offering a more accurate prediction of flood behavior. A 2-D model was attempted, but a successful model was not completed for this report because of problems accurately identifying bathymetry, and because of difficulty with self-formed channels. The steps for creating the 2D model are discussed in Appendix B.

7. Conclusions

7.1. Conclusions

The Niobrara River had massive ice flows following the 2019 March bomb cyclone and the rapid snowmelt that followed the event. This caused Spencer Dam to fail and the Highway 281 bridge approach to be destroyed. Since the failure of the dam, the river has taken a new course, and the streambed elevations are adjusting, causing changes in the morphology of the river. The overall goal of this project was to better predict short-term and long-term channel migration and aggradation in the vicinity of the Highway 281 bridge. Using the orthomosaics and point clouds that were collected from an unmanned aerial system and hand-collected PPK GPS data, a one-dimensional model was developed to recreate flow conditions in the Niobrara.

An important finding of this research was associated with changes in the longitudinal water surface elevation profile of the Highway 281 and Spencer Dam site. The water surface elevation, starting from the 2020 USGS LiDAR Data, is continually changing. The slope remains relatively the same, but the elevations are increasing over time. This indicates that the sediment from the reservoir is contributing to the adjustment of the bed elevation, thus the water elevation is also adjusted. This finding was helpful for determining the slope of the river in the creation of a hydraulic model.

Another finding from studying the collected orthomosaics is that the river flow condition is critical near the bridge for a large portion of the year. This is determined from the standing waves that are in all aerial orthomosaics. This finding was helpful in the creation of the model because results of the model should display that it is near critical depth for the entire reach. It is more difficult to model critical flows than subcritical flows because of the non-uniformity of the water surface.

This project started with data collection. Collecting thorough and detailed data, especially the photogrammetric and hand-collected PPK GPS data, was key in creating an accurate hydrodynamic model. The hand-collected PPK GPS data that were collected in the fall of 2023 could have been more detailed and exact for determining where the banks were and what the water surface elevations were. Better noting these would have been helpful in determining the actual water surface elevation for certain cross-sections and determining what was above and below the water surface. Nevertheless, the data that were collected were extremely helpful in producing viable flow cross sections, even if it would have been nice to have more of the data.

Another research finding is that the one-dimensional model that was created from implementing the collected data and understanding the river behavior is reasonable. This was determined based on the critical flow of the river and where the water elevation was for each cross-section. The results of the model recreated the same conditions as the fall of 2023. Creating a simple quasi-unsteady sediment-transport model was attempted and did not work due to the complexities of the sand-bed river and the rapid flow velocities observed at the site.

As for obtaining the objectives of this project, a measurement method was established for rapidly collecting detailed topographic and flow data at bridge crossings. The method was used to collect multiple complete data sets at a bridge crossing with dynamic streambed conditions. A hydraulic

modeling approach for predicting short- and long-term morphologic changes at the bridge crossing requires more work. Although a one-dimensional model was created, the model was unable to predict short- and long-term changes in the channel morphology. The predicted results were compared with the observed data, and it concluded the one-dimensional model could reproduce observed flow results accurately. The modeling methods still need to be refined for the application of a more complex hydrodynamic model at the local bridge crossing of the Niobrara River. Although the one-dimensional model is accurate in predicting flow conditions, a more complex model will be needed to predict bank and bedform movements. Not only to predict the bank and bedform movement between observed data but to predict the short- and long-term changes as well.

Finally the quantification of sediment availability volumes is a major result of the project. Calculating the volume loss in specific areas of erosion contributes to understanding the behavior of the river flow and will contribute to predicting short-term and long-term changes in the location of the banks and how much sediment the river has eroded. This information can be used both to understand long-term implications of bed aggradation at the study site, but also for feeding sediment into a future hydrodynamic model.

Based on our observations, we expect the riverbed to continue to aggrade, though at a lower rate than in previous years. This will continue until the sediment deposited in the reservoir is more thoroughly depleted. While not all of the sediment deposits that were determined are readily erodible, large quantities of highly erodible deposits remain in the immediate path of the main channel.

7.2. Recommendations for Further Work

The presented work can serve as a basis for a more complex sediment transport model or two-dimensional model. Understanding the changes of the bed topography at the Niobrara River over time is crucial in creating a simple sediment transport model. If possible, collecting additional PPK GPS data may help in creating a more accurate sediment transport model. More importantly, methods of recreating bathymetry from image data need to be developed to create a model with a wider spatial extent and reasonable depth estimates throughout the study reach.

For creating a two-dimensional model, a digital elevation model that best represents the current conditions of the Niobrara River is needed. Creation of a two-dimensional model will show what is happening across the floodplain rather than just at cross-sections, but only if one can be created that accurately represents the complex sediment transport processes that are happening at the site. A two-dimensional model will likely perform better with the perched channels – especially if high accuracy, detailed bathymetry is available. The model will also help in modelling the erosion at the banks.

These are the steps necessary to complete such a model:

1. Develop an efficient, automated method of converting aerial imagery into reasonably accurate bathymetries at the site.
2. Produce a reasonably accurate estimate of the unsubmerged topography of the sand bedforms above the water surface.

3. Develop a good sediment transport model that reliably predicts the movement of sediment in the river for different depths and velocities. It may not be necessary to predict the development of perched channels and braids, but it is definitely necessary to predict large-scale sediment transport behavior during high flows.
4. Develop a reasonable model for lateral erosion of sediment deposits. This is where the sediment erosion estimate procedures developed in this work are valuable, because the estimates can be used alongside near-bank flow information to understand how sediment is removed during high flows.
5. Embed the models from steps 3 and 4 with the two-dimensional hydrodynamic model, utilizing the bathymetries and topographies from steps 1 and 2 as baseline elevations.

References

Alexander, Jason S.; Zelt, Ronald B.; and Schaepe, Nathaniel J., (2009), "Geomorphic Segmentation, Hydraulic Geometry, and Hydraulic Microhabitats of the Niobrara River, Nebraska—Methods and Initial Results". Publications of the US Geological Survey. 14. https://digitalcommons.unl.edu/usgspubs/14

Baker, M.E., R. Ettema, M. Teal, and J. Trojanowski (2020) Spencer dam failure investigation report, *Association of State Dam Safety Officials (ASDSO)*, Lexington, KY.

Beltaos, S., & Prowse, T. D. (2001). "Climate impacts on extreme ice-jam events in Canadian rivers". *Hydrological Sciences Journal,* **46(1)**, 157–181. https://doi.org/10.1080/02626660109492807

Beltaos, S. (2016). "Extreme sediment pulses during ice breakup, Saint John River, Canada". *Cold Regions Science and Technology*, **128**, 38–46. https://doi.org/10.1016/j.coldregions.2016.05.005

Bridge, J. S. (1993)." The interaction between channel geometry, water flow, sediment transport and deposition in braided rivers". *Geological Society Special Publication*, **16(75)**, 13–71. http://sp.lyellcollection.org/Downloadedfrom

Church, M. (2006). "Bed material transport and the morphology of alluvial river channels". *Annual Review of Earth and Planetary Sciences,* **34(1)**, 325–354. https://doi.org/10.1146/annurev.earth.33.092203.122721

de Almeida, G. A. M., & Rodríguez, J. F. (2011). "Understanding pool-riffle dynamics through continuous morphological simulations". *Water Resources Research*, **47(1)**, 1–15. https://doi.org/10.1029/2010WR009170

Dey, S. (2001). "Bank Profile of Threshold Channels: A Simplified Approach". *Journal of Irrigation and Drainage Engineering*, **127(3)**, 184–187.

Dunne, K. B. J., & Jerolmack, D. J. (2018). "Evidence of, and a proposed explanation for, bimodal transport states in alluvial rivers". *Earth Surface Dynamics*, **6(3)**, 583–594. https://doi.org/10.5194/esurf-6-583-2018

Dunne, K. B. J., & Jerolmack, D. J. (2020). "What sets river width?". *Science Advances*, **6(41)**, 1–8. https://doi.org/10.1126/sciadv.abc1505

Francalanci, S., Lanzoni, S., Solari, L., & Papanicolaou, A. N. (2020). "Equilibrium cross section of river channels with cohesive erodible banks". *Journal of Geophysical Research: Earth Surface*, **125**, e2019JF005286. https://doi.org/10.1029/2019JF005286

Ikeda, S., & Izumi, N. (1991). "Stable Channel Cross Sections of Straight Sand Rivers". *Water Resources Research*, **27(9)**, 2429–2438. https://doi.org/10.1029/91WR01220

Leopold, L. B., & Maddock, T. (1953). "The Hydraulic Geometry of Stream Channels and Some Physiographic Implications".

NAIP, United States Department of Agriculture (2016). 1 meter Orthomosaics. Accessed November 2024. URL https://nrcs.app.box.com/v/naip/folder/18145823705

NAIP, United States Department of Agriculture (2018). 1 meter Orthomosaics. Accessed November 2024.

NAIP, United States Department of Agriculture (2020). 1 meter Orthomosaics. Accessed November 2024. URL https://nrcs.app.box.com/v/naip/folder/125277901693

NAIP, United States Department of Agriculture (2022). 1 meter Orthomosaics. Accessed November 2024. URL https://nrcs.app.box.com/v/naip/folder/178782857252

NAIP, United States Department of Agriculture (2024). 1 meter Orthomosaics. Accessed November 2024. URL https://nrcs.app.box.com/v/naip/folder/178782857252Nebraska Department of Natural Resources (2013) *archived data.*

Parker, G. (1978). "Self-formed straight rivers with equilibrium banks and mobile bed. Part 1. The sand-silt river". *Journal of Fluid Mechanics*, **89(1)**, 109–125.

Popović, P., Devauchelle, O., Abramian, A., & Lajeunesse, E. (2021). "Sediment load determines the shape of rivers". *Proceedings of the National Academy of Sciences*, **118(49)**, 1–11. https://doi.org/10.1073/pnas.2111215118

Randle, T. J., Mohammed, D. W., & Samad, A. (2008). "Platte River in Central Nebraska Modeling of Pulse-Flow Release".

Schaepe, N.J., and Zelt, R.B. (2018), Niobrara River suspended-sediment and bed-sediment data collected during hydroelectric dam flush near Spencer, Nebr., October through November, 2014: U.S. Geological Survey data release, https://doi.org/10.5066/F74M93RK.

Smith, N. (1971). "Transverse Bars and Braiding in the Lower Platte River, Nebraska". *Geological Society of America Bulletin*, **82**, 3407–3420.

Turcotte, B., Morse, B., Bergeron, N. E., & Roy, A. G. (2011). "Sediment transport in ice-affected rivers". *Journal of Hydrology,* **409**, 561-577. https://doi.org/10.1016/j.geomorph.2012.07.019

U.S. Geological Survey. (2021), 3D Elevation Program Lidar Point Cloud (ver. USGS Lidar Point Cloud NE_Niobrara_Topobathy_2018_D18 14TNN2838), accessed August 2022 at URL https://apps.nationalmap.gov/downloader/#/?z=4&y=37.99999999999999&x=-95&basemap=usgs_topo&datasets=&layerIds=

U.S. Geological Survey. (2022), 3D Elevation Program 1-Meter Resolution Digital Elevation Model (ver. USGS 1 Meter 14 x51y475 NE_Northeast_2020_D20), accessed August 2022 at URL https://apps.nationalmap.gov/downloader/#/?z=4&y=37.99999999999999&x=-95&basemap=usgs_topo&datasets=&layerIds=

van Rijn, L. (2007) "Unified View of Sediment Transport by Currents and Waves. I: Initiation of Motion, Bed Roughness, and Bed-Load Transport," *Journal of Hydraulic Engineering*, **133(6)**, Pages 649-667.

Wilson, G. (1973). “Equilibrium Cross-section of Meandering and Braided Rivers”. *Nature*, **241**, 393–394.

Yu, G., & Lim, S. Y. (2003). “Modified Manning formula for flow in alluvial channels with sand-beds”. *Journal of Hydraulic Research*, **41(6)**, 597–608. https://doi.org/10.1080/00221680309506892

Appendix A. Field Site Information

A.1. September 2022 Site Visit Information

Table A.1 Visit 1 Discharges (cfs) at Butte gauge and temperatures (°F) at Verdel

	3 Days Prior		2 Days Prior		1 Day Prior		Site Visit Day	
Time	9/7/2022		9/8/2022		9/9/2022		9/10/2022	
00:00	1032.7	72.9	1083.4	73.4	904.5	72.5	1246.6	N/A
00:15	1032.7	72.7	1049.8	73.4	894.9	72.3	1305.4	N/A
00:30	1017.9	72.3	1049.8	73.2	923.9	72.0	1325.3	N/A
00:45	1032.8	72.3	1006.9	73.0	923.8	71.6	1305.2	N/A
01:00	1032.8	72.0	1066.5	73.0	914.0	71.1	1345.2	N/A
01:15	1032.8	71.8	1049.8	72.9	904.3	70.7	1365.5	N/A
01:30	1049.3	71.6	1006.9	72.7	904.3	70.2	1345.0	N/A
01:45	1049.3	71.4	1017.2	72.7	913.9	69.8	1365.3	N/A
02:00	1066.0	71.2	996.5	72.5	913.9	69.6	1304.7	N/A
02:15	1049.3	71.1	996.5	72.3	913.8	69.3	1304.6	N/A
02:30	1049.3	70.9	1006.8	72.3	913.8	69.1	1344.6	N/A
02:45	1049.3	70.7	1006.8	72.1	913.8	69.1	1284.5	N/A
03:00	1049.3	70.5	1033.3	72.1	894.4	68.9	1304.2	N/A
03:15	1049.3	70.3	1006.8	72.0	904.0	68.5	1304.1	N/A
03:30	1049.3	70.0	996.5	71.8	923.4	68.4	1304.0	N/A
03:45	1066.0	70.0	1006.8	71.8	933.2	68.0	1303.9	N/A
04:00	1066.0	69.8	1006.8	71.6	923.3	67.8	1323.8	N/A
04:15	1049.4	69.8	1006.8	71.6	962.9	67.5	1343.9	N/A
04:30	1066.0	69.8	1033.4	71.4	942.9	67.3	1283.8	N/A
04:45	1049.4	69.6	1066.6	71.4	972.8	67.1	1283.7	N/A
05:00	1049.4	69.6	1100.5	71.4	972.8	66.9	1303.4	N/A
05:15	1066.0	69.4	1049.9	71.4	982.9	66.7	1303.3	N/A
05:30	1049.4	69.3	1017.1	71.2	942.8	66.7	1244.4	N/A
05:45	1082.9	69.3	1017.1	71.2	982.8	66.6	1283.3	N/A
06:00	1082.9	69.1	1017.1	71.2	962.6	66.6	1244.2	N/A
06:15	1082.9	69.1	1033.4	71.1	942.6	66.4	1302.9	N/A
06:30	1099.9	68.9	1017.1	71.1	932.7	66.2	1322.8	N/A
06:45	1099.9	68.9	1017.1	70.9	982.6	66.0	1225.2	N/A
07:00	1082.9	68.7	1066.7	70.9	992.8	65.8	1302.6	N/A
07:15	1082.9	68.5	1006.7	70.7	1003.0	65.5	1263.1	N/A
07:30	1082.9	68.5	1050.0	70.9	992.7	65.3	1282.6	N/A
07:45	1082.9	68.5	1117.8	70.9	982.5	65.3	1243.5	N/A
08:00	1083.0	68.7	1050.0	71.1	992.6	65.3	1282.4	N/A
08:15	1083.0	68.9	1050.0	71.2	1013.1	65.3	1302.1	N/A
08:30	1049.4	69.1	1033.4	71.2	982.4	65.1	1322.0	N/A
08:45	1066.1	69.4	1033.4	71.4	1002.7	64.9	1262.5	N/A
09:00	1083.0	69.8	1006.6	71.8	1027.1	64.9	1321.8	N/A
09:15	1049.5	70.2	1006.6	72.0	1027.0	64.8	1321.7	N/A
09:30	1083.0	70.3	996.3	72.1	1026.9	64.8	1301.6	N/A
09:45	1066.2	70.5	996.3	72.3	1026.9	64.8	1281.7	N/A
10:00	1100.0	70.9	1049.6	72.5	1026.8	64.8	1301.4	N/A
10:15	1117.2	71.2	1016.8	72.7	1026.7	64.6	1321.3	N/A
10:30	1100.0	71.8	1032.9	73.0	1042.9	64.6	1321.2	N/A
10:45	1083.0	72.1	1049.4	73.4	1012.7	64.6	1341.3	N/A
11:00	1100.0	72.5	1066.0	73.6	1012.7	64.6	1341.2	N/A
11:15	1083.0	72.9	1032.7	73.9	1059.1	64.6	1300.9	N/A
11:30	1083.0	73.8	1065.8	74.8	1012.6	64.6	1242.0	N/A
11:45	1100.0	74.8	1032.6	76.1	1012.5	64.4	1261.4	N/A

12:00	1083.1	75.7	1032.5	76.8	1058.9	N/A	1300.6	N/A
12:15	1083.1	76.1	1032.5	77.0	1026.2	N/A	1280.7	N/A
12:30	1100.1	76.3	1082.4	77.0	1058.7	N/A	1300.4	N/A
12:45	1083.1	76.5	1065.5	77.4	1058.7	N/A	1261.0	N/A
13:00	1083.1	76.3	1032.3	77.2	1058.6	N/A	1241.4	N/A
13:15	1066.2	75.9	1048.7	76.8	1058.5	N/A	1300.1	N/A
13:30	1049.6	75.7	1032.1	76.6	1058.5	N/A	1300.0	N/A
13:45	1083.1	75.6	1032.1	76.5	1042.0	N/A	1241.2	N/A
14:00	1066.3	75.6	1016.1	76.5	1012.2	N/A	1260.5	N/A
14:15	1083.1	75.6	1005.8	76.5	1058.3	N/A	1339.8	N/A
14:30	1049.6	75.6	995.5	76.5	1041.8	N/A	1299.6	N/A
14:45	1066.3	75.6	985.2	76.5	1074.6	N/A	1319.5	N/A
15:00	1049.6	75.7	975.1	76.5	1025.5	N/A	1359.9	N/A
15:15	1033.1	75.7	1064.8	76.5	1091.1	N/A	1299.3	N/A
15:30	1033.1	75.7	1015.9	76.6	1091.0	N/A	1221.9	N/A
15:45	1066.3	75.7	1064.6	76.6	1057.8	N/A	1221.9	N/A
16:00	1033.1	75.7	1005.5	76.8	1074.2	N/A	1299.0	N/A
16:15	1049.6	75.9	1081.2	76.8	1107.6	N/A	1221.7	N/A
16:30	1033.1	75.9	995.1	76.8	1090.7	N/A	1259.5	N/A
16:45	1066.3	75.9	984.9	76.8	1025.1	N/A	1259.4	N/A
17:00	1100.2	75.9	974.7	76.8	1073.9	N/A	1278.9	N/A
17:15	1049.7	75.9	974.7	76.8	1158.5	N/A	1239.8	N/A
17:30	1066.3	75.9	974.7	77.0	1090.4	N/A	1221.2	N/A
17:45	1066.4	75.9	1031.0	77.0	1107.1	N/A	1221.1	N/A
18:00	1033.1	75.9	1030.9	77.0	1107.0	N/A	1278.5	N/A
18:15	1017.4	75.9	994.9	77.0	1140.9	N/A	1239.4	N/A
18:30	1066.4	75.9	984.6	77.0	1123.8	N/A	1220.8	N/A
18:45	1033.2	75.9	994.8	77.0	1193.4	N/A	1258.6	N/A
19:00	1017.4	75.7	974.4	76.8	1193.3	N/A	1202.4	N/A
19:15	1007.0	75.7	974.4	76.8	1157.7	N/A	1220.5	N/A
19:30	1007.0	75.6	964.3	76.6	1193.1	N/A	1238.9	N/A
19:45	1007.0	75.4	974.3	76.5	1175.1	N/A	1184.1	N/A
20:00	1017.4	75.2	944.3	76.3	1140.3	N/A	1277.7	N/A
20:15	1033.2	75.2	944.2	76.1	1229.2	N/A	1258.0	N/A
20:30	1049.7	75.0	954.1	76.1	1210.8	N/A	1257.9	N/A
20:45	1049.7	75.0	944.1	76.1	1247.9	N/A	1257.8	N/A
21:00	1017.4	74.8	944.1	76.1	1286.8	N/A	1238.3	N/A
21:15	1007.0	74.8	944.1	75.9	1286.7	N/A	1277.2	N/A
21:30	1017.4	74.7	954.0	75.6	1306.5	N/A	1277.1	N/A
21:45	1033.2	74.5	944.0	75.2	1228.6	N/A	1201.4	N/A
22:00	1049.8	74.5	943.9	74.7	1326.3	N/A	1219.5	N/A
22:15	1066.5	74.3	934.0	74.5	1247.3	N/A	1219.4	N/A
22:30	1049.8	74.1	924.2	73.9	1247.2	N/A	1237.7	N/A
22:45	1017.3	74.1	924.1	73.8	1191.9	N/A	1257.0	N/A
23:00	1006.9	73.9	914.4	73.4	1286.0	N/A	1237.5	N/A
23:15	1049.8	73.8	924.1	73.0	1305.8	N/A	1219.0	N/A
23:30	1033.3	73.8	914.3	72.9	1246.8	N/A	1256.7	N/A
23:45	1033.3	73.6	904.6	72.7	1325.6	N/A	1218.9	N/A

Discharge Flow Data Collected from Nebraska Department of Natural Resources from Niobrara River, Butte Site. https://nednr.aquaticinformatics.net/Data/DataSet/Chart/Location/06464930/DataSet/Discharge/Working/Interval/Custom/2023/06/11/2023/06/15

Water Temperature Data Collected from USGS Water Data at Niobrara River at Verdel NE https://waterdata.usgs.gov/monitoring-location/06465500/#parameterCode=00010&showMedian=false&startDT=2022-09-07&endDT=2022-09-11

Table A.2 Weather at Lynch, Nebraska, September 10, 2022

Date:	9/7/2022	9/8/2022	9/9/2022	9/10/2022
Max. Temperature (°F)	94	92	102	65
Min. Temperature (°F)	55	55	61	48
Precipitation (in)	0	0	0	0.40
Weather Data Collected from NOAA Daily Summaries Station in Lynch, NE https://www.ncdc.noaa.gov/cdo-web/datasets/GHCND/stations/GHCND:USC00255040/detail				

Table A.3 Weather at O'Neill, Nebraska, September 10, 2022

Date:	9/7/2022	9/8/2022	9/9/2022	9/10/2022
Max. Temperature (°F)	91	99	70	71
Min. Temperature (°F)	57	68	55	49
Precipitation (in)	0	0	0	0.45
Weather Collected from The O'Neill Municipal John L Baker Field Station https://www.wunderground.com/history/daily/us/ne/oneill/KONL/date/2022-9-10				

A.2. March 2023 Site Visit Information

Table A.4 Visit 2 Discharges (cfs) at Butte gauge and temperatures (°F) at Verdel

	3 Days Prior		2 Days Prior		1 Day Prior		Site Visit Day	
Time	3/17/2023		3/18/2023		3/19/2023		3/20/2023	
00:00	4624.0		3401.7		3607.5		3224.4	
00:15	4496.2		3371.4		3514.8		3209.9	
00:30	4591.4		3356.3		3588.2		3138.3	
00:45	4464.2		3356.2		3588.1		3138.3	
01:00	4401.3		3356.1		3499.2		3067.7	
01:15	4339.1		3341.0		3531.2		2984.3	
01:30	4308.1		3281.3		3587.7		2984.3	
01:45	4307.8		3251.7		3483.6		2917.0	
02:00	4431.6		3178.4		3498.8		2916.9	
02:15	4246.2		3163.9		3453.1		2997.9	
02:30	4431.1		3163.8		3468.1		2943.3	
02:45	4399.6		3222.0		3422.7		2877.4	
03:00	4185.0		3178.2		3377.5		2825.3	
03:15	4154.7		3163.6		3347.6		2812.3	
03:30	4398.9		3221.8		3317.9		2799.4	
03:45	4305.9		3251.1		3288.3		2735.4	
04:00	4154.0		3265.8		3362.3		2710.1	
04:15	4183.8		3236.3		3332.5		2864.1	
04:30	4093.9		3221.6		3302.8		2916.6	
04:45	4123.4		3250.8		3244.1		2864.1	
05:00	4034.4		3295.1		3214.9		2838.0	
05:15	4093.2		3236.0		3214.9		2903.3	
05:30	3946.4		3235.9		3229.3		2786.3	
05:45	4033.7		3206.6		3436.7		2837.9	
06:00	4033.5		3177.4		3451.7		2799.1	
06:15	3945.8		3134.0		3391.4		2824.9	
06:30	3945.5		3090.9		3317.0		2863.9	
06:45	3974.3		3062.4		3451.4		2786.2	
07:00	3916.2		3076.6		3436.2		2903.1	
07:15	3944.8		3034.0		3376.1		3010.8	
07:30	4032.1		3019.9		3346.3		3024.6	
07:45	3944.4		2950.2		3316.6		3080.3	
08:00	4002.3		2896.5		3316.5		2955.8	
08:15	4060.8		2923.2		3301.7		2863.6	
08:30	4031.1		2923.1		3228.5		2811.8	
08:45	4060.3		2963.7		3331.1		2889.7	
09:00	3865.3		2923.1		3345.8		2747.7	
09:15	3885.4		2883.0		3330.9		2798.8	
09:30	3865.0		2869.7		3170.5		2747.7	
09:45	3885.1		2856.4		3199.2		2876.5	
10:00	3824.4		2816.9		3156.0		2863.4	
10:15	3844.4		2869.6		3141.7		2785.9	
10:30	3824.1		2843.1		3170.2		2734.9	
10:45	3803.9		2829.9		3127.3		2659.5	
11:00	3763.9		2869.5		3028.5		2722.2	
11:15	3783.7		2896.0		3042.5		2889.4	
11:30	3803.5		2896.0		2972.9		2863.2	
11:45	3783.4		2829.8		2945.6		2837.3	

12:00	3803.2		2991.0		2919.0		2811.4	
12:15	3783.1		2856.1		2986.6		2709.5	
12:30	3822.9		2882.5		2918.9		2524.4	
12:45	3762.9		2963.0		2918.9		2709.5	
13:00	3703.6		2909.1		2879.2		2902.2	
13:15	3703.4		2922.4		2879.2		2954.9	
13:30	3723.0		2935.8		2892.3		2915.3	
13:45	3722.8		2909.0		2945.3		2863.0	
14:00	3683.4		2869.1		3000.1		2889.0	
14:15	3702.9		2869.0		3000.1		2889.0	
14:30	3605.6		2869.0		2945.2		2954.7	
14:45	3644.1		2895.5		3140.6		2862.8	
15:00	3528.8		2922.1		3154.8		2811.1	
15:15	3547.7		2895.4		3241.2		2811.1	
15:30	3624.3		2855.7		3241.1		2862.8	
15:45	3512.0		2882.1		3168.9		2875.7	
16:00	3566.4		2868.8		3212.0		3023.0	
16:15	3511.8		2895.3		3255.5		3064.6	
16:30	3682.1		2868.7		3255.4		3120.6	
16:45	3623.7		2803.1		3387.9		3106.4	
17:00	3681.8		2829.2		3675.1		3234.3	
17:15	3584.9		2855.4		3508.3		3248.6	
17:30	3701.1		2855.4		3493.0		3234.1	
17:45	3661.9		2935.1		3579.6		3022.7	
18:00	3720.4		2962.1		3477.6		3022.7	
18:15	3584.4		3017.8		3387.4		3008.8	
18:30	3584.3		3045.8		3387.3		2862.4	
18:45	3565.0		3102.4		3387.3		2954.1	
19:00	3526.9		3074.0		3462.2		3120.0	
19:15	3495.2		3116.6		3541.3		3364.5	
19:30	3622.2		3470.7		3541.2		3162.3	
19:45	3622.1		3516.5		3597.5		3008.6	
20:00	3602.7		3485.8		3578.5		3008.5	
20:15	3621.8		3470.4		3769.9		2901.3	
20:30	3583.3		3409.7		3476.7		2940.6	
20:45	3778.0		3439.9		3491.8		2536.5	
21:00	3640.8		3470.2		3461.4		2500.4	
21:15	3777.7		3500.6		3506.8		2378.4	
21:30	3659.9		3500.5		3506.7		2609.5	
21:45	3698.7		3515.7		3506.6		2524.4	
22:00	3640.2		3570.5		3446.0		2646.5	
22:15	3640.1		3704.6		3461.0		2759.3	
22:30	3525.2		3763.0		3430.8		2874.9	
22:45	3601.3		3762.8		3326.8		2994.3	
23:00	3525.0		3608.0		3356.2		3063.3	
23:15	3478.2		3551.0		3356.1		3063.2	
23:30	3417.0		3588.7		3370.8		3035.5	
23:45	3432.2		3550.8		3311.8		2966.8	

Discharge Flow Data Collected from Nebraska Department of Natural Resources from Niobrara River, Butte Site.
https://nednr.aquaticinformatics.net/Data/DataSet/Chart/Location/06464930/DataSet/Discharge/Working/Interval/Custom/2023/06/11/2023/06/15

Water Temperature Data Collected from USGS Water Data at Niobrara River at Verdel NE
https://waterdata.usgs.gov/monitoring-location/06465500/#parameterCode=00010&showMedian=false&startDT=2022-09-07&endDT=2022-09-11

Table A.5 Weather at Lynch, Nebraska, March 20, 2023

Date:	3/17/2023	3/18/2023	3/19/2023	3/20/2023
Max. Temperature (°F)	N/A	35	27	57
Min. Temperature (°F)	N/A	4	5	16
Precipitation (in)	N/A	0.03	0	0
Weather Data Collected from NOAA Daily Summaries Station in Lynch, NE https://www.ncdc.noaa.gov/cdo-web/datasets/GHCND/stations/GHCND:USC00255040/detail				

Table A.6 Weather at O'Neill, Nebraska, March 20, 2023

Date:	3/17/2023	3/18/2023	3/19/2023	3/20/2023
Max. Temperature (°F)	32	24	56	38
Min. Temperature (°F)	14	10	13	22
Precipitation (in)	0	0	0	0
Weather Collected from The O'Neill Municipal John L Baker Field Station https://www.wunderground.com/history/daily/us/ne/oneill/KONL/date/2022-9-10				

A.3. August 2023 Site Visit Information

Table A.7 Visit 3 Discharges (cfs) at Butte gauge and temperatures (°F) at Verdel

	2 Days Prior		1 Day Prior		HW11 Visit		HW281 Visit	
Time	8/27/2023		8/28/2023		8/29/2023		8/30/2023	
00:00	1440.8	N/A	1464.4	77.0	1336.2	77.5	1450.4	76.1
00:15	1456.0	N/A	1464.3	77.0	1350.9	77.4	1450.3	75.9
00:30	1440.6	N/A	1464.2	76.8	1350.8	77.0	1434.7	75.7
00:45	1425.4	N/A	1479.7	76.6	1410.9	76.8	1434.6	75.4
01:00	1425.3	N/A	1479.6	76.5	1395.7	76.6	1434.6	75.2
01:15	1440.4	N/A	1464.0	76.3	1426.1	76.3	1450.1	75.0
01:30	1455.6	N/A	1479.5	75.9	1410.7	76.1	1450.0	74.7
01:45	1425.1	73.4	1463.8	75.7	1395.4	75.9	1481.3	74.5
02:00	1440.2	73.0	1479.3	75.6	1395.4	75.6	1449.8	74.3
02:15	1440.1	72.9	1479.2	75.4	1441.2	75.4	1449.8	73.9
02:30	1455.3	72.7	1463.6	75.2	1380.1	75.2	1465.4	73.8
02:45	1470.6	72.3	1463.5	75.0	1365.0	75.0	1465.3	73.6
03:00	1470.6	72.1	1463.5	74.8	1365.0	74.7	1449.6	73.2
03:15	1455.1	72.0	1463.4	74.7	1364.9	74.5	1449.5	73.0
03:30	1470.4	71.6	1463.3	74.5	1335.1	74.3	1433.9	72.9
03:45	1470.3	71.4	1463.3	74.3	1379.7	74.1	1480.8	72.7
04:00	1470.3	71.2	1478.7	74.3	1364.7	73.8	1464.9	72.3
04:15	1454.8	71.1	1478.7	74.1	1364.6	73.6	1496.5	72.1
04:30	1454.7	70.9	1478.6	73.9	1334.8	73.4	1496.4	72.0
04:45	1454.6	70.7	1463.0	73.8	1349.5	73.2	1496.4	71.8
05:00	1454.6	70.5	1478.4	73.6	1349.5	73.0	1449.0	71.6
05:15	1454.5	70.3	1478.4	73.4	1349.4	72.9	1464.6	71.2
05:30	1485.3	70.2	1478.3	73.2	1349.3	72.7	1464.5	71.1
05:45	1485.3	70.0	1462.7	73.0	1364.1	72.5	1496.1	70.9
06:00	1485.2	69.8	1462.6	72.9	1334.4	72.3	1480.1	70.7
06:15	1485.1	69.4	1462.5	72.7	1349.1	72.0	1480.1	70.5
06:30	1485.0	69.3	1478.0	72.7	1319.5	71.8	1495.9	70.3
06:45	1469.5	69.1	1462.4	72.3	1319.4	71.6	1479.9	70.2
07:00	1500.5	68.9	1462.3	72.3	1319.4	71.4	1464.1	69.8
07:15	1500.4	68.7	1462.2	72.1	1319.3	71.2	1495.7	69.6
07:30	1500.3	68.5	1477.7	72.0	1333.9	71.1	1495.6	69.4
07:45	1516.0	68.4	1462.1	72.0	1333.8	70.9	1511.5	69.3
08:00	1500.2	68.2	1477.6	72.0	1363.5	70.9	1479.6	69.3
08:15	1515.8	68.2	1477.5	72.0	1363.4	70.9	1495.4	69.1
08:30	1500.1	68.2	1477.4	72.0	1378.3	70.9	1495.3	69.1
08:45	1531.5	68.2	1461.8	72.0	1363.2	70.9	1495.3	69.3
09:00	1531.4	68.4	1477.3	72.0	1408.5	70.9	1479.3	69.3
09:15	1531.4	68.5	1477.2	72.1	1423.7	71.1	1495.1	69.4
09:30	1531.3	68.9	1477.1	72.3	1408.3	71.2	1527.1	69.6
09:45	1515.4	69.3	1461.5	72.5	1408.3	71.4	1495.0	69.8
10:00	1515.3	69.6	1477.0	72.7	1438.9	71.8	1527.0	70.2
10:15	1499.5	70.0	1476.9	73.0	1438.8	72.1	1526.9	70.5
10:30	1531.0	70.5	1492.5	73.4	1408.0	72.7	1543.1	70.9
10:45	1499.4	71.1	1476.8	73.9	1408.0	73.2	1526.8	71.2
11:00	1530.9	71.8	1476.7	74.5	1438.6	73.8	1542.9	71.8
11:15	1499.3	72.3	1476.6	75.2	1438.6	74.3	1526.7	72.3
11:30	1483.6	73.0	1492.2	75.9	1407.7	74.8	1526.6	72.9
11:45	1468.0	73.8	1492.2	76.6	1438.4	75.4	1526.5	73.4

12:00	1437.2	74.5	1507.9	77.4	1438.3	75.9	1510.3	73.9
12:15	1483.3	75.0	1476.3	78.3	1422.8	76.5	1510.3	74.5
12:30	1483.3	75.7	1491.9	79.0	1422.8	77.0	1494.2	75.2
12:45	1467.7	76.5	1491.9	79.7	1438.1	77.7	1510.1	75.7
13:00	1467.6	77.2	1491.8	80.4	1438.0	78.3	1526.2	76.5
13:15	1452.1	77.9	1491.7	81.0	1438.0	78.8	1542.3	77.0
13:30	1436.7	78.6	1476.0	81.7	1437.9	79.3	1542.2	77.7
13:45	1467.4	79.2	1491.6	82.0	1407.1	79.7	1542.2	78.3
14:00	1436.6	79.9	1460.2	82.6	1437.8	80.1	1525.9	78.8
14:15	1421.3	80.4	1460.2	82.9	1437.7	80.6	1525.8	79.3
14:30	1421.2	81.0	1444.6	83.7	1437.6	81.1	1509.7	79.9
14:45	1421.1	81.3	1444.6	84.0	1453.1	81.5	1509.6	80.4
15:00	1451.6	81.9	1444.5	84.2	1437.5	81.9	1509.5	81.0
15:15	1421.0	82.4	1475.5	84.6	1452.9	82.0	1493.4	81.3
15:30	1420.9	82.8	1413.7	84.9	1452.9	82.4	1509.4	81.7
15:45	1420.8	82.9	1428.9	85.3	1421.8	82.8	1493.3	81.9
16:00	1405.6	83.1	1428.8	85.6	1421.7	82.9	1493.2	82.2
16:15	1420.7	83.5	1428.7	85.6	1421.7	83.1	1509.2	82.2
16:30	1405.5	83.7	1398.2	85.6	1421.6	83.1	1493.1	82.4
16:45	1405.4	83.8	1413.3	85.3	1391.0	83.1	1477.1	82.4
17:00	1420.4	84.2	1413.2	84.9	1406.1	83.1	1477.1	82.4
17:15	1405.2	84.2	1413.2	84.4	1406.1	83.1	1477.0	82.6
17:30	1390.1	84.4	1413.1	84.2	1390.7	82.9	1461.1	82.4
17:45	1390.0	84.4	1397.8	84.0	1405.9	82.8	1476.8	82.4
18:00	1405.0	84.2	1352.8	83.8	1405.8	82.6	1476.8	82.0
18:15	1404.9	84.2	1412.9	83.7	1390.5	82.4	1445.2	81.9
18:30	1420.0	84.0	1397.6	83.3	1390.5	82.0	1445.1	81.5
18:45	1419.9	83.8	1397.5	82.8	1405.6	81.7	1460.8	81.3
19:00	1419.8	83.5	1382.4	82.4	1420.9	81.3	1460.7	81.0
19:15	1419.8	83.1	1367.3	82.4	1405.5	81.1	1429.3	80.6
19:30	1389.5	82.8	1367.2	82.2	1420.7	81.0	1460.6	80.4
19:45	1389.4	82.4	1308.2	81.9	1420.7	80.6	1444.8	80.1
20:00	1404.4	82.0	1352.2	81.7	1405.2	80.4	1444.7	79.7
20:15	1419.5	81.7	1352.1	81.3	1405.2	80.1	1444.6	79.3
20:30	1404.2	81.3	1352.1	81.1	1405.1	79.9	1444.6	79.0
20:45	1389.1	80.8	1352.0	81.0	1405.0	79.5	1444.5	78.6
21:00	1389.1	80.4	1351.9	80.6	1404.9	79.2	1444.4	78.3
21:15	1419.1	80.1	1337.0	80.2	1389.6	79.0	1444.4	77.9
21:30	1419.1	79.7	1337.0	80.1	1389.6	78.6	1444.3	77.5
21:45	1419.0	79.3	1336.9	79.7	1404.7	78.3	1428.6	77.4
22:00	1418.9	79.0	1336.8	79.5	1420.0	78.1	1397.7	77.0
22:15	1418.8	78.8	1411.7	79.2	1435.4	77.9	1459.8	76.6
22:30	1434.0	78.4	1396.4	79.0	1435.3	77.5	1428.4	76.3
22:45	1433.9	78.3	1381.2	78.8	1404.4	77.4	1443.9	76.1
23:00	1449.2	77.9	1366.2	78.4	1404.4	77.0	1412.8	75.7
23:15	1449.1	77.7	1321.7	78.3	1404.3	76.8	1459.5	75.6
23:30	1449.1	77.5	1321.7	78.1	1419.6	76.6	1475.2	75.2
23:45	1464.4	77.4	1351.1	77.9	1450.5	76.3	1507.1	74.8

Discharge Flow Data Collected from Nebraska Department of Natural Resources from Niobrara River, Butte Site.
https://nednr.aquaticinformatics.net/Data/DataSet/Chart/Location/06464930/DataSet/Discharge/Working/Interval/Custom/2023/06/11/2023/06/15

Water Temperature Data Collected from USGS Water Data at Niobrara River at Verdel NE
https://waterdata.usgs.gov/monitoring-location/06465500/#parameterCode=00010&showMedian=false&startDT=2022-09-07&endDT=2022-09-11

Table A.8 Weather at Lynch, Nebraska, August 30, 2023

Date:	8/27/2023	8/28/2023	8/29/2023	8/30/2023
Max. Temperature (°F)	78	88	92	89
Min. Temperature (°F)	48	48	55	52
Precipitation (in)	0	0	0	0
Weather Data Collected from NOAA Daily Summaries Station in Lynch, NE https://www.ncdc.noaa.gov/cdo-web/datasets/GHCND/stations/GHCND:USC00255040/detail				

Table A.9 Weather at O'Neill, Nebraska, August 30, 2023

Date:	8/27/2023	8/28/2023	8/29/2023	8/30/2023
Max. Temperature (°F)	85	87	85	88
Min. Temperature (°F)	50	61	57	53
Precipitation (in)	0	0	0	0
Weather Collected from The O'Neill Municipal John L Baker Field Station https://www.wunderground.com/history/daily/us/ne/oneill/KONL/date/2022-9-10				

A.4. Sediment Graphs – Data from Schaepe et al. (2018)

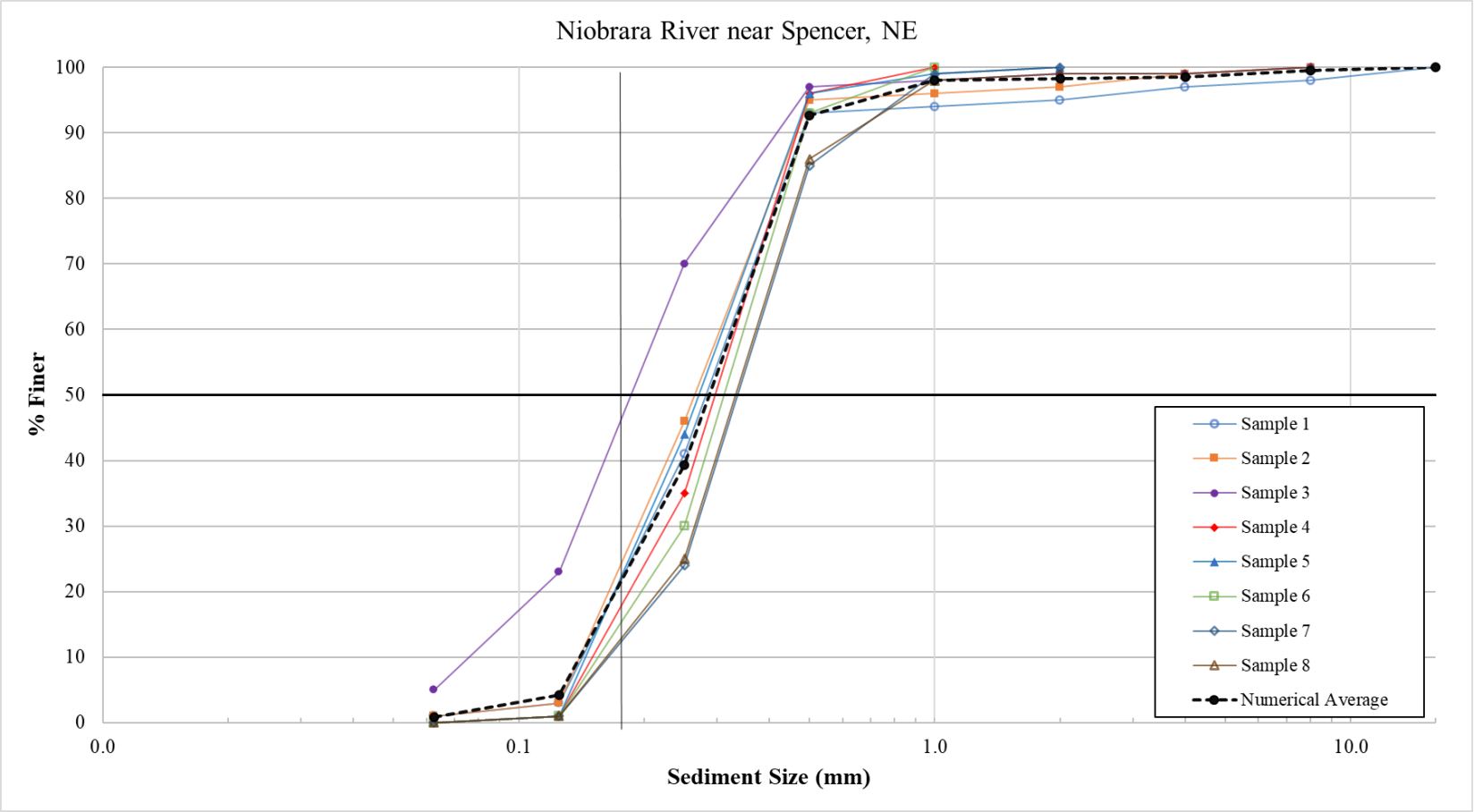

Figure A.1 Sediment Graph for Niobrara River near Spencer, Nebraska

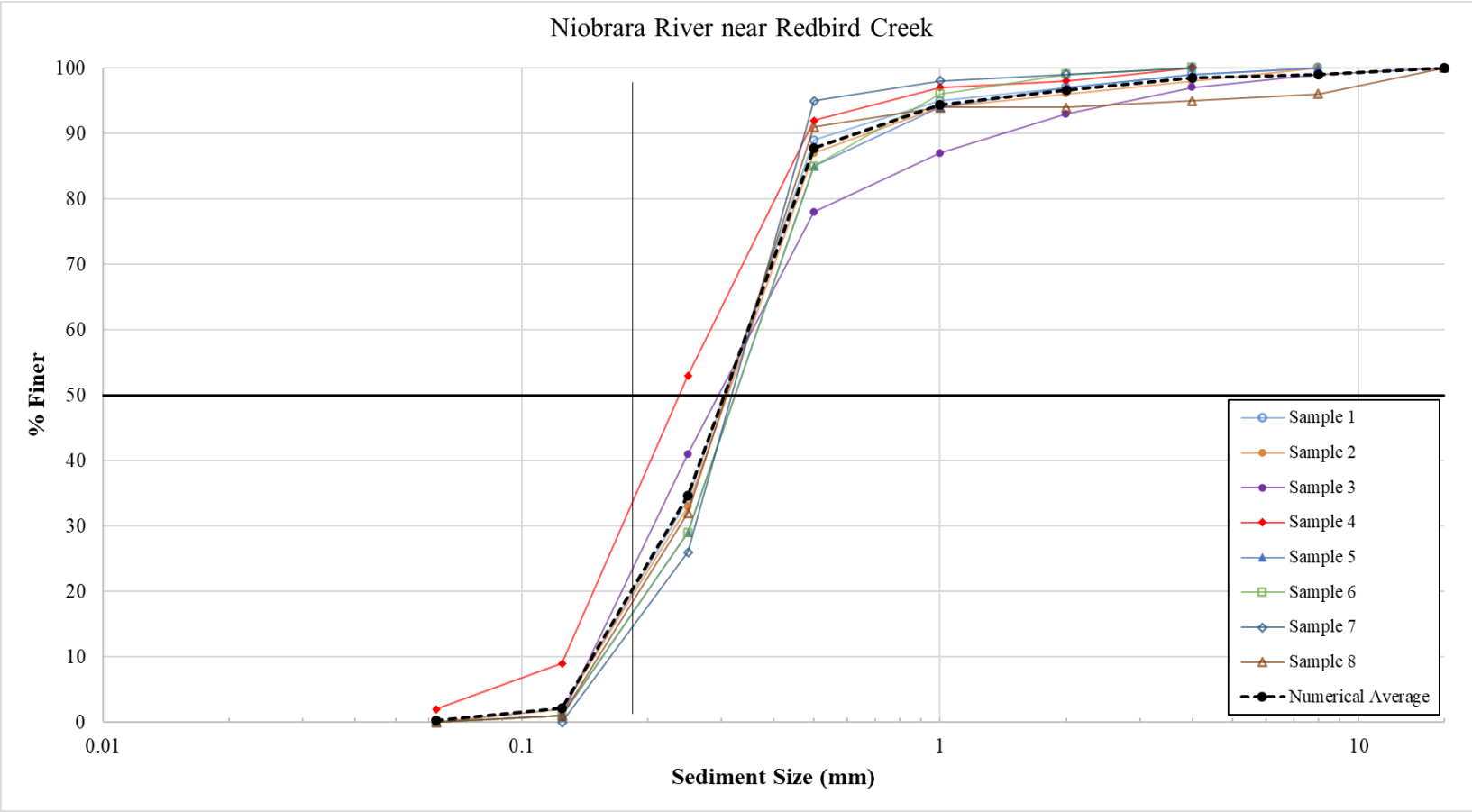

Figure A.2 Sediment Graph for Niobrara River near Redbird Creek

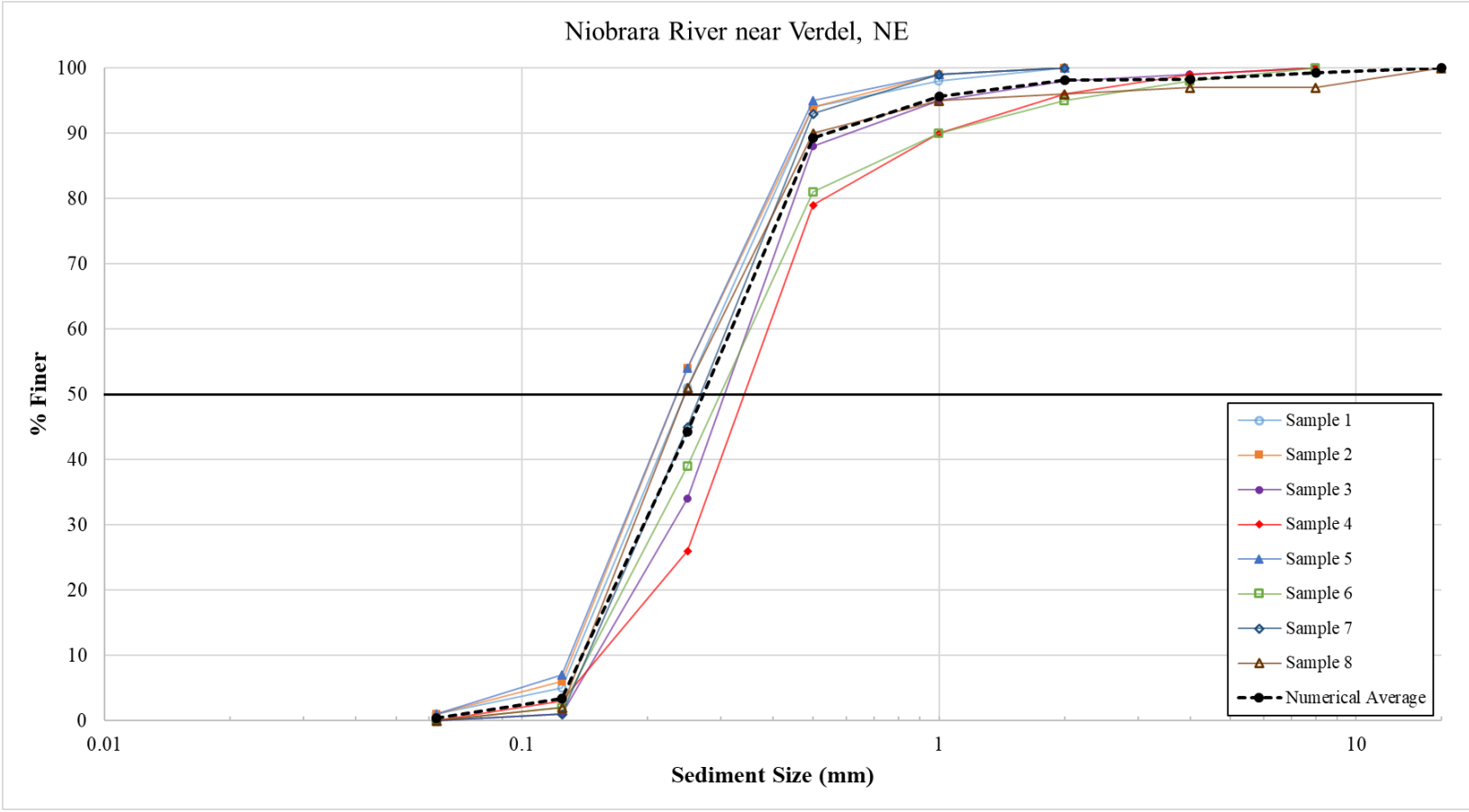

Figure A.3 Sediment Graph for Niobrara River near Verdel, Nebraska

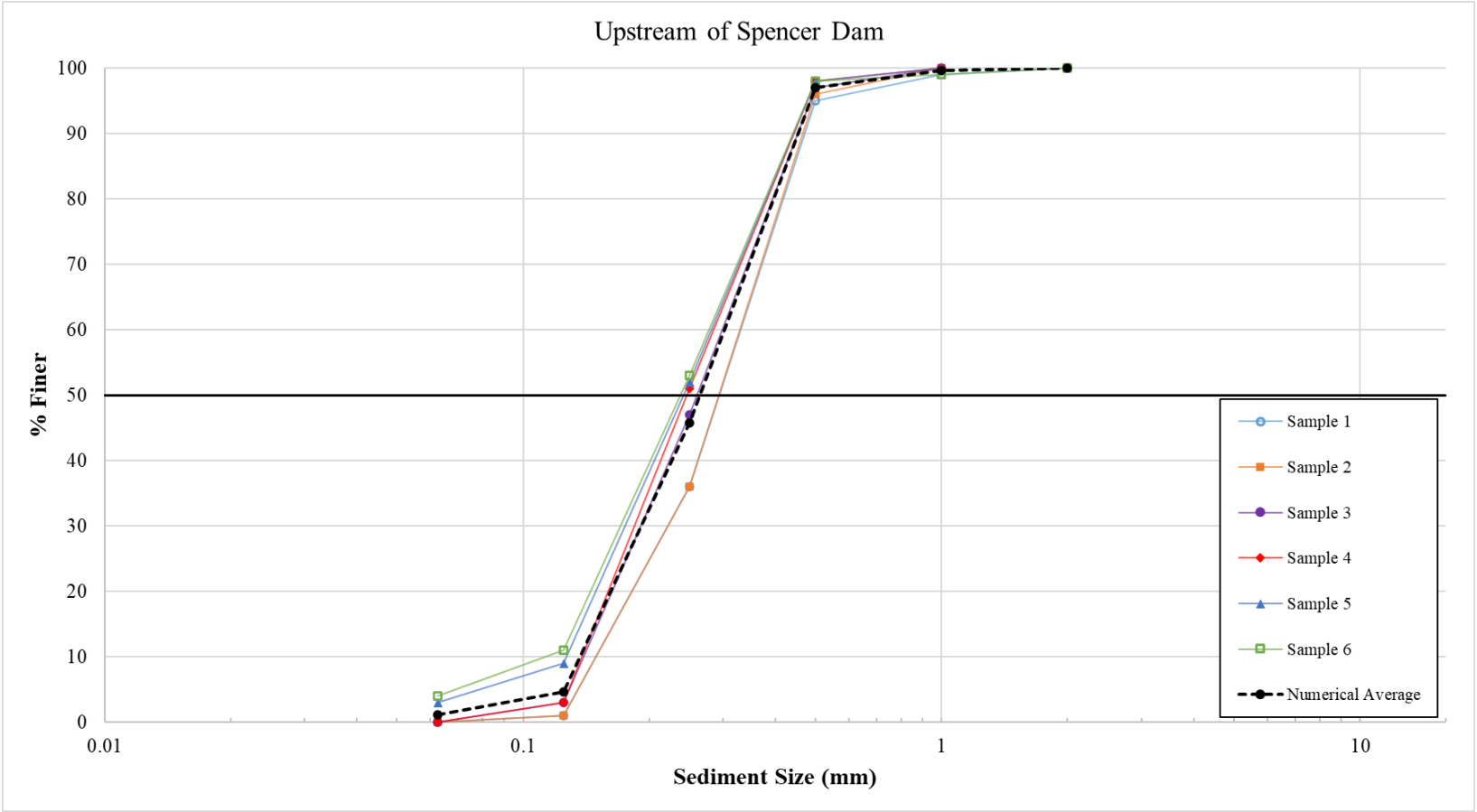

Figure A.4 Sediment Graph for Niobrara River upstream of Spencer Dam

Appendix B. Two-Dimensional Computer Models

A brief discussion of two-dimensional modeling is warranted for future analysis at the study site. To start creating a two-dimensional model, a two-dimensional geometry must be created first. To do this, the *Geometry Editor* is opened and *2D Flow Area* in the Tools row at the top of the window is selected. To create a 2D mesh, the river and river basin are selected by clicking on points surrounding the area of interest. At the last point of the mesh area, the map is double-clicked and the mesh area is saved. Then *BC Lines* is selected in the Tools row of the *Geometry Editor* and two boundary condition lines are added (inflow and outflow). The inflow boundary condition must be inside the mesh and at the area where the flow enters, and the outflow boundary condition must be outside of the mesh and where the flow exits. Once the mesh and the boundary condition lines are created, the 2D Flow Area on the left-hand side under the Editors column is selected. A default Manning's n is entered for the entire mesh. For any area where the Manning's n is not defined, the program will use the default. A Manning's n of 0.02 was used for the one-dimensional model and is also a good starting point for the two-dimensional model. This was determined by the range of Manning's n values that were observed in previous Platte River models. The next step is to select *Generate Computation Points on Regular Interval with Breaklines* and a small window requests the mesh spacing. Since the study area at Spencer Dam is relatively small, a mesh spacing of about 5m for both DX and DY may be appropriate. More cells mean longer run times, but the higher resolutions are beneficial for sediment transport calculations.

The geometry file is then saved and RAS Mapper is opened. The 2D Geometry Tree and the 2D Flow Areas are opened, and the Breaklines tab is selected and the geometry edited. Breaklines are created in RAS Mapper because it is easier to see the river and the banks are much easier to identify than in the Geometry Editor. Breaklines are created with a left click and ended with a double left click. The first breakline is the centerline or known thalweg of the channel. The right and left descending banks are the next two breaklines. Once these lines are made, the geometry is saved and the breaklines tab is again right-clicked. *Edit Breakline Properties* is selected and a small window opened, allowing the breakline spacing to be set. The breakline spacing for the current project was set to 2.5 meters, which is half of the mesh spacing. The near repeat for the centerline is 0 because the goal is just to help direct the flow during model runs. For bank lines, 3 Near Repeats was selected in our preliminary tests. The far spacing for all three was the same as the spacing for the mesh, or 5 meters. Then the changes are accepted and the *Breaklines* tab is pressed again followed by *Enforce Breaklines*. Then the geometry file is saved. The *Geometry Data* should be opened to see if there are any mesh errors indicated by red circles in the mesh. The red circles indicate if computed cells have 8 or more sides. Under the Edit tab in the upper left corner, points are added inside the cells with mesh errors to help eliminate the errors. Once all mesh errors are eliminated the file can be saved. A computation of the cells in the 2D Flow Area Editor might be needed once the geometry is finished.

Finally, unsteady flow data are added. Unsteady flow data in a 2D model simulates time-varying conditions, which is important for modelling real-world river behavior. In this case, unsteady flow data are used to model time-varying flow conditions and complex sediment transport in the

river and across the flood plain. Under the Edit tab on the home window, *Unsteady Flow Data* is selected. This is where the boundary conditions and initial conditions are set. The 2D unsteady flow is very unstable. To make sure it is stable, a constant flow is run through the model first to see if there is any flickering of the "flow" cells where it should be unchanging across the flow area. For the inflow boundary condition, the flow hydrograph is selected (this is the only option for the inflow boundary condition). A time interval of 15 minutes is selected to match the hydrograph data and a Fixed Start Date of August 30, 2023 is chosen. A constant flow of 1500 cubic feet per second can be entered as a starting flow. For a constant flow, the energy grade line slope and the channel slope are the same. The EG slope along the Boundary Condition Line is calculated using the *Measure Distance* tool in RAS Mapper, drawing a line across the outflow and using the slope. For the outflow boundary condition, *Normal Depth* is selected and the same slope from the EG slope is used. The slope for the model is 0.0012. The *Unsteady Flow Data* file is then saved.

Before running the unsteady analysis in our preliminary tests, RAS Mapper was opened and the 2D Geometry tree was opened. 2D Flow Areas was right-clicked and "Compute 2D Flow Areas Hydraulic Tables" was selected. Once finished, the *Unsteady Flow Analysis* option under the Run tab on the home window was selected. The 2D Geometry file was selected and the Unsteady Flow Data file was selected. The programs to run included *Geometry Preprocessor*, *Unsteady Flow Simulation*, *Post Processor*, and *Floodplain Mapping*. The computation interval for the model was 15 seconds. The mapping output interval, detailed output interval, and Hydrograph output interval were all 15 minutes. Then the model was run. The model results could be accessed in the RAS Mapper under "Results". Depth, Velocity, and WSE outputs could be observed. By selecting one of these options and the gradient legend next to it, temporal changes in the output could be reviewed. We could also adjust the model by adjusting the Flow Hydrograph in the Unsteady Flow Analysis data. The modeling procedure ended at this stage because bathymetry data for submerged parts of the river channels were limited, and there were difficulties with modeling the self-formed channels in the active alluvial areas of the floodplain.

Appendix C. National Agricultural Inventory Program Results

Table C.1 NAIP Aerial imagery information for Boyd County

Year	***Data Type***	***Source***	***Image Dates/Times***	***Estimated Discharge (ft^3/s)***	***Description***
2018	Aerial Imagery (0.6-meter resolution)	USDA NAIP (USDA, 2018)	9/12/18 15:38-15:55 9/12/18 15:00-15:17 9/26/18 14:40-14:57 10/03/18 11:43-12:01	1470-1720 1470-1720 1570-1790 1540-1840	Data collected in 5km-wide vertical swathes. Collection dates and times are provided for 10km upstream and downstream of HW281. Discharge estimates are provided for these times based on the range of discharges (minimum to maximum) of the previous and current date.
2020	Aerial Imagery (0.6-meter resolution)	USDA NAIP (USDA, 2020)	7/27/20 12:19-12:33 7/27/20 12:36-12:52 7/27/20 12:55-13:09	1370-1770 1370-1770 1370-1770	Data collected in 7km-wide vertical swathes. Collection dates and times provided for 10km upstream and downstream of HW281. Discharge estimates are provided for these times based on the range of discharges (minimum to maximum) of the previous and current date.
2022	Aerial Imagery (0.6-meter resolution)	USDA NAIP (USDA, 2022)	8/22/22 10:02-10:31 8/22/22 10:34-11:05 8/22/22 11:09-11:37	1210-1280 1210-1280 1210-1280	Data collected in 8.5km-wide vertical swathes. Collection dates and times provided for 10km upstream and downstream of HW281. Discharge estimates are provided for these times based on the range of discharges (minimum to maximum) of the previous and current date.
2024	Aerial Imagery (0.6-meter resolution)	USDA NAIP (USDA, 2024)	8/31/24 14:02-14:02 8/31/24 14:03-14:03 8/31/24 14:53-14:53 8/31/24 13:16-13:16	1060-1270 1060-1270 1060-1270 1060-1270	Data collected in 8.5km-wide vertical swathes split into 1 minute intervals. Collection dates and times provided for 10km upstream and downstream of HW281. Discharge estimates are provided for these times based on the range of discharges (minimum to maximum) of the previous and current date.

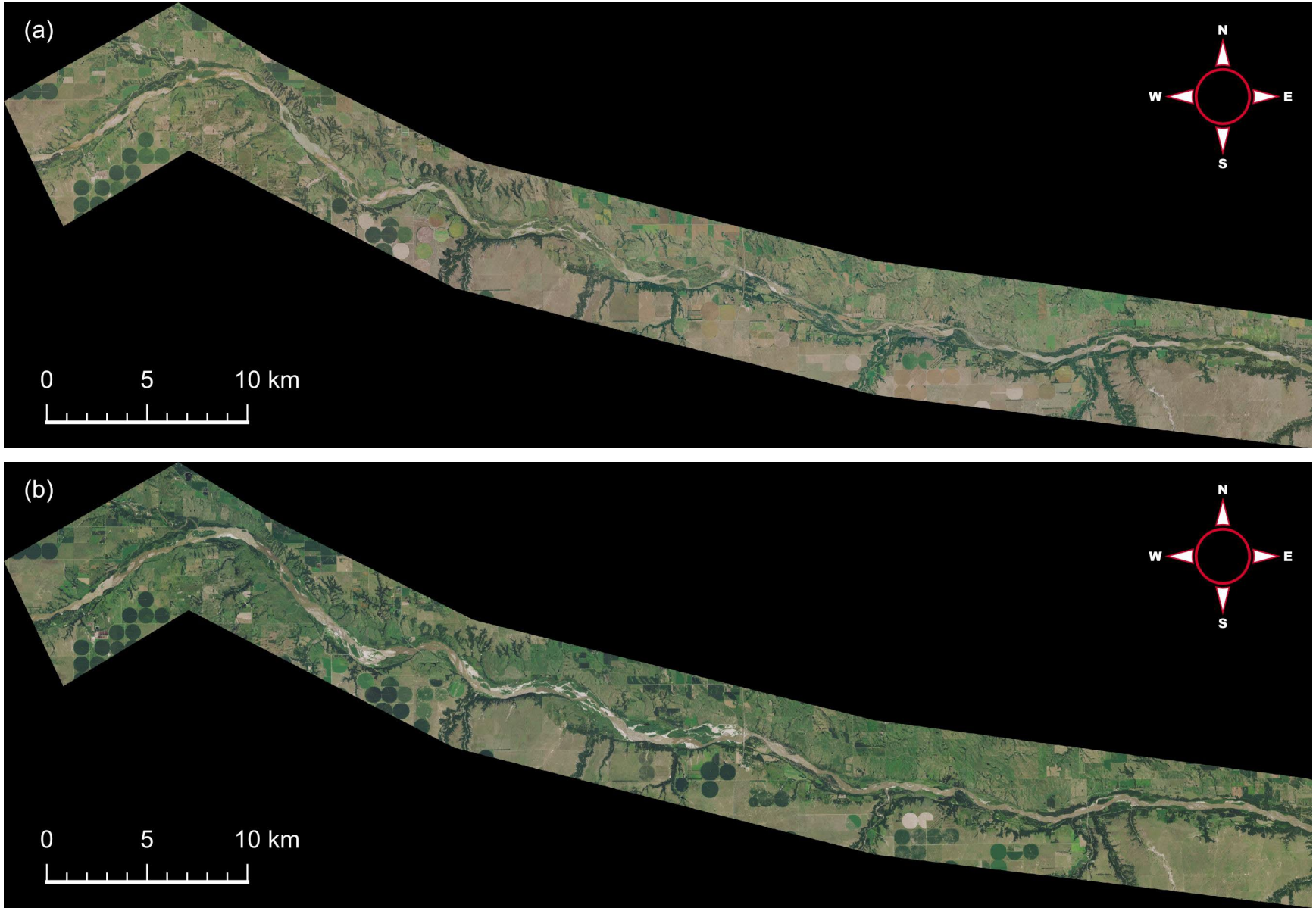

Figure C.1 NAIP aerial imagery of the Niobrara for Boyd and Holt Counties from (a) 2018 and (b) 2020

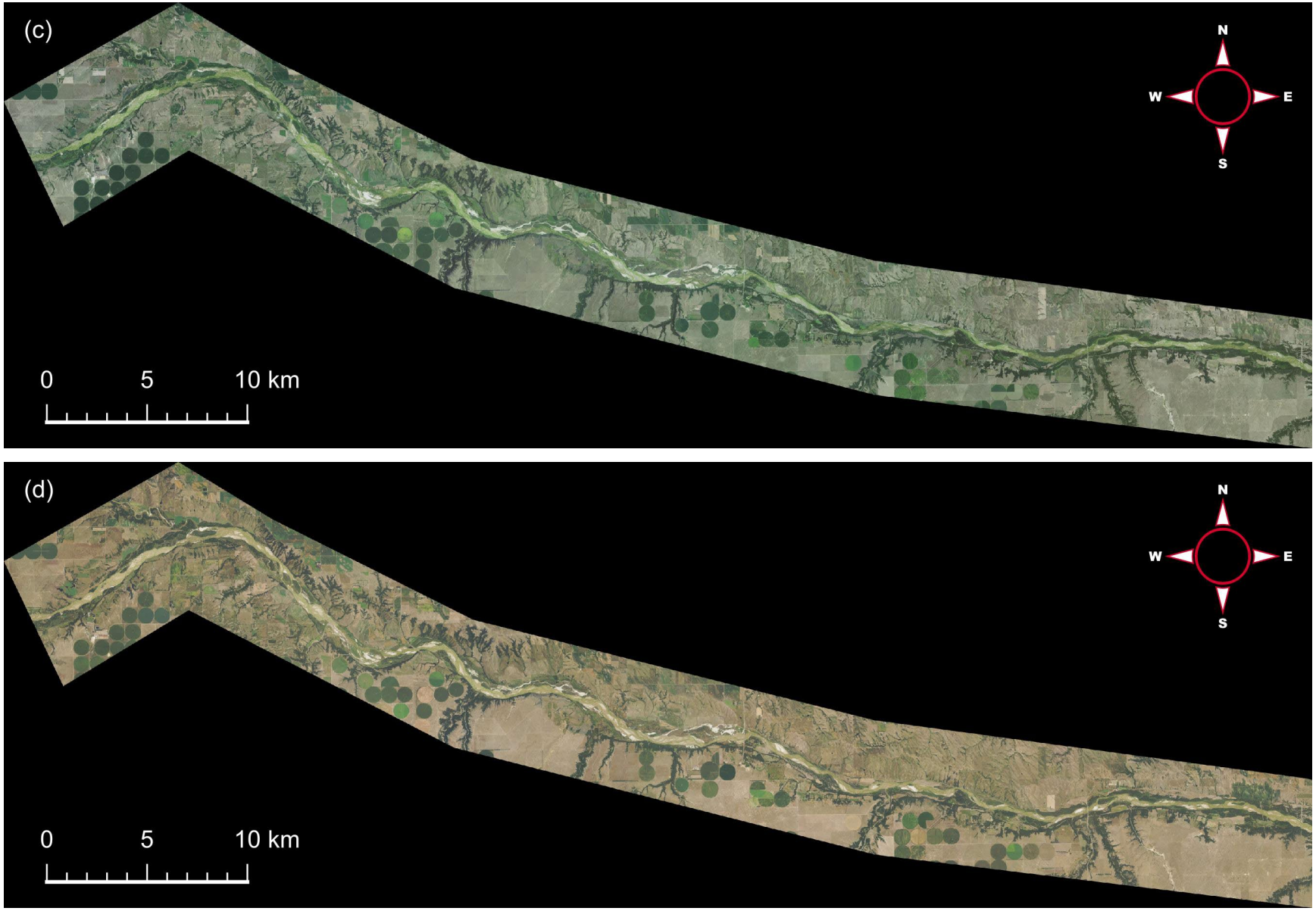

Figure C.1(cont.) NAIP aerial imagery of the Niobrara for Boyd and Holt Counties from (c) 2022 and (d) 2024

Figure C.2 7km long NAIP aerial images upstream of HW281 in (a) 2018 and (b) 2020

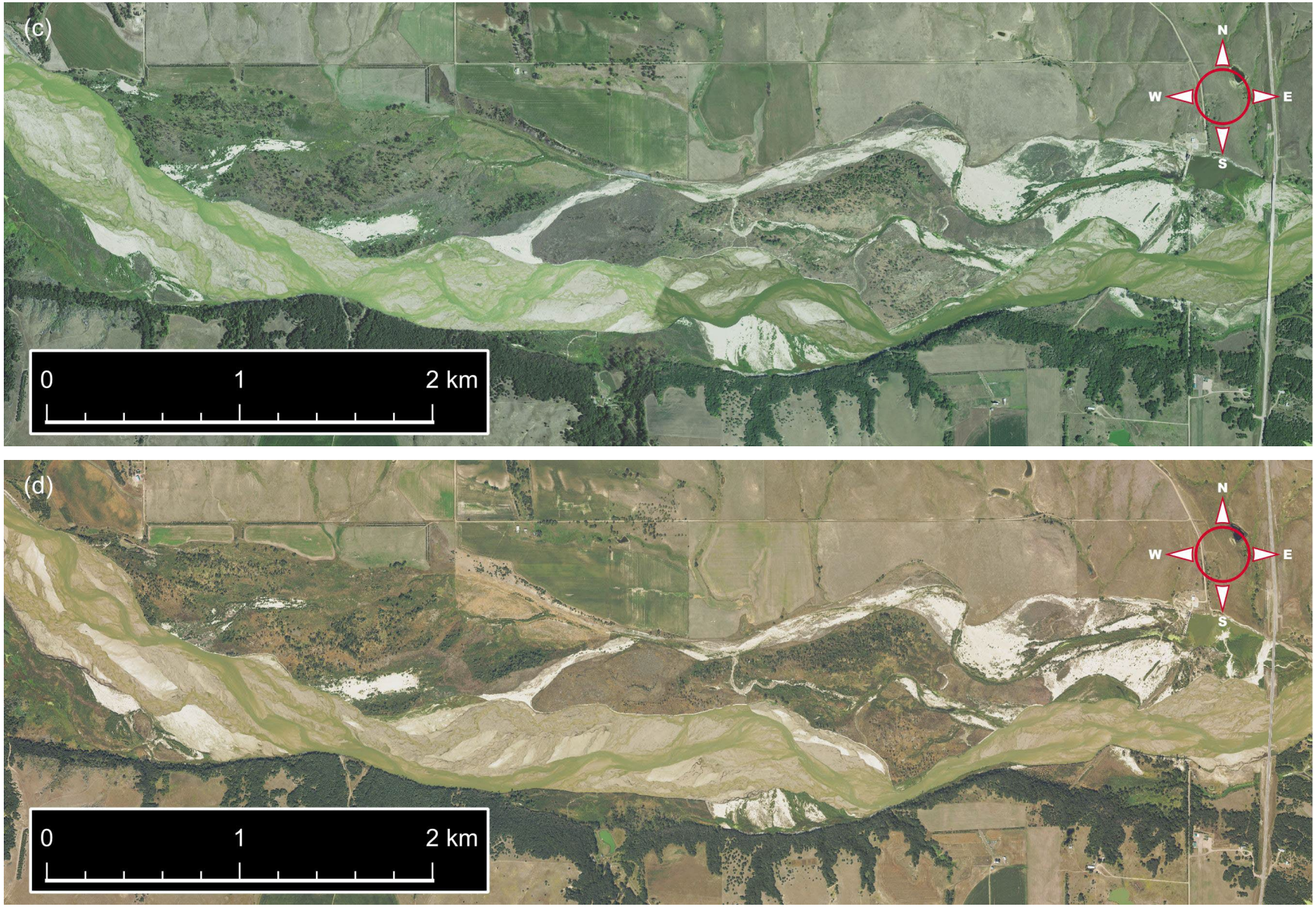

Figure C.2 (cont.) 7km long NAIP aerial images upstream of HW281 in (c) 2022 and (d) 2024

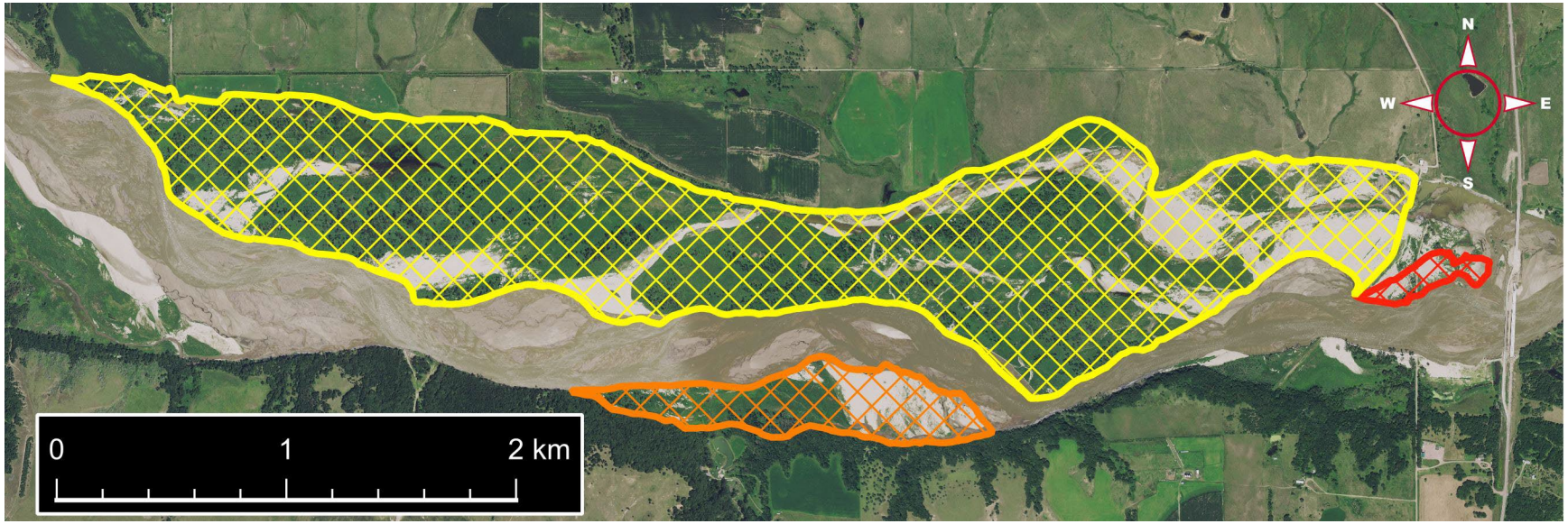

Figure C.3 Available sediment deposits upstream and downstream of the dam based on the 2020 DEM. Yellow is Area A and represents the largest deposit. Orange is Area B. Red is Area C. Area C is an underestimate and represents areas eroded thus far, but it is a small amount of sediment compared to what remains upstream of the dam in Areas A and B

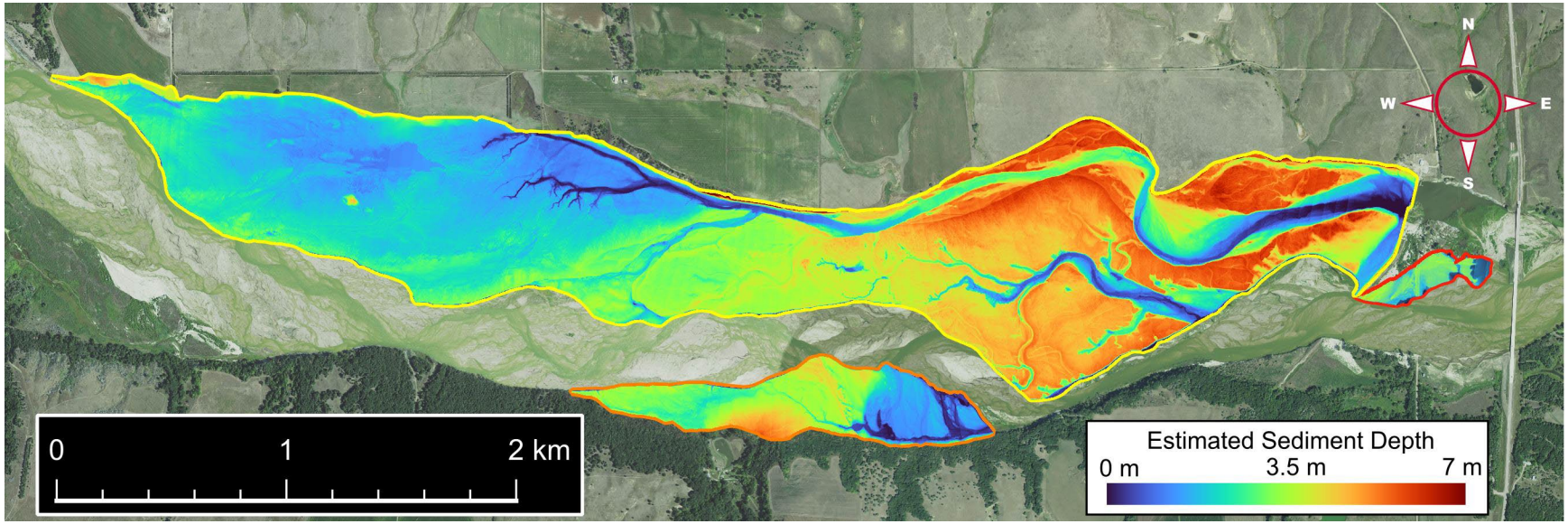

Figure C.4 Sediment availability in the vicinity of Spencer Dam as determined from the 2020 DEM using a datum based on minimum channel centerline elevations

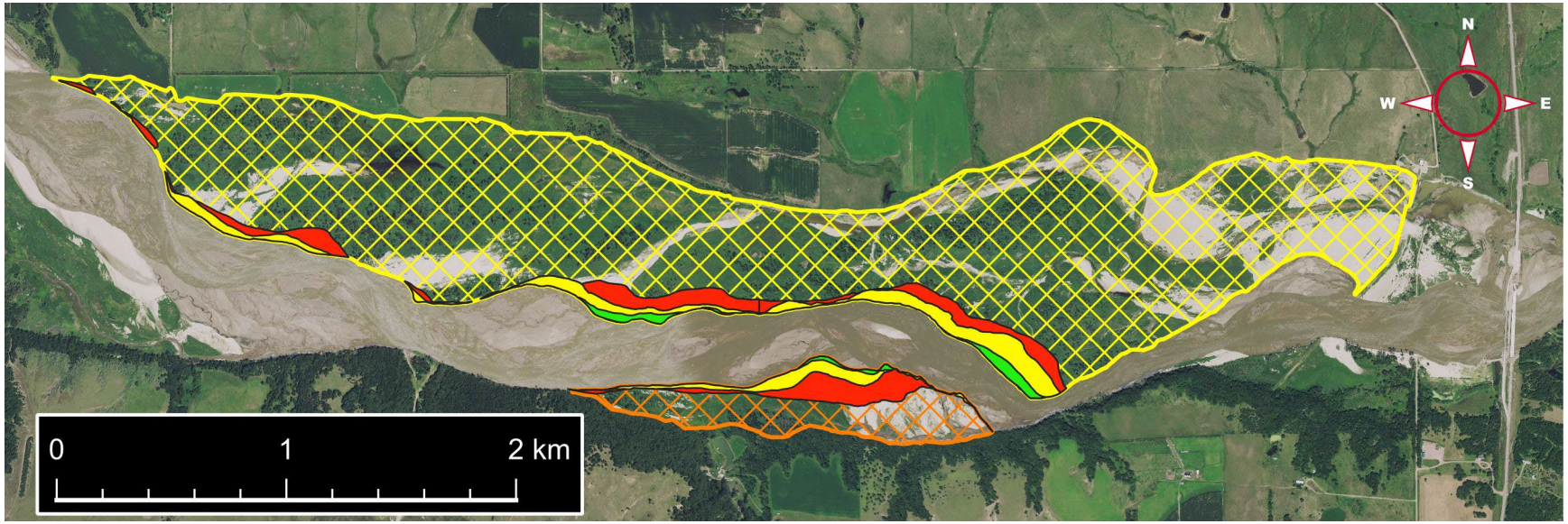

Figure C.5 Biannual sediment loss polygons based on NAIP observations. Green – 2020 DEM to 2020 NAIP. Yellow – 2020 NAIP to 2022 NAIP. Red – 2022 NAIP to 2024 NAIP. Note that green represents a much shorter time period than yellow and red

Table C.2 NAIP Sediment deposits and erosion from the time of the DEM until the specified NAIP Raster

Sediment Deposit	***Date***	***Estimated Available Sediment (m^3)***	***Available (red) or Eroded (green) Area (m^2)***	***Cumulative Volume Eroded (m^3)***	***Rasters used to Identify Remaining Sediment***
A	4/27/20	10979468	3539148		USGS DEM (2020). The Lidar Mapping Reports for the tiles used in this data set say that Lidar data collection for the region (WU_ID 198502) was done between 3/29/20 and 6/3/20. However, a swath map provided with the data shows more specifically that the lider data were collected on 4/27/20 for the entire area of the dam. Areas north of the reservoir (not used for sediment deposit analysis) and near Highway 11 were sampled on 4/06/20. These are the two dates specified for the entire study area.
A	7/27/20		27792	102047	USDA NAIP (2020)
A	8/22/22		160236	586598	USDA NAIP (2022)
A			167581	621485	February Ortho (2024)… only observes downstream part of Deposit A. This is a minimum estimate
A	8/31/24		296316	1058381	USDA NAIP (2024)
B	4/27/20	986721	365792		USGS DEM (2020). See notes given above for Deposit A
B	7/27/20		5084	17393	USDA NAIP (2020)
B	8/22/22		46409	153490	USDA NAIP (2022)
B	8/31/24		116059	354407	USDA NAIP (2024)

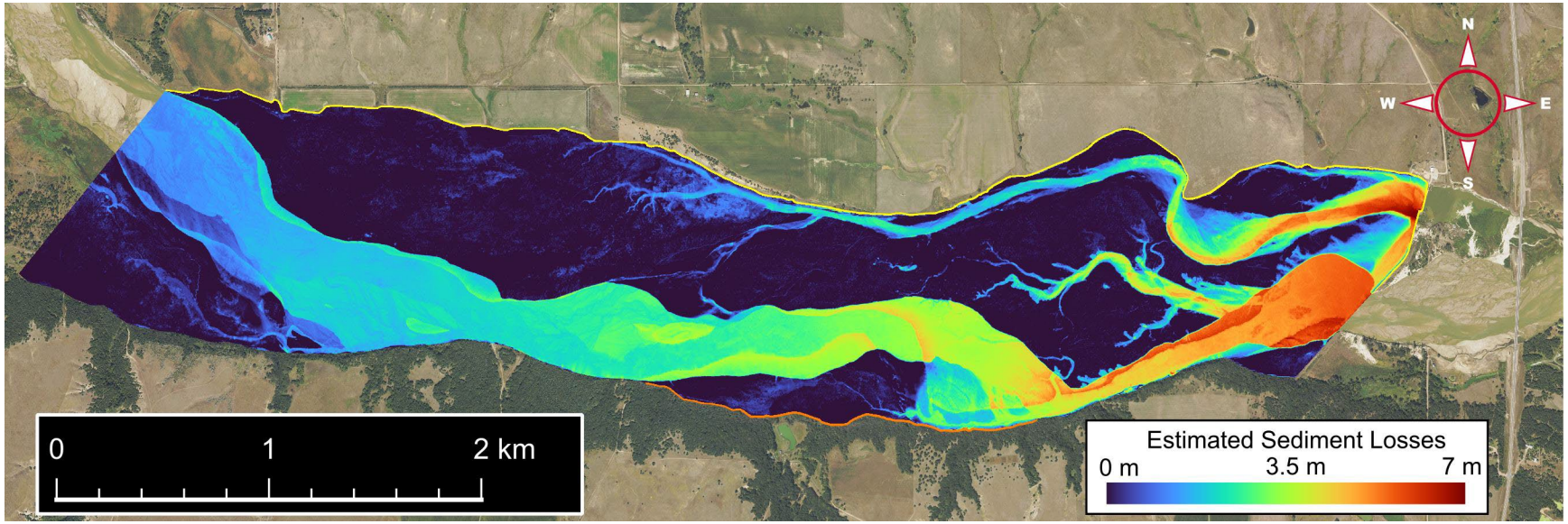

Figure C.6 Sediment losses upstream of Spencer Dam between 2013 and 2020 DEMs utilizing information as far as 6 km upstream of Spencer Dam

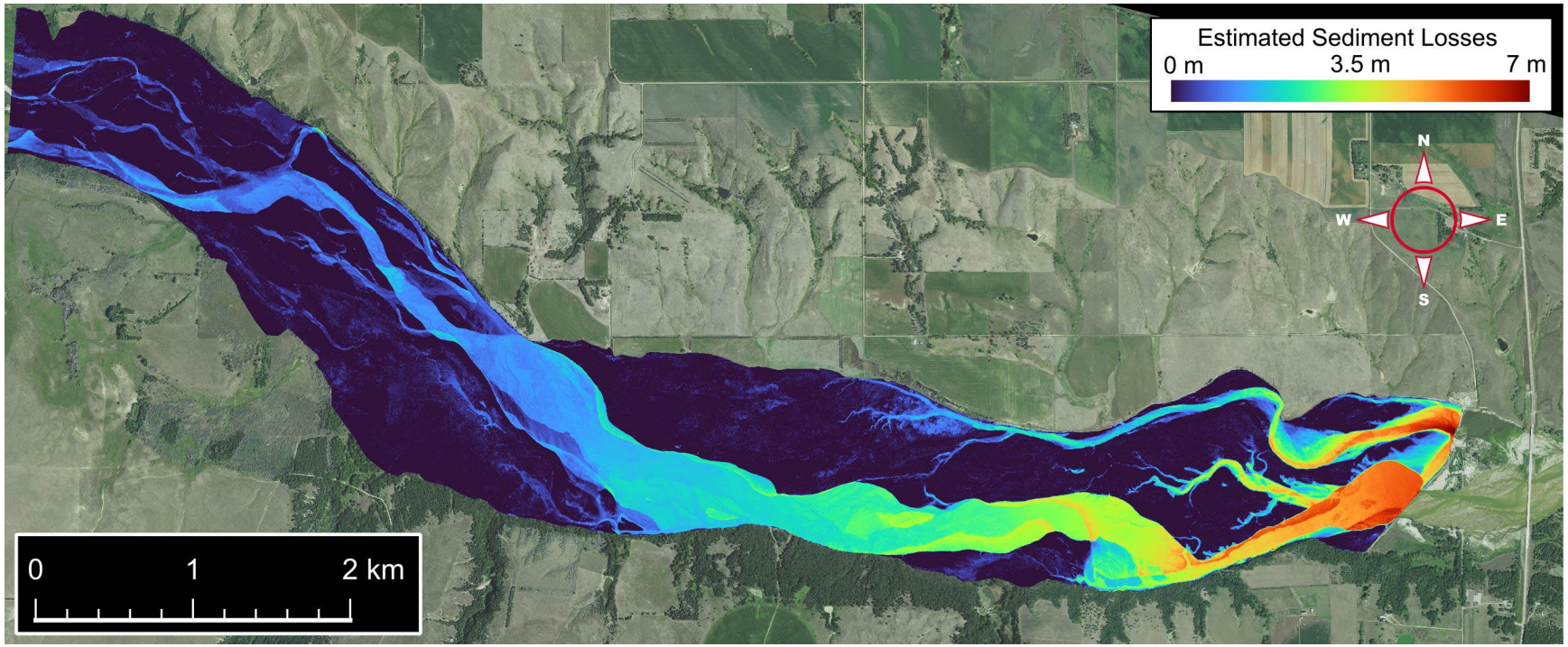

Figure C.7 Sediment losses upstream of Spencer Dam between 2013 and 2020 DEMs utilizing information as far as 10 km upstream of Spencer Dam

Table C.3 Analyzed areas and volumes eroded between 2013 and 2020 DEM for six and ten kilometers upstream of dam

Sediment Deposit	***Date***	***Analyzed Area (m^2)***	***Volume Eroded (m^3)***	***Rasters used to Identify Remaining Sediment***
Area 6 km upstream of dam	4/27/20	6490759	7419438	This is the sediment that was eroded between 2013 and 2020 after the dam failure, but only up to 6 km upstream because the reservoir appears to only extend that far. There are far less signs of erosion beyond this point.
Area 10 km upstream of dam	4/27/20	10350450	7830965	Same as above but for 10 km upstream.